A determination of the effective weak mixing angle from a measurement of the forward-backward charge asymmetry in heavy flavour decays of the Z^0 boson at LEP

Paul G. Colrain, B.Sc.(Hons)

Department of Physics and Astronomy

University of Glasgow

Thesis submitted for the degree of

Doctor of Philosophy

March 31, 1994

ProQuest LLC.
789 East Eisenhower Parkway
P.O. Box 1346
Ann Arbor, MI 48106 – 1346

Abstract

This thesis describes a measurement of the forward-backward hemisphere charge asymmetry in heavy flavour decays of the Z^0 boson using the ALEPH detector at LEP.

$Z^0 \rightarrow b\bar{b}$ decays are tagged by identifying the decay products of long-lived b hadrons via their large track impact parameters relative to the Z^0 decay point. The background event tagging efficiencies are estimated using Monte Carlo simulation, whereas the $b\bar{b}$ event tagging efficiency is evaluated by measuring the relative rates of single and double tagged events.

In a sample of 70,259 hadronic Z^0 decays, with a b purity of 88%, the charge asymmetry, $\langle Q_{FB} \rangle$, expressed as the mean difference between the momentum weighted forward and backward hemisphere charges, is measured to be

$$\langle Q_{FB} \rangle \; = \; -0.0112 \pm 0.0012(stat.) \pm 0.00018(syst.) \, .$$

Using a precision measurement of the mean b quark hemisphere charge, and accurate fits to the angular dependence of the event tagging efficiencies, $\langle Q_{FB} \rangle$ is used to determine a value for the electroweak asymmetry, $A_{FB}^{b\bar{b}}$:

$$A_{FB}^{b\bar{b}} \; = \; 0.1183 \pm 0.0131(stat.) \pm 0.00057(syst.) \, .$$

Interpreting $A_{FB}^{b\bar{b}}$ in the framework of the minimal Standard Model of electroweak interactions, the effective weak mixing angle, $sin^2\theta_W^{eff}$, is determined :

$$sin^2\theta_W^{eff} \; = \; 0.2281 \pm 0.0024(stat.) \pm 0.0011(syst.) \, .$$

This places the following Standard Model limits on the mass of the top quark, m_t :

$$m_t \; = \; 259^{+43}_{-50} \, \mathrm{GeV}/c^2 \, ,$$

or

$$m_t \; < \; 338 \, \mathrm{GeV}/c^2 \quad (95\% \text{ confidence level}) \, .$$

Preface

This thesis describes a measurement of the forward-backward charge asymmetry in heavy flavour decays of the Z^0 boson using the ALEPH detector at LEP. The data were collected in the year 1992. The measurement is interpreted in terms of the Standard Model of electroweak interactions and is used to determine a value for the effective weak mixing angle, $sin^2\theta_W^{eff}$.

The work of the ALEPH collaboration depends directly and indirectly on the participation of many people over a long period of time. My contribution to the working of the experiment included monitoring of the detector performance and the data acquisition. The material presented in this thesis reflects my own individual analysis of the ALEPH data as part of a working group. The final results depend on a previous measurement made within the collaboration (Section 4.2).

No portion of the work referred to in this thesis has been submitted in support of an application for another degree or qualification in this, or any other, institution of learning.

Acknowledgements

I would like to thank Andy Halley, my colleague in this analysis, for his patience and good advice. Thanks also to Ingrid Tenhave, Alain Blondel and Rick St. Denis for some helpful discussion and to my supervisor Robert Turnbull for his help and enthusiasm.

I would like to thank the Physics and Astronomy department of the University of Glasgow for giving me the opportunity to undertake this research and SERC for their financial support.

Contents

1 The Standard Model **1**

1.1 An overview of particle physics 1

1.2 Gauge theory 3

1.2.1 Introduction 3

1.2.2 Yang-Mills gauge theory 6

1.2.3 Quantum chromodynamics 7

1.3 The Standard Model of electroweak interactions 8

1.3.1 The symmetry group of the Standard Model : $SU(2)_L \times U(1)$ . . 8

1.3.2 The Higgs mechanism 10

1.3.3 The forward-backward asymmetry, $A_{FB}^{f\bar{f}}$ 13

2 The Experiment **18**

2.1 The LEP collider 18

2.2 The ALEPH detector 19

2.2.1 Tracking 21

2.2.2 Calorimetry 25

2.2.3 Trigger 26

2.2.4 Data acquisition 27

2.3 Monte Carlo simulation 28

3 The forward-backward charge asymmetry **29**

3.1 The forward-backward charge asymmetry, $\langle Q_{FB} \rangle$ 29

3.2 Relationship between $\langle Q_{FB} \rangle$ and $\mathcal{A}_{FB}^{b\bar{b}}$ 32

4 Tagging $Z^0 \to b\bar{b}$ decays using track impact parameters **36**

4.1 The impact parameter tag 37

4.1.1 Track impact parameters 37

4.1.2 The tag variable 39

4.1.3 Monte Carlo hemisphere and event tagging efficiencies 42

4.2 Determination of the hemisphere tagging efficiencies 44

4.2.1 The 'Double Tag' method 44

4.2.2 Experimental Results 46

4.3 Angular dependence of the event tagging efficiencies 49

4.3.1 Modelling the angular dependence 50

4.3.2 The flavour dependent acceptance factors 52

4.4 Summary 56

5 Quark charge separations **57**

5.1 Monte Carlo quark charge separations 57

5.1.1 κ dependence 58

5.1.2 Impact parameter tag cut dependence 60

5.1.3 Fragmentation systematic errors 61

5.2 A measurement of the b charge separation using the impact parameter tag 63

5.2.1 Principle of the measurement 65

5.2.2 Experimental results 66

5.2.3 Determination of the b charge separation 70

5.3 Summary 71

6 A measurement of the forward-backward charge asymmetry **73**

6.1 Event Selection 74

6.2 The measured forward-backward charge asymmetry 75

6.3 Experimental systematic errors 78

6.3.1 Forward-backward momentum imbalance 79

6.3.2 Material asymmetry 80

6.3.3 Track losses 80

6.3.4 Charged tracks with unphysically high momentum 81

6.4 Summary 81

7 Electroweak interpretation of the charge asymmetry **83**

7.1 A Standard Model analysis of the data 83

7.2 QCD corrections to $\mathcal{A}_{FB}^{b\bar{b}}$ 87

7.3 The fitting procedure 89

7.4 Systematic errors 92

8 Summary and conclusions **96**

Chapter 1

The Standard Model

1.1 An overview of particle physics

Particle physics concerns itself with the question : What are the fundamental constituents of the universe ? The current answer to this question is displayed in table 1.1 and is the result of many decades of dialogue between experimental and theoretical particle physicists.

All matter in the universe appears to be made of fundamental particles, called *fermions*, possessing intrinsic angular momentum, or spin, of magnitude $\frac{1}{2}\hbar$ where $\hbar$ is Planck's constant divided by 2π. These particles are believed to be structureless and pointlike on the scale of $10^{-17}m$. There are a total of 12 such elementary particles each having a unique set of characteristics, or *quantum numbers*, owing to their different response to the three 'fundamental' forces of nature, the *strong*, *electromagnetic* and *weak* forces. The effect of *gravity* on the elementary particles is so weak, compared to the other three forces, that it can be safely ignored. Six of these particles, called *quarks*, feel the effects of all three forces. Of the remaining particles, called *leptons*, three couple to the the electromagnetic and weak forces (the charged leptons) while the remaining three feel the effect of the weak force only (the neutral leptons or neutrinos).

Name	*charge*	*spin*
Quarks		
u (up), c (charmed), t (top)	$+\frac{2}{3}$	$\frac{1}{2}$
d (down), s (strange), b (bottom)	$-\frac{1}{3}$	$\frac{1}{2}$
Leptons		
e (electron), μ (muon), τ (tau)	-1	$\frac{1}{2}$
ν_e *(electron neutrino),* ν_μ, ν_τ	0	$\frac{1}{2}$
Gauge bosons		
γ *(photon)*	0	1
$W^{\pm}$, Z^0 *(Weak bosons)*	± 1, 0	1
g_i *(i=1,...,8, gluons)*	0	1
G (graviton)	0	2

Table 1.1: *The fundamental constituents of the universe. For each charged particle there is an associated anti-particle of the same mass but of opposite electromagnetic charge.*

The strong force acts only over very small distances and binds quarks together within protons and neutrons (nucleons) [1]. Its residual effects are believed to be responsible for the attraction between nucleons inside nuclei. The electromagnetic force is responsible for the attraction between electrons and nuclei which binds atoms and molecules, controlling chemistry and the physics of materials. The strength of the electromagnetic force, relative to the strong force, is $\sim 10^{-2}$. The weak force governs processes such as nuclear β-decay causing protons to transmute into neutrons and vice-versa ; it is vital for the synthesis of light elements in the early universe. Its strength relative to the strong force is $\sim 10^{-13}$. (The corresponding strength of gravity is $\sim 10^{-38}$). These forces are all transmitted by specific fields or particles which are equivalent concepts in the quantum field theory used to explain their properties.

The mediating particles are called gauge bosons ; for the electromagnetic, weak and strong forces they have spin $1\hbar$. (See table 1.1). The electromagnetic and strong forces are mediated by a massless photon, γ, and eight massless gluons, g_i $(i = 1, ..., 8)$, respectively, whereas the weak force is mediated by 3 massive particles, the $W^{\pm}$ and Z^0 bosons.

A major problem with our understanding of these fundamental forces is in their number and disparate strengths and properties. The Standard Model of electroweak interactions of Glashow, Weinberg and Salam [2] [3] [4] attempts to unify two of these forces, the weak force and the electromagnetic force, inside a consistent mathematical framework. The Standard Model is an SU(2)×U(1) *gauge* field theory reflecting the SU(2) and U(1) gauge structures of the weak and electromagnetic interactions respectively.

Section 1.2 gives a short introduction to gauge field theories and in section 1.3 a summary of the structure of the Standard Model theory is given, including an explanation of the Higgs mechanism by which the gauge bosons and the fermions are given mass.

1.2 Gauge theory

1.2.1 Introduction

Symmetry principles play an important role in the physics of elementary particles. The presence of a symmetry in a physical system, for example invariance of the system under spatial rotations, implies the existence of a conserved quantity, in this case rotational angular momentum. It is present belief that all particle interactions are governed by internal symmetries called *gauge* symmetries that are independent of the space-time coordinates.

The Lagrangian formalism [5] provides a convenient way of identifying the conserved

quantities ; starting from a scalar Lagrangian, $\mathcal{L}$, there is a conserved quantity corresponding to each continuous symmetry transformation which leaves the Lagrangian and the resulting equations of motion invariant in form. Such a theorem, known as Noether's theorem, permits observed selection rules to be described in terms of symmetry requirements in $\mathcal{L}$ and is very useful as a guide for the introduction of interaction terms in developing new theories.

Quantum electrodynamics (QED), the theory of the interaction between charged fermions and photons, has the vital property that the various unphysical infinite contributions that routinely arise in quantum field theories can all be consistently eliminated ; the theory is said to be *renormalisable*. This can be traced to the fact that the QED Lagrangian is invariant under local gauge transformations of the fermion field, $\psi(x^\mu)$, and the photon field, $A_\nu(x^\mu)$:

$$\begin{aligned} \psi(x^\mu) &\rightarrow e^{iq\theta(x^\mu)}\psi(x^\mu) \,, \\ A_\nu(x^\mu) &\rightarrow A_\nu(x^\mu) + \partial_\nu\theta(x^\mu) \,, \end{aligned}$$

where $\theta(x^\mu)$ depends arbitrarily on the space time coordinates x^μ. q is the fermion-photon coupling. In other words, the complex phase of the fermion field, ψ, can be altered in an arbitrary way as long as a massless spin 1 gauge field, A_μ, is introduced and adjusted simultaneously in a suitable way. The conserved quantity corresponding to this internal symmetry can be shown to be the electromagnetic charge of the system.

The phase factor, $e^{iq\theta(x)}$, belongs to the symmetry group U(1) of unitary transformations. By 'designing' the Lagrangian to be invariant under the transformations of more general symmetry groups, the properties of other forces can be described in a similar way.

Some of the properties of the weak force can be understood if the electron field, e,

and its neutrino field, ν_e, are regarded as two components of a 'doublet' fermion field :

$$\psi = \begin{pmatrix} e \\ \\ \nu_e \end{pmatrix} .$$

By requiring that the corresponding free fermion Lagrangian be invariant under transformations of the form

$$\psi \rightarrow U(\theta(x))\, \psi \, , \tag{1.1}$$

where $U(\theta)$ is a 2×2 unitary matrix, requires the introduction of three massless spin 1 gauge fields, W^+, W^- and W^0, with which the fermion doublet can interact. In this case the transformations are more complex than the U(1) phase changes of QED since the off diagonal terms in $U(\theta)$ can change one member of the doublet into the other : $e \leftrightarrow \nu_e$. Weak interactions involving other fermions can be described in a similar way by constructing the doublets

$$\begin{pmatrix} \mu \\ \\ \nu_\mu \end{pmatrix} , \begin{pmatrix} \tau \\ \\ \nu_\tau \end{pmatrix} , \begin{pmatrix} u \\ \\ d \end{pmatrix} , \begin{pmatrix} c \\ \\ s \end{pmatrix} , \begin{pmatrix} t \\ \\ b \end{pmatrix} .$$

The above transformations (1.1) belong to the symmetry group SU(2) of special unitary transformations of which a complex doublet is the simplest representation.

The physical predictions corresponding to a chosen symmetry can be systematically derived using quantum field theory[6]. The fields, such as ψ and A_μ, are elevated to operators which act in the vector space of all possible physical states creating and annihilating their corresponding particles. Interaction probabilities are then computed by evaluating a perturbation series in $\mathcal{L}_{int}$, the interaction terms in the Lagrangian. It is then possible to identify a correspondence between certain factors in the probability amplitudes and the various terms in the Lagrangian. Once this connection is identified, predictions of physical quantities can be made simply by following a set of rules called Feynman rules [7].

In the following section the structure of a Yang-Mills gauge theory is formally introduced. A Yang-Mills gauge theory is the most general gauge theory describing the interaction of fermions with gauge fields. The results presented will be applied to the electroweak theory in section 1.3.

1.2.2 Yang-Mills gauge theory

The Lagrangian, $\mathcal{L}(\psi, \partial_\mu \psi)$, describing the free propagation of a fermion field, ψ, is given by

$$\mathcal{L} = \bar{\psi}(i\gamma^\mu \partial_\mu - m)\psi \,.$$

ψ is in general a column vector including the fields of all fermions in the theory. A Yang-Mills gauge transformation of ψ is a D-dimensional continuous transformation,

$$\begin{aligned} \psi &\rightarrow U(\theta^A)\psi \quad (A = 1, 2, ..., D)\,, \\ &= e^{ig\sum_A \theta^A T^A}\psi\,, \end{aligned}$$

where T^A are the generators of a symmetry group of transformations which act on the fermion field, ψ. The structure of the group is summarised by the commutation relations

$$[T^A, T^B] = iC^{ABC}T^C\,,$$

where the structure constants, C^{ABC}, depend on the group. If the parameters θ^A depend arbitrarily on the space-time coordinates, $\theta^A = \theta^A(x^\mu)$, then the Lagrangian, $\mathcal{L}(\psi, \partial_\mu \psi)$, is in general *not* invariant under the transformations $U(\theta^A(x^\mu))$. Such gauge transformations are described as being *local* gauge transformations.

However, by introducing a set of gauge fields, V_μ^A, (in one-to-one correspondence with the generators of the group) with the transformation law

$$\sum_A T^A V_\mu^A \rightarrow U(\sum_A T^A V_\mu^A)U^{-1} - (1/ig)(\partial_\mu U)U^{-1}$$

and by modifying the space-time dependence of the fermion field,

$$\partial_\mu \psi \rightarrow D_\mu \psi = (\partial_\mu + ig \sum_A T^A V_\mu^A)\psi \ ,$$

gauge invariance of the Lagrangian can be achieved. This procedure introduces a mechanism whereby certain components of ψ can mix. That mechanism is the interaction of the fermions with massless spin 1 gauge particles with coupling g.

The complete Yang-Mills Lagrangian can be written in the form

$$\mathcal{L}_{YM} = -\frac{1}{4} \sum_A F_{\mu\nu}^A F^{A\,\mu\nu} + \mathcal{L}(\psi, D_\mu \psi) \ ,$$

where $F_{\mu\nu}^A$ is the gauge invariant antisymmetric tensor describing the kinetic energy and self-interaction of the gauge fields V_μ^A :

$$F_{\mu\nu}^A = \partial_\mu V_\nu^A - \partial_\nu V_\mu^A - g C_{ABC} V_\mu^B V_\nu^C \ .$$

In a U(1) gauge theory, such as QED, there is just one generator and the structure constants are trivially zero. Consequently, the antisymmetric tensor does not possess terms quadratic in the gauge fields. As a result, the gauge field A^μ of QED does not interact with itself ; there is no photon-photon coupling. In more general *non-Abelian* theories, the generators of the symmetry group do not commute and quadratic terms are present, allowing the gauge fields to interact with each other. This is the case in the Standard Model of electroweak interactions discussed in section 1.3.

Many of the properties of the strong force can be explained using an SU(3) Yang-Mills gauge theory called Quantum Chromodynamics, or QCD in analogy to QED. Section 1.2.3 below gives a brief description of QCD.

1.2.3 Quantum chromodynamics

Many of the high energy phenomena involving quarks and gluons can be described using an SU(3) local gauge theory called Quantum Chromodynamics. In this theory a

quark is represented by a 3-component field where each component is labelled with one of three 'colour' charges, red, blue or green. The symmetry group SU(3) of unitary transformations of these fields is generated by eight hermitian 3×3 matrices λ^A $(A = 1, ..., 8)$. Consequently, when local gauge invariance is imposed on the free quark Lagrangian, eight massless gauge bosons are introduced. These gauge bosons are precisely the gluons mentioned above.

Due to the non-abelian nature of SU(3), the QCD Lagrangian contains gluon self-interaction terms whose presence has dramatic implications for the nature of the strong force. Because the gluons themselves carry colour, they contribute to the polarisation of the vacuum causing the quark-gluon coupling, α_s, to decrease as the energy of the process under study increases. As a result, at very high energies, or equivalently very short distances, the quarks within hadrons behave as free particles. This phenomenon is referred to as 'asymptotic freedom' and is crucial for the perturbative calculation of high energy QCD processes. The large coupling involved in lower energy processes, such as quark hadronisation, excludes the use of perturbation theory, and at present semi-empirical models have to be used [8] [9].

1.3 The Standard Model of electroweak interactions

1.3.1 The symmetry group of the Standard Model : $SU(2)_L \times U(1)$

The basic Standard Model Lagrangian of Glashow, Weinberg and Salam can be written as[1]

$$\mathcal{L}_{SM} = -\frac{1}{4}\sum_{A=1}^{3} F^A_{\mu\nu} F^{A\,\mu\nu} - \frac{1}{4} B_{\mu\nu} B^{\mu\nu} + \bar{\psi}_L i\gamma^\mu D_\mu \psi_L + \bar{\psi}_R i\gamma^\mu D_\mu \psi_R \qquad (1.2)$$

[1]Only the symmetric part of the S.M. Lagrangian, which involves massless gauge bosons and fermions, is shown here. In the next section the Higgs mechanism is described, whereby the symmetry is spontaneously broken giving mass to the bosons and fermions.

This is the Yang-Mills Lagrangian for the symmetry group SU(2)×U(1). That is, $\mathcal{L}_{SM}$ is invariant in form under SU(2) and U(1) transformations simultaneously. $B_{\mu\nu}$ and $F^A_{\mu\nu}$ are the antisymmetric tensors constructed from the gauge fields B_μ of U(1) and W^A_μ $(A = 1, 2, 3)$ of SU(2) respectively.

The L and R subscripts on the fermion field, ψ, indicate its left and right-handed projections respectively. It is observed in nature that the gauge fields, W^A_μ, associated with the SU(2) symmetry of the Standard Model couple only to a particular projection, ψ_L, of the fermion spinor fields[2] :

$$\psi_L = \frac{1}{2}(1 - \gamma_5)\psi \,.$$

This component is called the left-handed component. Consequently, the left-handed fermions are grouped into SU(2) doublets but the orthogonal right-handed components remain as singlet fields. The gauge field ,B_μ, of U(1) couples equally to left and right-handed fermions.

The modified fermion derivatives, $D_\mu\psi$, are given by

$$D_\mu\psi_{L,R} = \left[\partial_\mu + ig\sum_{A=1}^{3} T^A_{L,R}W^A_\mu + ig'\frac{1}{2}Y_{L,R}B_\mu\right]\psi_{L,R}\,, \tag{1.3}$$

where $T^A_{L,R}(A = 1, 2, 3)$ and $\frac{1}{2}Y_{L,R}$ are the SU(2) and U(1) generators and g and g' are their respective fermion-gauge couplings. $T = (T^1, T^2, T^3)$ and Y are called the weak *isospin* and weak *hypercharge* respectively and are related to the charge operator, Q, which generates the U(1) transformations of QED, by

$$Q = T^3_L + \frac{1}{2}Y_L = T^3_R + \frac{1}{2}Y_R\,. \tag{1.4}$$

The physical fields, A_μ, Z_μ and $W^\pm_\mu$, are linear combinations of the gauge fields, B_μ and W^A_μ, in terms of which the SU(2)×U(1) symmetry is apparent :

$$A_\mu \;=\; cos\theta_W B_\mu + sin\theta_W W^3_\mu\,, \tag{1.5}$$

[2] γ_5 is one of the five Dirac γ-matrices. See for example [5]

$$Z_\mu = -sin\theta_W B_\mu + cos\theta_W W_\mu^3 , \tag{1.6}$$

$$W_\mu^\pm = (W_\mu^1 \pm iW_\mu^2)/\sqrt{2} . \tag{1.7}$$

θ_W is the weak mixing angle, or Weinberg angle. Using expression (1.4) for the charge operator Q, θ_W can be expressed in terms of the SU(2) and U(1) couplings g and g' :

$$gsin\theta_W = g'cos\theta_W = e ,$$

giving

$$tan\theta_W = \frac{g'}{g} . \tag{1.8}$$

The theory, as it stands, describes the interaction of *massless* gauge bosons with *massless* fermions. However, experiment excludes this scenario. For example, the mass of the Z^0 boson has been measured at LEP to be 91.187 ± 0.007 GeV/c^2 [10]. If mass terms, such as $M^2 W_\mu W^\mu$, are introduced into the Lagrangian on their own, the local gauge symmetry is broken, the theory becomes unrenormalisable and loses its predictive power. A mechanism is required whereby gauge boson mass terms can be introduced into the Lagrangian without violating gauge invariance. One such mechanism, called the Higgs mechanism, is described in the next section.

1.3.2 The Higgs mechanism

In the *minimal* Standard Model the Higgs mechanism involves the introduction of *four* scalar (spin 0) fields, $\phi_i(x^\mu)$, arranged as a complex SU(2) doublet :

$$\phi(x^\mu) = \begin{pmatrix} \phi_+(x^\mu) \\ \phi_0(x^\mu) \end{pmatrix} \quad : \quad \begin{matrix} \phi_+ = (\phi_1 + i\phi_2)/\sqrt{2} \\ \phi_0 = (\phi_3 + i\phi_4)/\sqrt{2} \end{matrix} ,$$

with weak hypercharge $Y = 1$. The free propagation of this field ϕ is described by the Lagrangian

$$\mathcal{L}_{Higgs} = (\partial_\mu \phi)^\dagger (\partial^\mu \phi) - \mu^2 \phi^\dagger \phi - \lambda (\phi^\dagger \phi)^2$$

with $\lambda > 0$ and $\mu^2 < 0$.

Just as for a fermion doublet the imposition of SU(2)×U(1) local gauge invariance requires the introduction of four gauge fields and the modification of the Lagrangian

$$\mathcal{L}_{Higgs} = |(\partial_\mu + ig\sum_{A=1}^{3} T^A_{L,R} W^A_\mu + ig'\frac{1}{2} Y_{L,R} B_\mu)\phi|^2 - \mu^2 \phi^\dagger \phi - \lambda(\phi^\dagger \phi)^2 \,.$$

By a suitable SU(2) gauge transformation ϕ can be written in terms of just one scalar field, h :

$$\phi(x^\mu) = \frac{1}{\sqrt{2}} \begin{pmatrix} 0 \\ \\ v + h(x^\mu) \end{pmatrix}$$

with ground state, or vacuum expectation value,

$$\phi_0 = \frac{1}{\sqrt{2}} \begin{pmatrix} 0 \\ \\ v \end{pmatrix} \,. \tag{1.9}$$

By choosing a particular ground state the Lagrangian takes a form in which the symmetry is 'hidden' and terms identifiable as gauge boson mass terms appear. Inserting (1.9) into the above Lagrangian and interpreting the resulting expression in terms of the physical fields, $W^\pm_\mu$, A_μ and Z_μ, the following gauge boson masses are obtained :

$$\begin{aligned} M_W &= \frac{1}{2} v g \,, \\ M_A &= 0 \,, \\ M_Z &= \frac{1}{2} v \sqrt{g^2 + g'^2} \,. \end{aligned}$$

The quantum numbers of the Higgs field ($Y = 1$, $T = \frac{1}{2}$) were constructed with the requirement that the photon be massless, so the result $M_A = 0$ is just a consistency check. However the result

$$\frac{M_W}{M_Z} = \frac{g}{\sqrt{g^2 + g'^2}} = cos\theta_W \,,$$

where equation (1.8) has been used in the last step, is a prediction of the Standard Model. The generation of the gauge boson masses in this way is called 'spontaneous symmetry breaking'.

The same Higgs doublet has exactly the required quantum numbers to give mass to the fermion matter fields also. For example, to generate the electron mass the following SU(2)×U(1) gauge invariant term is introduced

$$-G_e \left[(\bar{\nu}_e, \bar{e})_L \begin{pmatrix} \phi^+ \\ \phi^0 \end{pmatrix} e_R + \bar{e_R}(\phi^-, \bar{\phi^0}) \begin{pmatrix} \nu_e \\ e \end{pmatrix}_L \right] .$$

By spontaneously breaking the gauge symmetry and substituting (1.9) for ϕ, the electron mass is revealed :

$$m_e = \frac{G_e v}{\sqrt{2}} .$$

Note however that G_e is arbitrary, so the actual mass of the electron is not predicted. The masses of the quarks are generated in a similar way.

To summarise, the complete Standard electroweak Lagrangian can be written as

$$\begin{aligned} \mathcal{L} = & - \frac{1}{4} \sum_{A=1}^{3} W^A_{\mu\nu} W^{A\,\mu\nu} - \frac{1}{4} B_{\mu\nu} B^{\mu\nu} \\ & + \bar{\psi}_{L,R} \gamma^\mu (\partial_\mu + ig \sum_{A=1}^{3} T^A_{L,R} W^A_\mu + ig' \frac{1}{2} Y_{L,R} B_\mu) \psi_{L,R} \\ & + |(\partial_\mu + ig \sum_{A=1}^{3} T^A_{L,R} W^A_\mu + ig' \frac{1}{2} Y_{L,R} B_\mu)\phi|^2 - \mu^2 \phi^\dagger \phi - \lambda (\phi^\dagger \phi)^2 \\ & - (G_1 \bar{\psi}_L \phi \psi_R + G_2 \bar{\psi}_L \phi_c \psi_R + h.c.) \end{aligned} \tag{1.10}$$

The Standard Model Lagrangian involves a certain number of free parameters which are not fixed by the theory, such as the fermion masses, the gauge couplings and the Higgs field vacuum expectation value. These parameters, or appropriate combinations, can be measured using Standard Model calculations of physical observables such as interaction cross-section and lifetimes. Once the physical input is defined the values of other observables can be predicted allowing the internal gauge structure of the theory to

be tested. In the following section the prediction for the forward-backward asymmetry in the process $e^+e^- \rightarrow f\bar{f}$ is presented and its use as a test of the Standard Model is discussed.

1.3.3 The forward-backward asymmetry, $A_{FB}^{f\bar{f}}$

The fermion couplings to the physical gauge fields can be derived directly from the Lagrangian (1.10) using the relations (1.5)-(1.7). For example, the A_μ and Z_μ couplings are given by [11]

$$\begin{aligned} V_{\psi\bar{\psi}\gamma} &= e\left[\bar{\psi}\gamma_\mu Q\psi\right]A^\mu\,, \\ V_{\psi\bar{\psi}Z^0} &= \frac{g}{2cos\theta_W}\bar{\psi}\gamma_\mu\left[T_L^3(1-\gamma_5)+T_R^3(1-\gamma_5)-Qsin^2\theta_W\right]\psi Z^\mu\,. \end{aligned}$$

Alternatively the Z^0 coupling can be written as

$$V_{\psi\bar{\psi}Z^0} = e\bar{\psi}\gamma_\mu\left[v_f - a_f\gamma_5\right]\psi Z^\mu\,,$$

where v_f and a_f are the vector and axial-vector Z^0-fermion couplings :

$$v_f = \frac{I_3^f - 2sin^2\theta_W Q_f}{2sin\theta_W cos\theta_W}, \quad a_f = \frac{I_3^f}{2sin\theta_W cos\theta_W}\,.$$

Together with the photon propagator,

$$\frac{-ig^{\mu\nu}}{k^2}\,,$$

and the Z^0 boson propagator,

$$\frac{-ig^{\mu\nu}+k^\mu k^\nu/M_Z}{k^2-M_Z^2}\,,$$

these form a set of Feynman rules allowing the calculation of interaction cross-sections and lifetimes involving neutral current processes.

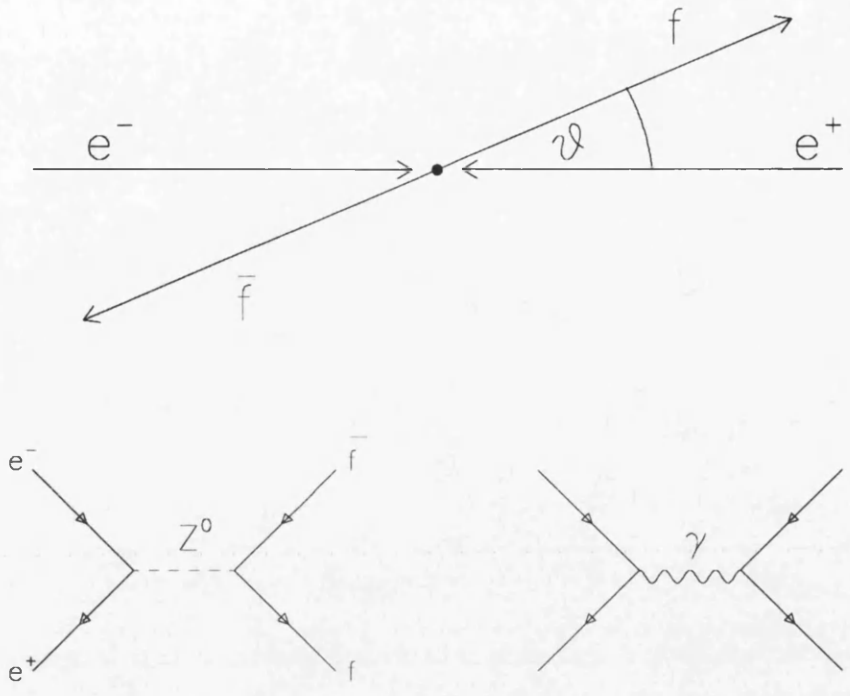

Figure 1.1: *Schematic diagram of the process* $e^+ e^- \rightarrow f\bar{f}$ *and the two lowest order contributing diagrams.*

In lowest order the prediction for the differential cross-section for the process $e^+e^- \rightarrow f\bar{f}$ is given by ($\mu_f = m_f^2/s$) :

$$\frac{d\sigma^f}{d\Omega} = \frac{\alpha^2}{4s} 3\sqrt{1-4\mu_f} \quad [\, G_1(s)\cdot(1+cos^2\theta) + G_3(s)\cdot\sqrt{1-4\mu_f}\cdot 2cos\theta + G_2(s)\cdot 4\mu_f \cdot sin^2\theta\,], \tag{1.11}$$

where

$$\begin{aligned} G_1(s) &= Q_e^2 Q_f^2 + 2Q_e Q_f v_e v_f Re\chi_0(s) + (v_e^2+a_e^2)(v_f^2+a_f^2-4\mu_f a_f^2)|\chi_0(s)|^2\,, \\ G_2(s) &= Q_e^2 Q_f^2 + 2Q_e Q_f v_e v_f Re\chi_0(s) + (v_e^2+a_e^2)v_f^2|\chi_0(s)|^2\,, \\ G_3(s) &= 2Q_e Q_f a_e a_f Re\chi_0(s) + 4v_e a_e v_f a_f|\chi_0(s)|^2\,, \end{aligned}$$

and $\chi_0(s)$ is the Z^0 propagator. θ is the polar angle between the incoming electron, e^-, and the outgoing fermion, f, as shown in figure 1.1. The two lowest order diagrams

which contribute to the differential cross section, $d\sigma^f/d\Omega$, are also shown in figure 1.1. On the Z^0 resonance ($s = M_Z^2$) the contribution to $d\sigma^f/d\Omega$ from γ exchange and $\gamma - Z^0$ interference is small compared to that from Z^0 exchange.

Due to the chiral nature of the Standard Model [3] and the correspondence between handedness and helicity at relativistic energies, the differential cross-section is *not* forward-backward symmetric. The asymmetry, $A_{FB}^{f\bar{f}}$, is defined as

$$A_{FB}^{f\bar{f}} = \frac{\sigma_F^f - \sigma_B^f}{\sigma_F^f + \sigma_B^f} , \tag{1.12}$$

where

$$\sigma_F^f = 2\pi \int_0^1 \frac{d\sigma^f}{d\Omega} d(cos\theta), \quad \sigma_B^f = 2\pi \int_{-1}^0 \frac{d\sigma^f}{d\Omega} d(cos\theta) . \tag{1.13}$$

For light fermions ($m_f/M_Z \ll 1$), and neglecting γ exchange terms[4], the lowest order on-resonance asymmetry can be written as

$$A_{FB}^{f\bar{f}}(M_Z^2) = \frac{3}{4} \mathcal{A}_e \mathcal{A}_f \tag{1.14}$$

where

$$\mathcal{A}_f = \frac{2 v_f a_f}{v_f^2 + a_f^2} = \frac{2(1 - 4|Q_f| sin^2\theta_W)}{1 + (1 - 4(|Q_f| sin^2\theta_W)^2} . \tag{1.15}$$

The quantity $\mathcal{A}_f$ is shown in figure 1.2 as a function of $sin^2\theta_W$ for up and down type quarks and for the electron. Due simply to the magnitude of its charge $\mathcal{A}_d$ ($d = d, s, b$) is large and relatively insensitive to $sin^2\theta_W$, whereas $\mathcal{A}_e$ is very sensitive to $sin^2\theta_W$.

Therefore, in lowest order, the on-resonance asymmetry is determined completely by $sin^2\theta_W$ as given by equations (1.14) and (1.15). However, when higher order corrections

[3] A chiral theory is one in which the gauge fields couple differently left and right-handed fermions.

[4] If the finite mass of the fermions is taken into account, $A_{FB}^{f\bar{f}}$ changes by an amount far less than the precision of present experimental measurements, even for the b-quark. Also, γ exchange effects are negligible on the Z^0 resonance. Nevertheless, both effects are taken into account in the interpretation of the charge asymmetry measurement presented in chapters 3 to 8 of this thesis.

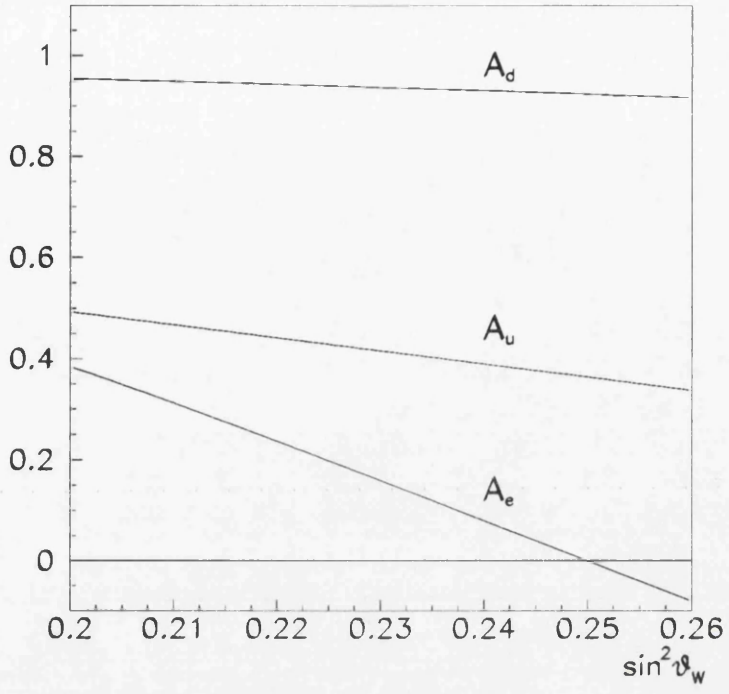

Figure 1.2: *The quantity $\mathcal{A}^f$ for quarks and leptons as a function of $sin^2\theta_W$.*

are included these equations and the relations between the parameters of the Standard Model are modified. $A_{FB}^{f\bar{f}}$ is then dependent on all the parameters, in particular on the unknown parameters M_H and m_t. The higher order corrections can be divided into the following two classes :

- **QED corrections** ; Here one of the fermions can radiate a real or virtual photon. These corrections are independent of the gauge structure of the Standard Model and require only the global parameters M_Z, Γ_Z, v_f a_f ;

- **Weak corrections** ; These include all non-QED electroweak corrections, such as loop corrections to the Z^0 and γ propagators, $\gamma - Z^0$ interference and vertex and box corrections and are dependent on the structure of the Standard Model.

In the case of hadronic final states, QCD corrections due to gluon radiation must also

be considered. The corrections have a similar structure to those of QED and can be calculated using perturbative QCD.

In the calculation of higher order contributions, infinite divergencies appear. These can be removed by replacing the 'bare' parameters in the Lagrangian by 'renormalised' parameters into which the infinities are absorbed. The legality of this renormalisation procedure can be traced to the fact that the Standard Model is a Yang-Mills theory, i.e. it is a theory with a local gauge invariance.

A common choice of input parameters, known as the 'on-shell' scheme, is[5]

$$\alpha,\ G_\mu,\ M_Z,\ M_H,\ m_f\ .$$

The advantages of this choice is that all the parameters have a clear physical meaning, can be measured directly and, apart from M_H and m_t are experimentally known.

Within the on-shell scheme the weak corrections have a structure that allow their absorption into a redefinition of the neutral current coupling constants, v_f and a_f, or equivalently a redefinition of $sin^2\theta_W$. It is this *effective* weak mixing angle, $sin^2\theta_W^{eff}$, that determines the asymmetries at the Z^0 peak. Chapters 3 to 7 of this thesis describe a measurement of the charge asymmetry $\langle Q_{FB} \rangle$ in $b\bar{b}$ decays of the Z^0 boson. $\langle Q_{FB} \rangle$ is sensitive to the underlying $b\bar{b}$ forward-backward asymmetry $A_{FB}^{b\bar{b}}$. The experimental apparatus is described in chapter 2 below.

[5] G_μ is often replaced by the $W^\pm$ boson mass, M_W, which is related to G_μ via the precise knowledge of the muon lifetime.

Chapter 2

The Experiment

In this chapter the experimental apparatus is described. Section 2.1 briefly describes the LEP collider and in section 2.2 an overview of the ALEPH experiment is given.

2.1 The LEP collider

CERN's large electron-positron collider, LEP, was built to allow precision tests of the Standard Model of particle physics through a high statistics study of the properties of the Z^0 boson. LEP is a 27 km circular storage ring constructed inside a tunnel at an average depth of 100 m at the foot of the Jura mountains near Geneva (figure 2.1). Electrons and positrons are accelerated in four or eight bunches in opposite directions using 128 conventional radio-frequency (RF) cavities. These bunches are steered around the ring using 3368 dipole bending magnets and are made to collide at the centre of 4 large particle detectors situated in caverns around the collider. The dimensions of the beam are 'squeezed' using 816 quadrupole and 504 sextupole magnets. Beam spot dimensions of $\sim 250\ \mu$m horizontally and $\sim 15\ \mu$m vertically are achievable, giving a peak luminosity of $\sim 1.1 \times 10^{31}\ \mathrm{cm}^{-2}\mathrm{s}^{-1}$. The maximum energy achievable is 60 Gev/beam although the machine is presently run close to the Z^0 resonance at 45.6 GeV/beam.

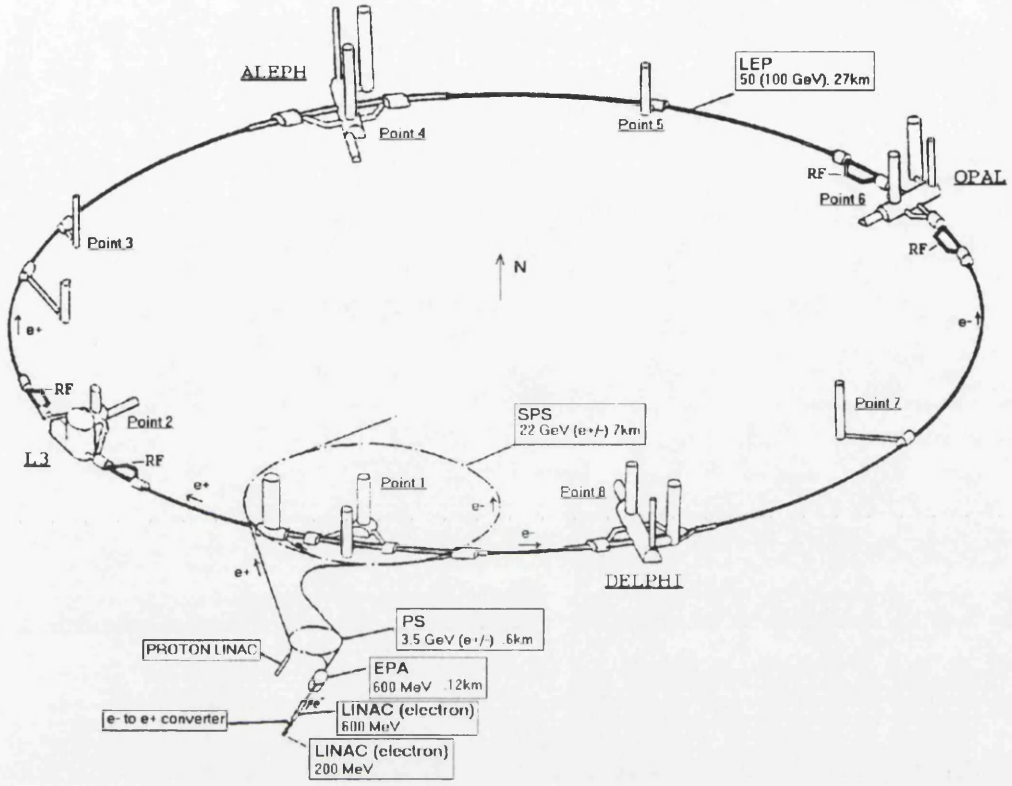

Figure 2.1: *The LEP collider.*

In LEP phase 2, scheduled to begin early in 1996, the addition of 192 superconducting radio-frequency cavities will enable beam energies of up to 90 GeV to be reached. This will allow the experiments to measure the W mass and couplings via W^+W^- production, and to search for new particles and phenomena.

2.2 The ALEPH detector

ALEPH [12], shown in figure 2.2, is one of the four large particle detectors situated around the LEP collider. Its role is to determine, as accurately as possible, the nature, direction and energy of each particle created in a collision of a positron and an electron. The number of particles created varies with each collision, but is around 40

on average. ALEPH is made up of independent modular subdetectors, arranged as a central cylindrical 'barrel' section closed by two 'endcaps', and covering almost 4π solid angle. The dimensions of the detector are approximately 12×12×12 m and its weight is about 3000 tons.

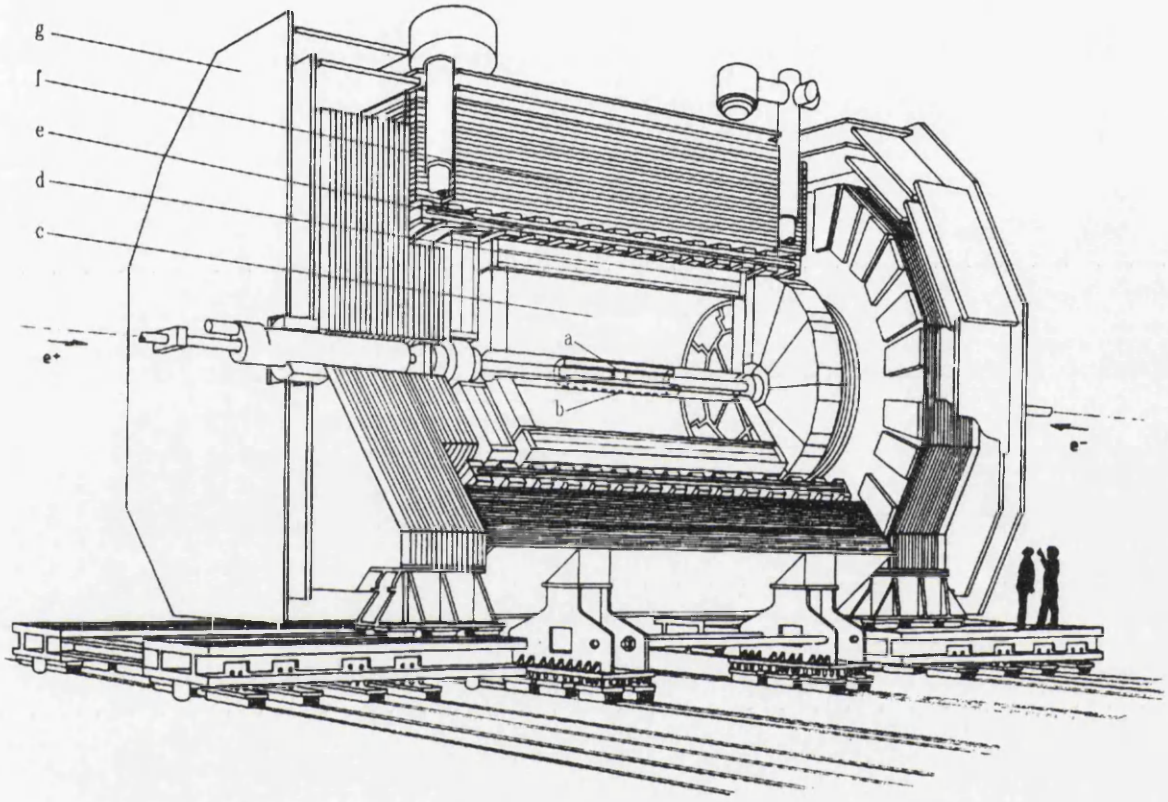

Figure 2.2: *Schematic diagram of the ALEPH particle detector ; (a) silicon vertex detector (VDET), (b) inner tracking chamber (ITC), (c) time projection chamber (TPC), (d) electromagnetic calorimeter (ECAL), (e) superconducting solenoid, (f) hadronic calorimeter (HCAL) and (g) the muon chambers (MUON).*

Nearest to the beam is a silicon strip micro vertex detector (VDET) used to tag the presence of heavy flavour hadrons through precision tracking of their decay products. Surrounding this is a cylindrical multiwire drift chamber, the inner tracking chamber (ITC), which provides track coordinates in r and ϕ and is used for triggering. Outside

the ITC is the primary tracking device of ALEPH, a large time projection chamber (TPC) providing 3-dimensional track coordinates. A finely segmented electromagnetic sampling calorimeter (ECAL) consisting of alternate layers of lead sheets and proportional tubes, lies outside the TPC. All of these subdetectors are enclosed within a superconducting coil which provides a uniform 1.5 Tesla magnetic field used for charge and momentum measurement. The flux is returned in a large iron structure that both supports the experiment and is a fully instrumented hadron calorimeter (HCAL). Limited streamer tubes fill hollow slots in the (HCAL) and produce a digital pattern, as well as an analogue signal from projective towers for energy measurement. Finally, 92% of the solid angle is surrounded by muon chambers which measure two 3-dimensional coordinate for each penetrating charged particle. The luminosity is measured using three separate luminosty calorimeters (LCAL, SICAL and BCAL) covering progressively smaller angles.

2.2.1 Tracking

The silicon strip vertex detector

The primary motivation for the construction of silicon strip micro vertex detectors at LEP was the potential to tag the presence of heavy flavour (charm and beauty) hadrons through their lifetime. The ALEPH silicon vertex detector (VDET) [13] is shown in figure 2.3. Two layers of silicon strip detectors are arranged in two concentric barrels around the beampipe with average radii 6.5 cm and 10.7 cm and length 20.0 cm. The solid angle coverage with active detector is 87% and 75% for the inner and outer layers respectively.

The silicon strip detectors have readout strips on both sides. The strips on one side are parallel to the beam direction and measure the azimuthal angle ϕ and the strips on the other side are perpendicular to the beam and measure the z coordinate. With the

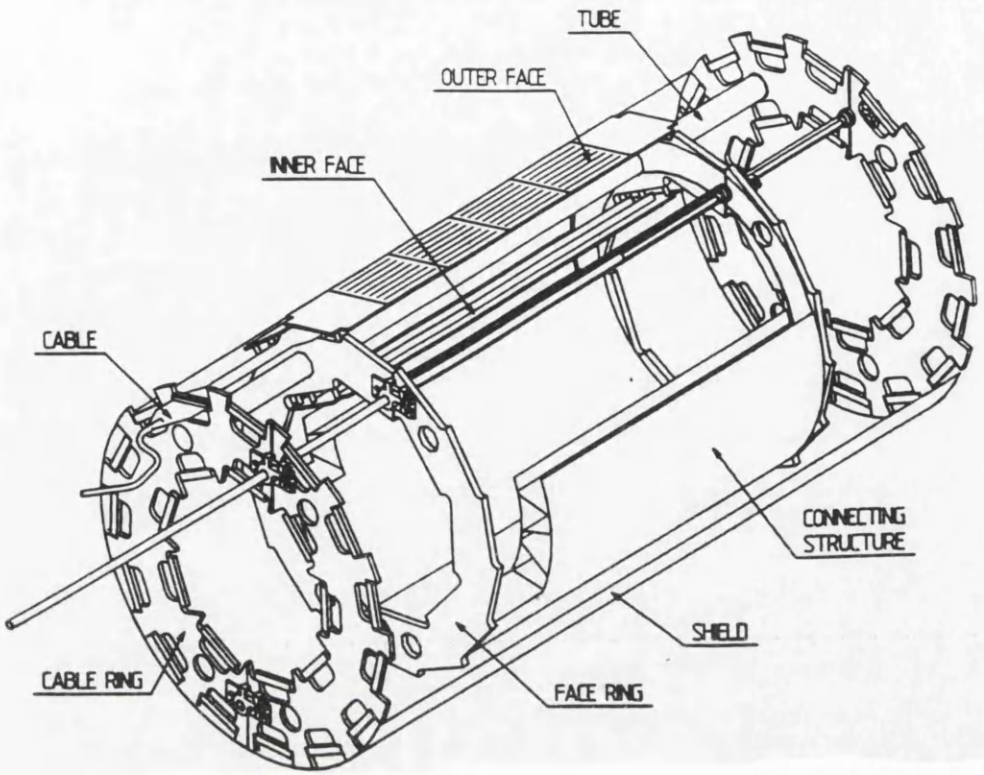

Figure 2.3: *Schematic diagram of the VDET silicon vertex detector.*

radius r given by the mechanical holding frame, the position of a single particle hit is determined in cylindrical coordinates (r, ϕ, z).

The readout of the detectors in both the ϕ and z side is performed with custom designed VLSI CMOS amplifier chips, the CAMEX 64. The total number of analogue readout channels is 73 728.

At normal incidence a particle traverses on average an amount of material equivalent to $\sim$ 4.1% of a radiation length. The point resolution of tracks at perpendicular incidence is found to be 12 μm in $r - \phi$ and 10 μm in z. The addition of two very high precision VDET points onto the helix of a given charged track, measured using the ITC and/or the TPC, improves the momentum resolution by $\sim$ 25% from $\Delta p/p = 8.8 \times 10^{-4} \cdot p$ to $\Delta p/p = 6.6 \times 10^{-4} \cdot p$.

The inner tracking chamber

The inner tracking chamber (ITC), is a conventional drift chamber 2 metres long and positioned outside the VDET. It contains 960 sense wires strung between two aluminium endplates, each sense wire being surrounded by field wires in a hexagonal cell. The cells are organised into eight concentric layers ; the four inner layers having 96 cells and the four outer, 144 cells. By measuring the drift time the $r-\phi$ coordinate is measured with a precision of about 100 μm. The z-coordinate is measured using charge division with a precision of 30 mm.

As well as providing precise $r-\phi$ track coordinates the ITC, due to its fast response time, is used to provide tracking information to the level 1 trigger.

The time projection chamber

The time projection chamber (TPC) [14], shown in figure 2.4, provides most of the charged track information in ALEPH. It has an inner radius of 0.3 m and an outer radius of 1.8 m, and is 4.7 m long. It provides up to 21 3-dimensional space points per track and samples their ionisation energy loss ($\frac{dE}{dX}$) up to 340 times.

Each end of the TPC is almost at ground potential and at the centre there is a membrane of graphite coated mylar at -26 kV. Together with the inner and outer field cages these create a uniform field at approximately 115 V/cm. Ionization electrons drift from their production point to segmented proportional chambers on each end of the TPC, where gas multiplication takes place. The magnetic field limits diffusion in the $r-\phi$ plane. Cathode readout in the proportional chambers is via 21 concentric pad rows, each pad being 6.2 mm long in the azimuthal direction and 30 mm in the radial direction. The accurate position measurement of 180 μm at 0° in $r-\phi$ is derived from the sharing of induced charge between a number of neighbouring cathode pads. The z coordinate is derived from measurements of the drift time with a resolution of about 1 mm. The momentum resolution of the TPC alone is $\Delta p/p = 1.2 \times 10^{-3} \cdot p$ at 45

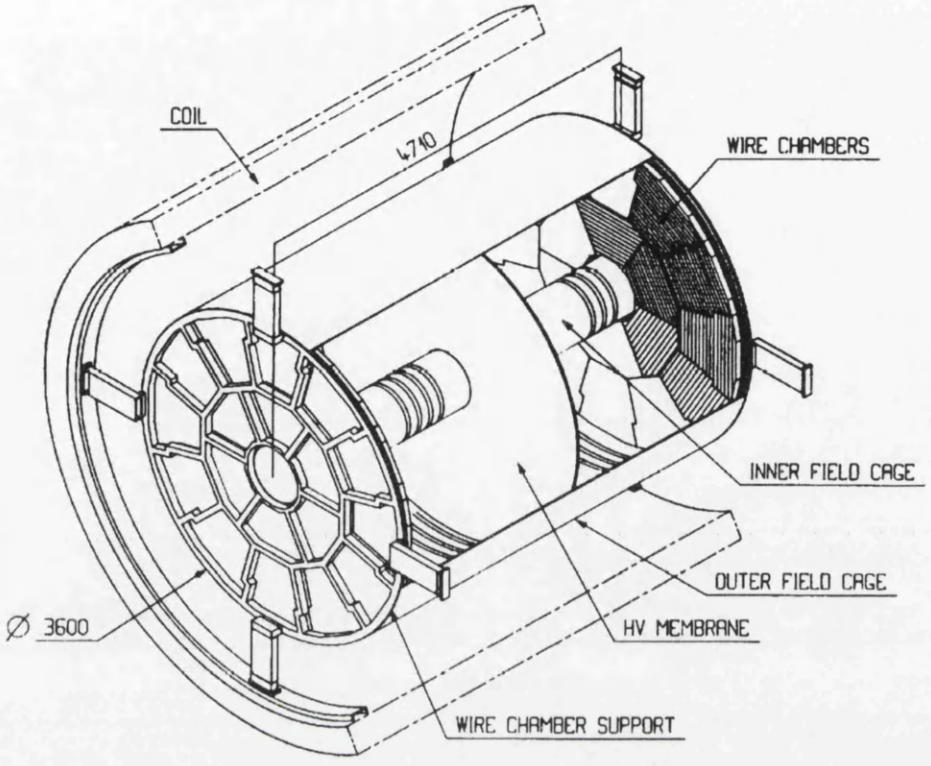

Figure 2.4: *The time projection chamber TPC.*

GeV/c. The sense wires of the proportional chambers are used for $\frac{dE}{dX}$ measurements, giving a resolution of 4.5% for Bhabha electrons. This information is used to separate charged e, μ, K and p.

Superconducting Solenoid

The ALEPH magnet is a liquid helium-cooled superconducting solenoid, creating a 1.5 Tesla magnetic field in the z direction at a current of 5000 A. The coil consists of a main winding 5.3 m in diameter and 6.35 m long and has a total weight (coil and cryostat) of 55 tons. The wire used is a niobium-titanium alloy and is operated at 4.3 Kelvin, at which temperature it is superconducting. The field occupies a volume of 123 m^3 and its z component is uniform to within 0.2 %. The radial and azimuthal components are

less than 0.4 and 0.04 % of the z component respectively.

2.2.2 Calorimetry

The electromagnetic calorimeter

The electromagnetic calorimeter (ECAL), is a sampling calorimeter and lies inside the superconducting coil to minimise the amount of material in front of it. It is built in 36 modules, 12 in the barrel and 12 in each endcap. Each module contains 45 layers of lead and proportional wire chambers. Cathode pads in each layer of the wire chambers are connected to form towers pointing towards the interaction point. Each tower is read out in 'storeys' of 4, 9 and 9 radiation lengths and has a solid angle coverage of $\sim 0.9^o \times 0.9^o$. The granularity of the pads allows the centroid of each shower to be located with angular resolution $\sigma_\phi = \sigma_\theta / sin\theta = 0.32 + 2.7/\sqrt{\mathrm{E}(GeV)}$ mrad, and the longitudinal development of the showers can be observed on the 45 wire layers providing good electron and photon id. The energy resolution of the ECAL is parameterised as $\sigma/E = 0.01 + 0.18/\sqrt{\mathrm{E}(GeV)}$.

The hadron calorimeter

The hadron calorimeter (HCAL) consists of 23 layers of iron each 50 mm thick with limited streamer tubes between each layer. Pads running perpendicular to the streamer tubes are connected in towers of solid angle $\sim 3.7^o \times 3.7^o$ pointing to the interaction point. On the other side of the tubes are aluminium strips running the whole length of each tube, their digital readout providing a 2-dimensional view of the shower profile. The energy resolution of the HCAL is $\sigma/E = 0.84/\sqrt{\mathrm{E}(GeV)}$. The signals from the streamer tubes are used by the level 2 trigger to measure the energy deposition as a function of depth.

The muon chambers

Outside the HCAL are two layers of limited streamer tubes which comprise the muon chambers. The detector elements are similar to those of the HCAL with the difference that they are instrumented with orthogonal strips running parallel and perpendicular to the streamer tubes rather than connecting pads together in towers of solid angle. Combined with knowledge of their position the muon chambers measure one or two 3-dimensional space points for each track penetrating the HCAL. Together with the HCAL the muon chambers are used to identify muons. For 95% efficiency misidentification of hadrons is $\sim 1\%$.

2.2.3 Trigger

The philosophy of the ALEPH trigger is to record every e^+e^- collision. The trigger consists of three levels, sensitive to single particles or single jets. The level 1 and 2 triggers consist of specially built hardware that looks for signals in coarse segments of the HCAL, ECAL, LCAL, ITC and TPC.

The level 1 trigger decides whether or not to initiate digitization of the event. The principal level 1 triggers in ALEPH are :

- ECAL energy greater than 6.5 GeV in the barrel or 3.8 GeV in either endcap or greater than 1.6 GeV in both endcaps in coincidence ;
- ECAL energy greater than 1.3 GeV in a module in the same azimuthal region as an ITC track ;
- a particle penetrating HCAL in the same azimuthal region as an ITC track.

A number of subsidiary triggers provide high redundancy and allow trigger efficiencies to be precisely determined.

Level 2 serves only to verify a level 1 trigger by replacing ITC tracking information

with more accurate TPC information available 50 μs after the beam crossing. A level 2 'yes' initiates full readout of the detector.

The level 3 trigger involves software analysis of the full detector readout and is used to reject background such as beam gas interactions and off-momentum particles hitting the vacuum chamber or collimators. Very loose criteria are applied to ensure that all physics events are saved for analysis. The efficiency of the trigger is 100 % for hadronic Z^0 decays, $\sim$ 100 % for leptonic Z^0 decays and $99.7 \pm 0.2\%$ for Bhabha events.

2.2.4 Data acquisition

ALEPH consists of hundreds of thousands of subdetector elements each delivering 500 Mbytes of raw data per second. A highly sophisticated data aquisition (DAQ) system is required to format and reduce the data to an acceptable level to be written on tape, minimize the dead time and synchronize the data from each event.

Data reduction is achieved using the trigger system described in the previous section and by a process known as 'zero suppression' where only those channels which have signals above certain thresholds are read out. The DAQ has a modular structure to match that of the detector and has a tree-like heirarchy with no communication between elements on the same level.

The task of each element at each level of the hierarchy is as follows :

- **Read out controllers (ROCs).** Once triggered, the ROCs read out the sub-detector specific 'front-end' electronics, apply calibration procedures if required and format the data.

- **Event builders (EBs)** The EBs receive data from the ROCs and build a sub-event at sub-detector level.

- **Main event builder (MEB).** The MEB combines the sub-events from the various EBs and forms the complete event.

- **The event processor (EP).** The EP (level 3 trigger) performs data reduction on the complete event.

- **The host computer.** The host computer stores the data on disk and provides facilities for on-line event display and detector performance monitoring.

- **Event reconstruction.** The event reconstruction in ALEPH is done 'quasi-online' in a dedicated facility which outputs the reconstructed events to tape which are then taken to the main CERN computer centre for storage and offline analysis.

The operating conditions of the subdetectors such as voltages, temperatures, power supplies, gas control etc. are controlled using a 'Slow Control' system. The system detects any faults from the subdetectors and the associated electronics during data taking. This information is then recorded with the rest of the event information.

2.3 Monte Carlo simulation

All Monte Carlo simulated data referred to in this thesis were produced using the HVFLO3 physics generator. HVFLO3 is based on JETSET 7.3 [8] with the modification that $e^+e^- \rightarrow q\bar{q}$ events are generated using DYMU3 [16], which includes an improved treatment of initial state radiation. Final state gluon and photon radiation is simulated in JETSET 7.3. Also the simulation of certain inclusive and exclusive charmed and beauty hadron decays are modified to reflect recent experimental observation.

Detector simulation is performed in the GEANT [17] framework. 'Hits' are produced in tracks in the tracking detectors and are smeared by the appropriate resolution and used to produce 'raw data' containing the same information as real events. Showers in calorimeters are developed using GEANT tables and algorithms, but electron and positron showers are parameterized using parameterisations established from test beam data.

Chapter 3

The forward-backward charge asymmetry

The following chapters describe a measurement of the forward-backward charge asymmetry, $\langle Q_{FB} \rangle$, in $b\bar{b}$ decays of the Z^0 boson. $\langle Q_{FB} \rangle$ is sensitive to the underlying $b\bar{b}$ forward-backward asymmetry, $\mathcal{A}_{FB}^{b\bar{b}}$. When interpreted in terms of the Standard Model, $\mathcal{A}_{FB}^{b\bar{b}}$ can be used to estimate the effective electroweak mixing angle, $sin^2\theta_W^{eff}$, which is a prediction of the model once M_Z, M_H and m_t are known.

Section 3.1 introduces the forward-backward charge asymmetry, $\langle Q_{FB} \rangle$, and in section 3.2 the relationship between $\langle Q_{FB} \rangle$ and $\mathcal{A}_{FB}^{b\bar{b}}$ is described.

3.1 The forward-backward charge asymmetry, $\langle Q_{FB} \rangle$

Previous electroweak [18] and mixing [19] measurements have made use of the quark charge retention properties of jets. As quarks are not observed directly, their charges have to be inferred from the resulting hadronic final state. This is achieved by using a weighted charge method originally proposed by Field and Feynman [20]. This method is based on the premise that there is a high probability that the original quark is contained in one of the leading hadrons.

In each event the direction of the primary quark is estimated using the thrust axis, $\vec{t}$, defined as the unit vector that maximises

$$\frac{\sum_{i=1}^{N} |\vec{t} \cdot \vec{p}_i|}{\sum_{i=1}^{N} |\vec{p}_i|},$$

where p_i is the momentum of track i and the summation is over all reconstructed charged and neutral tracks[1]. The thrust vector, $\vec{t}$, is chosen to point in the forward direction defined by the direction of the electron beam as shown in figure 3.1.

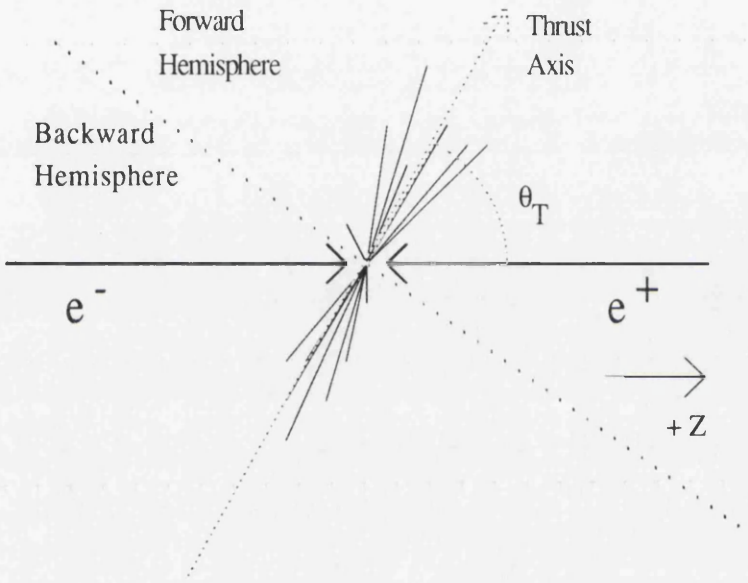

Figure 3.1: *Schematic diagram showing the thrust axis and the forward and backward hemispheres.*

Each event is split into two hemispheres by a plane perpendicular to the thrust axis. The *hemisphere charge*, Q_F, of the forward hemisphere is defined as

$$Q_F = \frac{\sum_{\vec{t} \cdot \vec{p}_i > 0} q_i |\vec{t} \cdot \vec{p}_i|^\kappa}{\sum_{\vec{t} \cdot \vec{p}_i > 0} |\vec{t} \cdot \vec{p}_i|^\kappa}, \tag{3.1}$$

[1] The reconstruction of the four-momenta of all charged and neutral particles in an event is described in [21]

where q_i and p_i are the charge and momentum of track i and κ is a weighting parameter chosen to optimise the sensitivity of the measurement. Q_B is defined similarly for the backward hemisphere.

The forward-backward charge asymmetry, $\langle Q_{FB} \rangle$, is defined as the mean forward-backward hemisphere charge difference averaged over all events :

$$\langle Q_{FB} \rangle = \langle Q_F - Q_B \rangle \, . \tag{3.2}$$

For a single quark flavour, f, $\langle Q_{FB}^{f\bar{f}} \rangle$ is non-zero due to an underlying forward-backward

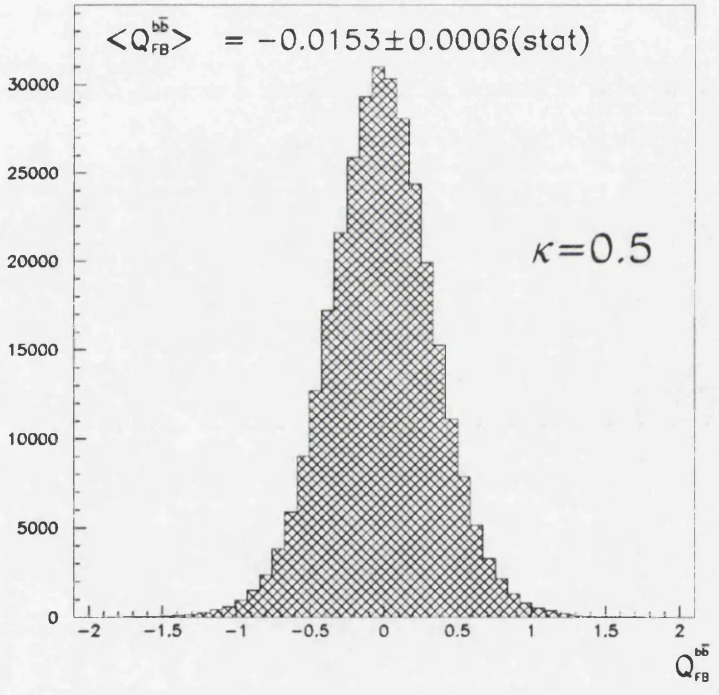

Figure 3.2: *The forward-backward hemisphere charge difference distribution in Monte Carlo $b\bar{b}$ events for $\kappa = 0.5$. The mean is shifted from zero due to the underlying forward-backward asymmetry in the direction of the final state b quark.*

asymmetry in the angular distribution of the final state quark, $A_{FB}^{f\bar{f}}$, the origin of which is described in chapter 1. Figure 3.2 shows the forward-backward charge difference

distribution in Monte Carlo $b\bar{b}$ events for $\kappa = 0.5$.

In reality the event sample consists of a mixture of u, d, s, c and b events and the measured $\langle Q_{FB} \rangle$ is the sum of the five $\langle Q_{FB}^{f\bar{f}} \rangle$, each weighted with its corresponding sample purity, $\mathcal{P}^f$:

$$\langle Q_{FB} \rangle = \sum_{f=u,d,s,c,b} \langle Q_{FB}^{f\bar{f}} \rangle \, \mathcal{P}^f \quad . \tag{3.3}$$

In this analysis, $b\bar{b}$ events are tagged preferentially by identifying large impact parameter charged tracks belonging to the decay products of long-lived b hadrons. A b purity, $\mathcal{P}^b$, of $\sim 90\%$ can be obtained, in which case the measured $\langle Q_{FB} \rangle$ is very sensitive to the $b\bar{b}$ asymmetry, $\mathcal{A}_{FB}^{b\bar{b}}$.

3.2 Relationship between $\langle Q_{FB} \rangle$ and $\mathcal{A}_{FB}^{b\bar{b}}$

For a single quark flavour, f, $\langle Q_{FB} \rangle$ can be written as :

$$\langle Q_{FB}^{f\bar{f}} \rangle = \frac{N_F^f \langle Q_{FB}^f \rangle + N_F^{\bar{f}} \langle Q_{FB}^{\bar{f}} \rangle}{N_F^f + N_F^{\bar{f}}} \quad ,$$

where N_F^f is the number of events in which the quark, f, is produced in the forward hemisphere and $\langle Q_{FB}^f \rangle$ is the mean forward-backward charge difference averaged over all such events, etc. Using the trivial relation, $\langle Q_{FB}^f \rangle = -\langle Q_{FB}^{\bar{f}} \rangle$, equation (3.2) can be written as

$$\langle Q_{FB}^{f\bar{f}} \rangle = \langle Q_{FB}^f \rangle \, \frac{N_F^f - N_F^{\bar{f}}}{N_F^f + N_F^{\bar{f}}} \quad ,$$

or

$$\langle Q_{FB}^{f\bar{f}} \rangle = \delta^f \, \frac{N_F^f - N_F^{\bar{f}}}{N_F^f + N_F^{\bar{f}}} \quad , \tag{3.4}$$

which defines the *quark charge separation*, $\delta^f = \langle Q_{FB}^f \rangle$.

Figure 3.3 shows the forward-backward charge difference distribution in Monte Carlo $u\bar{u}$ events where the u or $\bar{u}$ quark is produced in the forward hemisphere. The difference between the means of the distributions demonstrates that it is possible

to distinguish, at hadron level, between a u and a $\bar{u}$ quark going into the forward hemisphere. Similar distributions are obtained for the other quark flavours.

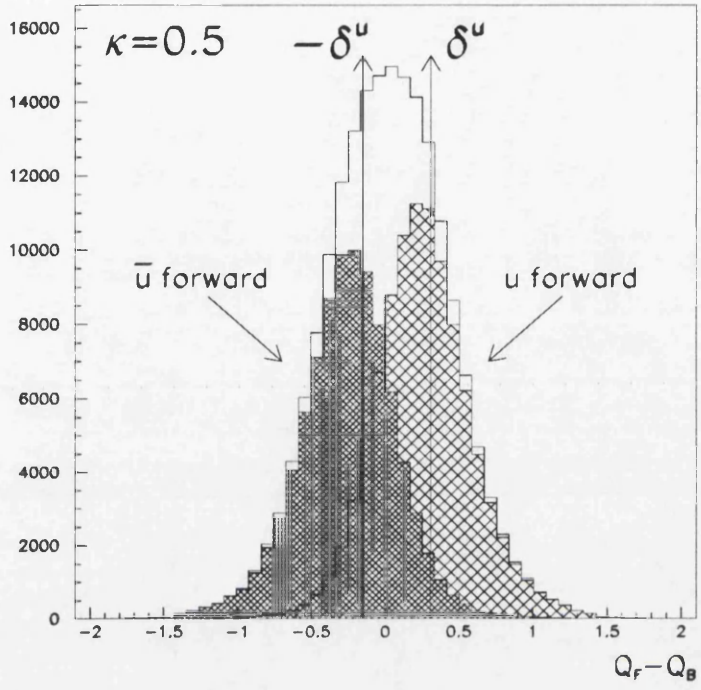

Figure 3.3: *The u charge separation δ^u in Monte Carlo simulated data for $\kappa = 0.5$.*

If the tagging efficiency of $f\bar{f}$ events is uniform over the whole $\cos\theta$ range, then the number of events in which the quark is produced in the forward direction, N_F^f, is proportional to the corresponding cross-section, σ_F^f, and the forward-backward asymmetry, $\mathcal{A}_{FB}^{f\bar{f}}$, can be written as

$$\mathcal{A}_{FB}^{f\bar{f}} = \frac{N_F^f - N_F^{\bar{f}}}{N_F^f + N_F^{\bar{f}}} \ .$$

However, the event tagging efficiencies, ε^f, are *not* uniform over the whole angular range, but fall towards zero near the edge of the VDET acceptance, as shown in figure 3.4 using Monte Carlo simulated data. If the maximum $\cos\theta$ acceptance is c, the following

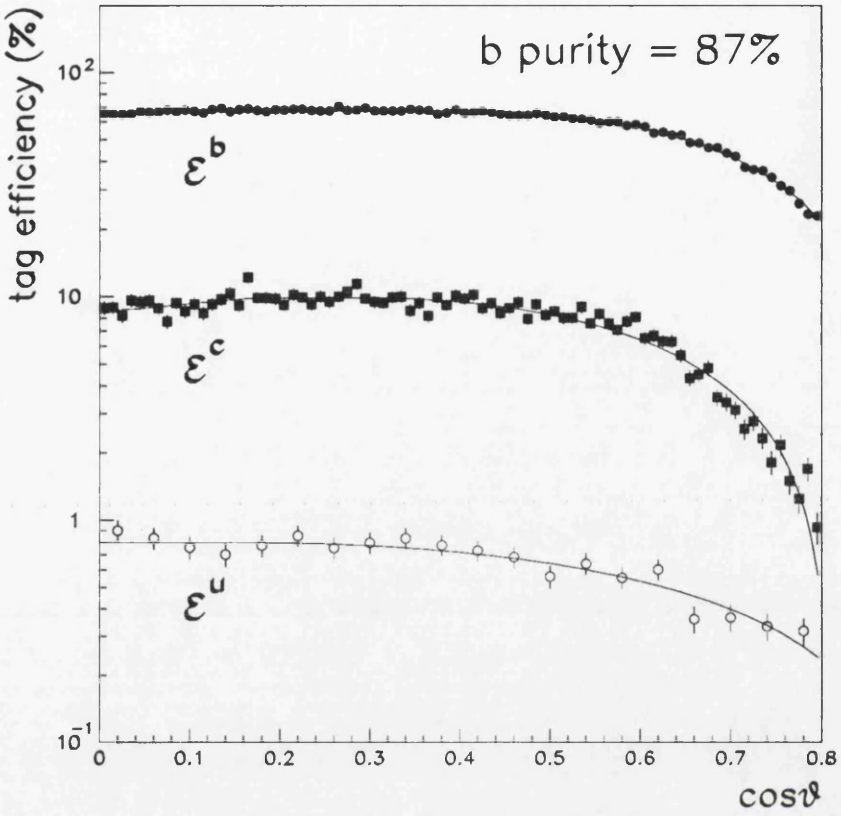

Figure 3.4: *Event tagging efficiencies ε^f in Monte Carlo simulated data.*

relation holds :

$$\frac{N_F^f - N_F^{\bar{f}}}{N_F^f + N_F^{\bar{f}}} = \frac{\int_0^c \frac{d\sigma^f}{d\Omega}\varepsilon^f(cos\theta)d(\cos\theta) - \int_{-c}^0 \frac{d\sigma^f}{d\Omega}\varepsilon^f(\cos\theta)d(cos\theta)}{\int_{-c}^c \frac{d\sigma^f}{d\Omega}\varepsilon^f(\cos\theta)d(cos\theta)} .$$

The tagging efficiencies, ε^f, are symmetric functions, so the only term remaining of the numerator is that corresponding to the anti-symmetric $cos\theta$ term in the differential cross-section (1.11). For the same reason this term disappears from the denominator. The coefficient of this term is proportional to the asymmetry, $\mathcal{A}_{FB}^{f\bar{f}}$, and so the asymmetry drops out as a multiplicative factor :

$$\frac{N_F^f - N_F^{\bar{f}}}{N_F^f + N_F^{\bar{f}}} = C^f \, \mathcal{A}_{FB}^{f\bar{f}} . \tag{3.5}$$

The flavour dependent *acceptance factors*, C^f, depend on the form of the differential cross section and tagging efficiencies. Inserting equation (3.5) into equation (3.4) gives

$$\langle Q_{FB}^{f\bar{f}} \rangle = \delta^f \; C^f \; \mathcal{A}_{FB}^{f\bar{f}} \quad . \tag{3.6}$$

Finally, equations (3.6) and (3.3) give, for the forward-backward charge asymmetry :

$$\langle Q_{FB} \rangle = \sum_{f=u,d,s,c,b} \delta^f \; C^f \; \mathcal{A}_{FB}^{f\bar{f}} \; \mathcal{P}^f \quad . \tag{3.7}$$

Equation (3.7) contains all the elements of the analysis and will be referred to in the following chapters.

The forward-backward charge asymmetry, $\langle Q_{FB} \rangle$, is measured in the hadronic data sample collected in 1992 using different κ values and different cuts on the impact parameter tag. The values obtained are presented in chapter 6. The evaluation of the charge separations, δ^f, are described in chapter 5. The u, d, s and c background charge separations are determined using Monte Carlo simulation and the b separation is measured in data. Chapter 4 gives a description of the impact parameter tag used to identify $b\bar{b}$ events. The evaluation of the purities, $\mathcal{P}^f$, and acceptance factors, C^f, are discussed there in detail. The most critical input to equation 3.7 are $\mathcal{P}^b$ and δ^b, both of which are determined using very little Monte Carlo simulation. Consequently, the interpretation of the measurement is insensitive to theoretical uncertainties in the kinematics of b decays and in the fragmentation of heavy quarks. Finally, in chapter 7, $\langle Q_{FB} \rangle$ is interpreted in terms of the Standard Model and $\mathcal{A}_{FB}^{b\bar{b}}$ and $sin^2\theta_W$ are determined.

Chapter 4

Tagging $Z^0 \rightarrow b\bar{b}$ decays using track impact parameters

For a precision measurement of $A_{FB}^{b\bar{b}}$ it is desirable that $Z^0 \rightarrow b\bar{b}$ decays be identified with a high efficiency and purity. This chapter describes the method used in the asymmetry measurement. Those results relevant to the measurement are presented.

The b hadrons produced in Z^0 decays are found primarily in $b\bar{b}$ events. By detecting signatures of these b hadrons, via their large mass and long lifetime, it is possible to select $b\bar{b}$ events with good efficiency and little background. In this analysis, *track impact parameters* are used to tag b hadrons. The algorithm relies on the precision tracking afforded by the ALEPH double-sided silicon vertex detector (VDET) and is described in [22]. Section 4.1 summarise the main stages of the algorithm.

The asymmetry measurement requires an accurate determination of the quark tagging efficiencies. Section 4.2 describes an ALEPH measurement of the $Z^0 \rightarrow b\bar{b}$ branching fraction, $\Gamma^{b\bar{b}}/\Gamma^{had}$, using the impact parameter tag [23]. Within this analysis the *uds* and *c* efficiencies are determined using a combination of Monte Carlo simulation and information within data. Their values are then used to estimate values for the b efficiency and $\Gamma^{b\bar{b}}/\Gamma^{had}$ by measuring the relative rates of single and double tagged

events. The method is insensitive to Monte Carlo modelling of b quark production and of b hadron production and decay properties.

Finally, section 4.3 describes a study of the angular dependence of the tag, an accurate modelling of which is crucial for the asymmetry measurement. The flavour dependent acceptance factors introduced in chapter 3 are evaluated.

4.1 The impact parameter tag

4.1.1 Track impact parameters

The impact parameter, δ, of a charged particle's trajectory is its distance of closest approach to the Z^0 decay point. Figure 4.1 shows a schematic diagram of a b hadron

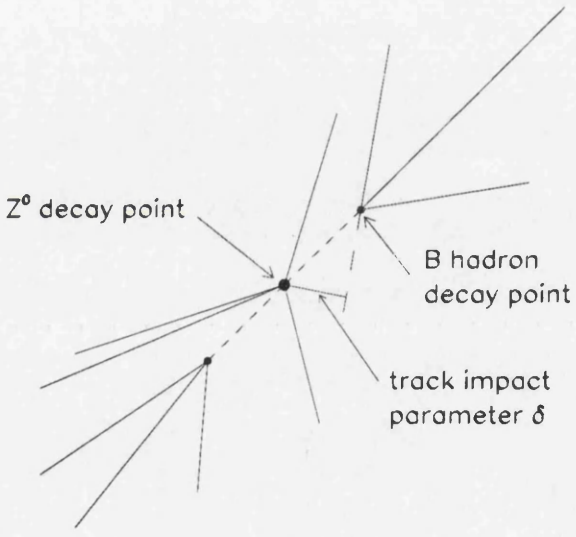

Figure 4.1: *Schematic diagram of a b hadron decay*

decay, with the impact parameter of one of its decay products indicated. The b hadrons produced in Z^0 decays typically travel 2-3 mm, before decaying into about 5 charged particles, including the decay products of secondary charmed hadrons. The masses of the final decay products are an order of magnitude less than those of the b hadrons themselves, resulting in highly energetic decays. Consequently, $b\bar{b}$ events are

characterised by the presence of many charged tracks with significant impact parameters with respect to the Z^0 decay point (or primary interaction point). Charmed hadrons have similar decay lengths to those of b hadrons, but are lighter and their decays have lower charged multiplicities ($\sim$ 2 or 3). In contrast, most of the tracks in $Z^0 \rightarrow u\bar{u}$, $d\bar{d}$, $s\bar{s}$ events originate from the primary interaction point. Therefore, by selecting events with many high impact parameter charged tracks, a high purity $b\bar{b}$ event sample can be obtained.

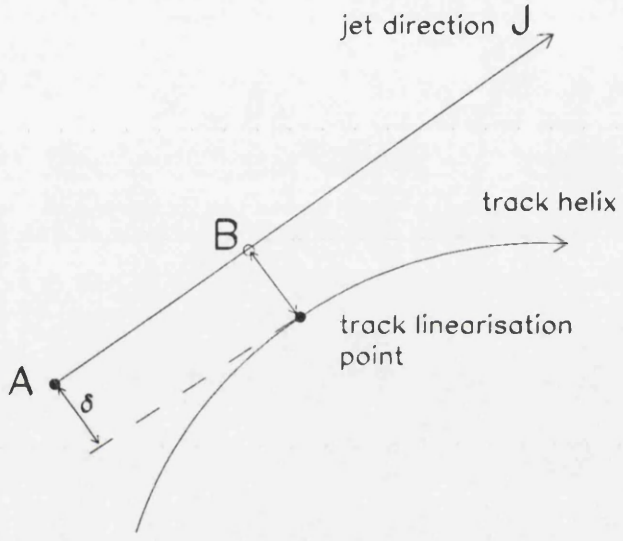

Figure 4.2: *The reconstruction of track impact parameters. **A** is the primary interaction point.*

Using the precise 3D tracking for charged tracks afforded by the VDET, accurate estimates of the true impact parameters can be made. They are measured using the following prescription (see figure 4.2). The tracks in an event are clustered into jets [24, 25], the jet definition having been optimised to reproduce the directions of b hadrons within $b\bar{b}$ events. Each track helix is linearised at the point where it is closest to its associated jet. The impact parameter, δ, of a charged track is then defined as the distance of closest approach of the corresponding linearised track to the reconstructed

primary interaction point [26], and is signed according to

$$\tilde{\delta} = sign((\overrightarrow{B} - A) \cdot \hat{J})\, \delta \ , \tag{4.1}$$

i.e. $\tilde{\delta}$ is positive if the point of closest approach of the track helix to its jet lies in that half of the event defined by the jet direction. Due to the finite experimental resolution, a random sign is assigned to tracks which originate from the primary vertex.

Using this algorithm, the measured resolution, $\sigma_{\tilde{\delta}}$, on the three dimensional impact parameter, $\tilde{\delta}$, for tracks with at least one VDET hit and momentum above 3 GeV is about 50 μm.

4.1.2 The tag variable

This section describes the processing of the impact parameters producing a variable that can be used to tag $Z^0 \rightarrow b\bar{b}$ events.

Using the reconstructed primary interaction point and the b hadron flight directions, the impact parameters of all charged tracks in an event are evaluated. The statistical resolution on the impact parameter varies as a function of momentum, angle and the number of reconstructed coordinates within the vertex detector. These functional dependences can be removed by considering, not the measured impact parameter itself, but its estimated statistical significance, $\tilde{\delta}/\sigma_{\tilde{\delta}}$. Figure 4.3 shows the signed impact parameter significance distribution in Monte Carlo simulated events. The distribution would be symmetric about zero if all tracks originated from the primary interaction point. The excess on the positive side is the lifetime signal, and is attributed to high impact parameter tracks from the decays of b hadrons and, to a lesser extent, c hadrons. The negative half of the distribution is a measure of the background under the lifetime signal.

Figure 4.4.a shows the negative half of figure 4.3 normalised to unity and the same distribution for the 1992 data. Due to imperfect modelling of the detector response the

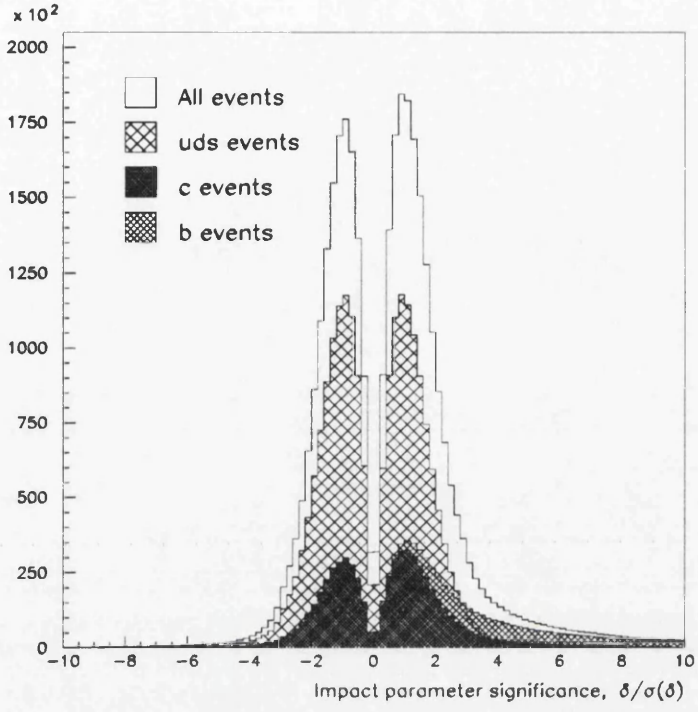

Figure 4.3: *The signed impact parameter significance distribution in Monte Carlo hadronic events.*

standard Monte Carlo does not reproduce the distributions obtained in the data. To improve the agreement an exponential smearing is applied to random Monte Carlo tracks. After applying this correction a good agreement is obtained as shown in figure 4.4.b.

The data distribution is fitted with the sum of a gaussian and two exponentials. This fit is a direct measurement of the experimental resolution of the impact parameter significance and is used to assign to a given *positive* impact parameter track, a probability P_t, that it originated from the primary interaction point. Given a track with impact parameter significance $\tilde{\delta}/\sigma_{\tilde{\delta}}$, its probability, P_t, is defined as

$$P_t(\tilde{\delta}/\sigma_{\tilde{\delta}}) = \int_{|\tilde{\delta}/\sigma_{\tilde{\delta}}|}^{+\infty} R(x)dx \,, \tag{4.2}$$

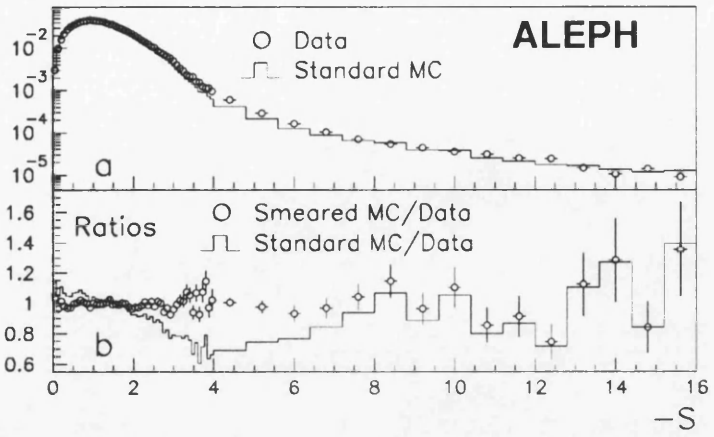

Figure 4.4: *(a.) Negative impact parameter significance distribution in data and in standard Monte Carlo data.* ($S = \tilde{\delta}/\sigma_{\tilde{\delta}}$.) *(b.) The ratio of the negative impact parameter distributions for standard and smeared Monte Carlo over data.*

where R is the fit to the negative impact parameter significance distribution. That is, $P_t(\tilde{\delta}/\sigma_{\tilde{\delta}})$ is the probability that a track originating from the primary vertex could be measured to have an impact parameter significance $\tilde{\delta}/\sigma_{\tilde{\delta}}$ or greater.

Each b hadron decays to ~ 5 charged particles, all of which can have large *positive* impact parameters. By combining the impact parameter information from all such tracks within an event, a tag variable can be constructed which can be used to distinguish $b\bar{b}$ events from those of lighter quarks.

Each event is split into two hemispheres defined by the axis of the highest energy jet. In each hemisphere the track probabilities, P_t, of those tracks with positive impact parameters are combined to form a hemisphere probability, P_h. For a hemisphere containing N positive impact parameter tracks, P_h is the probability that N tracks all originating from the primary interaction point, could reproduce the observed set of track probabilities, or any other set equally likely or more unlikely. Figure 4.5 shows

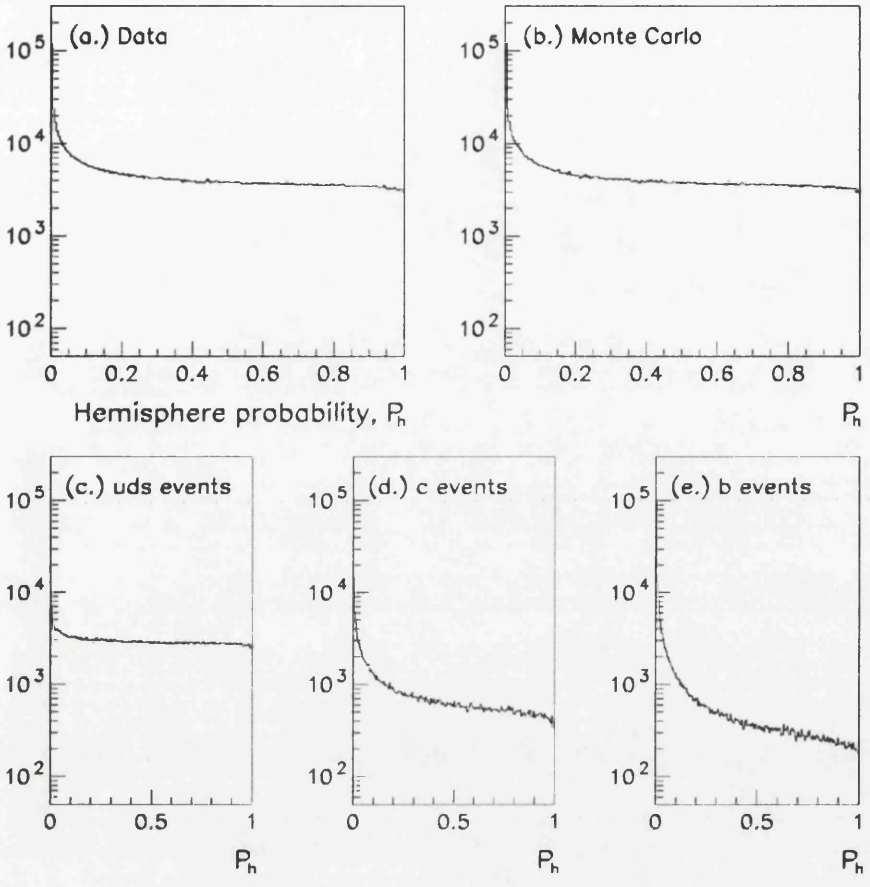

Figure 4.5: *The P_h distributions in data and Monte Carlo.*

the P_h distributions obtained in the 1992 data and in Monte Carlo simulated data. By accepting only those hemispheres with a P_h value *below* an arbitrary cut value, b hemispheres can be chosen preferentially

4.1.3 Monte Carlo hemisphere and event tagging efficiencies

Figure 4.6.a shows the hemisphere tagging efficiencies, ε_h^f (f = uds, c, b), and the b hemisphere purity obtained using Monte Carlo data for different cuts on P_h. The u, d and s hemispheres are grouped together because in Monte Carlo data they have almost

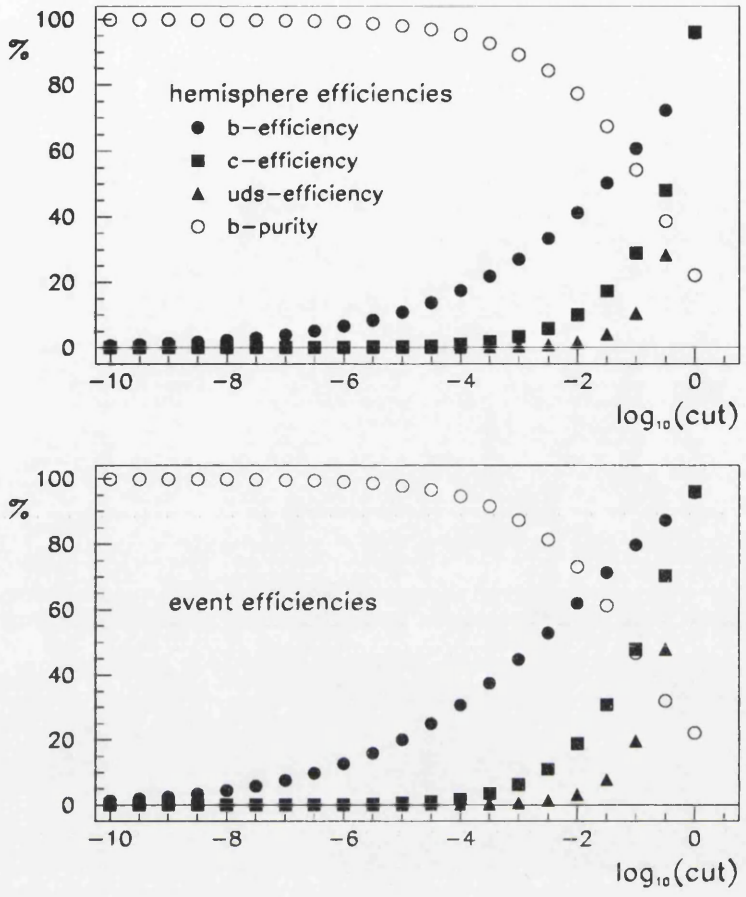

Figure 4.6: *Monte Carlo (a) hemisphere and (b) event tagging efficiencies and their corresponding b purities as a function of the cut on the tag variable* P_h.

identical tagging efficiencies.

An *event* can be tagged if *at least* one of its hemispheres passes a chosen cut on P_h. The resulting event tagging efficiencies, ε^f, are related to the hemisphere tagging efficiencies, ε_h^f, by

$$\varepsilon^f = 2\varepsilon_h^f \left(1 - c^f \varepsilon_h^f\right) + c^f \left(\varepsilon_h^f\right)^2 . \tag{4.3}$$

The c^f are correction factors which take into account any correlations between the tagging probabilities in the two hemispheres. Their relation to the classically defined

correlations is given in the next section. Figure 4.6 shows the event tagging efficiencies, ε^f, and the corresponding b purities obtained using Monte Carlo data.

4.2 Determination of the hemisphere tagging efficiencies

This section describes the 'double-tag' method used to determine the b hemisphere tagging efficiency, ε_h^b, and the $Z^0 \to b\bar{b}$ branching fraction, $\Gamma^{b\bar{b}}/\Gamma^{had}$. The method was developed for an ALEPH measurement of $\Gamma^{b\bar{b}}/\Gamma^{had}$. The values obtained for the *uds*, c and b hemisphere tagging efficiencies are used to calculate the corresponding event tagging efficiencies required for the asymmetry measurement. Section 4.2.1 describes the method and the results are presented in section 4.2.2.

4.2.1 The 'Double Tag' method

The b hemisphere tagging efficiency, ε_h^b, and the $Z^0 \to b\bar{b}$ branching fraction, $\Gamma^{b\bar{b}}/\Gamma^{had}$, can be determined by measuring in the data the relative rates of hemispheres tagged and events where both hemispheres tag.

For a particular cut on the hemisphere probability, P_h, the total fraction of hemispheres tagged, F_h, can be written as

$$F_h = \frac{\Gamma^{b\bar{b}}}{\Gamma^{had}}\varepsilon_h^b + \frac{\Gamma^{c\bar{c}}}{\Gamma^{had}}\varepsilon_h^c + (1 - \frac{\Gamma^{c\bar{c}}}{\Gamma^{had}} - \frac{\Gamma^{b\bar{b}}}{\Gamma^{had}})\varepsilon_h^{uds} , \tag{4.4}$$

where the trivial relation, $\Gamma^{u\bar{u}} + \Gamma^{d\bar{d}} + \Gamma^{s\bar{s}} + \Gamma^{c\bar{c}} + \Gamma^{b\bar{b}} = \Gamma^{had}$ has been used. Similarly, the fraction of events where both hemispheres are tagged is given by

$$F_d = \frac{\Gamma^{b\bar{b}}}{\Gamma^{had}}\varepsilon_d^b + \frac{\Gamma^{c\bar{c}}}{\Gamma^{had}}\varepsilon_d^c + (1 - \frac{\Gamma^{c\bar{c}}}{\Gamma^{had}} - \frac{\Gamma^{b\bar{b}}}{\Gamma^{had}})\varepsilon_d^{uds} , \tag{4.5}$$

where ε_d^f are the double tag efficiencies.

Because of correlations between the tagging probabilities of the two hemispheres, $\varepsilon_d^f \neq (\varepsilon_h^f)^2$. The correlations have two main sources. Firstly, momentum conservation within an event induces a correlation between the total momentum in each hemisphere,

and since the hemisphere probabilities are inherently dependent on momentum, a correlation between the two probabilities is introduced. Secondly, the tracks in both hemispheres originate from the same point in space, the primary interaction point. Therefore, any error on the reconstructed primary vertex will introduce a correlation between the apparent lifetime in the two hemispheres, and hence on their tagging probabilities. Classically, the correlations, λ^f, are defined as

$$\lambda^f = \frac{\varepsilon_d^f - (\varepsilon_h^f)^2}{\varepsilon_h^f - (\varepsilon_h^f)^2} , \tag{4.6}$$

and are related to the correlation corrections, c^f, of section 4.1.3 by

$$c^f = \lambda^f \frac{1}{\varepsilon_h^f}\left(1 - \varepsilon_h^f\right) + 1 . \tag{4.7}$$

Only the b-hemisphere correlations need be evaluated, since the other correlations have a negligible effect on the final $\Gamma^{b\bar{b}}/\Gamma^{had}$ and ε_h^b values.

Using equation (4.6) to substitute for ε_d^f in equation (4.5) the following expression for F_d is obtained :

$$\begin{aligned} F_d &= \frac{\Gamma^{b\bar{b}}}{\Gamma^{had}}(\varepsilon_h^b)^2 + \frac{\Gamma^{c\bar{c}}}{\Gamma^{had}}(\varepsilon_h^c)^2 + (1 - \frac{\Gamma^{c\bar{c}}}{\Gamma^{had}} - \frac{\Gamma^{b\bar{b}}}{\Gamma^{had}})(\varepsilon_h^{uds})^2 \\ &+ \frac{\Gamma^{b\bar{b}}}{\Gamma^{had}}\lambda_b(\varepsilon_h^b - (\varepsilon_h^b)^2) . \end{aligned} \tag{4.8}$$

Equations (4.4) and (4.8) can then be used to solve for $\Gamma^{b\bar{b}}/\Gamma^{had}$ and ε_h^b :

$$\Gamma^{b\bar{b}}/\Gamma^{had} = \frac{(F_h - \Gamma^{c\bar{c}}/\Gamma^{had}(\varepsilon_h^c - \varepsilon_h^{uds}) - \varepsilon_h^{uds})^2}{(F_d - \Gamma^{c\bar{c}}/\Gamma^{had}(\varepsilon_h^c - \varepsilon_h^{uds})^2 - (\varepsilon_h^{uds})^2 - 2F_h\varepsilon_h^{uds} - \lambda^b\Gamma^{b\bar{b}}/\Gamma^{had}(\varepsilon_h^b - (\varepsilon_h^b)^2))} \tag{4.9}$$

and

$$\varepsilon_h^b = \frac{(F_d - \Gamma^{c\bar{c}}/\Gamma^{had}(\varepsilon_h^c - \varepsilon_h^{uds}) - F_h\varepsilon_h^{uds} - \lambda^b\Gamma^{b\bar{b}}/\Gamma^{had}(\varepsilon_b^h - (\varepsilon_h^b)^2))}{(F_h - \Gamma^{c\bar{c}}/\Gamma^{had}(\varepsilon_h^c - \varepsilon_h^{uds}) - \varepsilon_h^{uds})} . \tag{4.10}$$

These two equation are not a closed form but can be solved iteratively since λ_b is small.

4.2.2 Experimental Results

Events are required to pass the standard ALEPH hadronic event selection discussed in detail in chapter 6. In addition, the two highest momentum jets in each event must have energies of more than 10 GeV, and must lie within the polar angle acceptance, $|cos\theta| < 0.7$. These cuts give an overall acceptance of $\sim 57\%$ leaving a data sample of 398 000 hadronic events. It is important to note that this event selection is different from that used in the asymmetry analysis. This point is addressed below.

The b-hemisphere correlations, λ^b, are estimated using Monte Carlo simulation and are shown in table 4.1. The *uds* hemisphere tagging efficiency, ε_h^{uds}, has two sources ;

$P_h <$	λ^b	c^b
0.0100	-0.0217 ± 0.0032	0.9830 ± 0.0028
0.0050	-0.0227 ± 0.0039	0.9779 ± 0.0040
0.0010	-0.0220 ± 0.0040	0.9663 ± 0.0063
0.0005	-0.0212 ± 0.0035	0.9608 ± 0.0065
0.0001	-0.0201 ± 0.0027	0.9441 ± 0.0076

Table 4.1: *The b hemisphere probability correlations, λ^b, and the corrections, c^b.*

$P_h <$	ε_h^{uds}	ε_h^c
0.0100	0.0198 ± 0.0030	0.1299 ± 0.0064
0.0050	0.0117 ± 0.0021	0.0932 ± 0.0054
0.0010	0.0041 ± 0.0015	0.0415 ± 0.0036
0.0005	0.0026 ± 0.0010	0.0289 ± 0.0030
0.0001	0.0009 ± 0.0005	0.0118 ± 0.0018

Table 4.2: *The uds and c hemisphere tagging efficiencies.*

that due to real lifetime within *uds* events (eg. K_s^0 and hyperons), and that due to the finite impact parameter resolution. The latter is estimated using the negative impact parameter significance distribution of figure 4.4. The *uds* efficiency due to real lifetime and the *c* efficiency, ε_h^c, are estimated using Monte Carlo simulation. The values obtained are shown in table 4.2.

Using the hemisphere correlations of table 4.1, the background hemisphere tagging efficiencies shown in table 4.2, and $\Gamma^{c\bar{c}}/\Gamma^{had}$ constrained by the Standard Model, equations (4.9) and (4.10) are solved and the resulting solutions are presented in table 4.3. The errors shown are the total errors due to the uncertainty on each of ε_h^{uds}, ε_h^c, λ^b and the statistical errors on F_h and F_d.

$P_h <$	ε_h^b	$\Gamma^{b\bar{b}}/\Gamma^{had}$
0.0100	0.5601 ± 0.0186	0.2192 ± 0.0073
0.0050	0.5073 ± 0.0142	0.2188 ± 0.0061
0.0010	0.3949 ± 0.0081	0.2174 ± 0.0044
0.0005	0.3506 ± 0.0063	0.2188 ± 0.0039
0.0001	0.2645 ± 0.0041	0.2187 ± 0.0034

Table 4.3: *The ε_h^b and $\Gamma^{b\bar{b}}/\Gamma^{had}$ values obtained by solving equations 4.9 and 4.10.*

The *event* tagging efficiencies, ε^f, are then calculated using equation (4.3) and are shown in table 4.4. Finally, the event tagging efficiencies are used to evaluate the quark purities, $\mathcal{P}^f$, according to :

$$\mathcal{P}^f = \frac{\varepsilon^f \Gamma^{f\bar{f}}}{\sum_f \varepsilon^f \Gamma^{f\bar{f}}} . \tag{4.11}$$

Table 4.5 shows the purities obtained using the $\Gamma^{b\bar{b}}/\Gamma^{had}$ values given in table 4.3 and Standard Model values for the other branching fractions. In the electroweak interpretation of the measured forward-backward charge asymmetry the purities are calculated using equation (4.11) and $\Gamma^{b\bar{b}}/\Gamma^{had}$ is constrained to agree with its measured

$P_h <$	ε^{uds}	ε^{c}	ε^{b}
0.0100	0.0393 ± 0.0058	0.2429 ± 0.0110	0.8118 ± 0.0167
0.0050	0.0232 ± 0.0041	0.1777 ± 0.0098	0.7630 ± 0.0143
0.0010	0.0082 ± 0.0030	0.0813 ± 0.0068	0.6391 ± 0.0100
0.0005	0.0051 ± 0.0020	0.0570 ± 0.0059	0.5831 ± 0.0084
0.0001	0.0018 ± 0.0009	0.0235 ± 0.0036	0.4630 ± 0.0062

Table 4.4: *The quark event tagging efficiencies, ε^f. These are calculated using equation (4.3). The ε_h^f are taken from table 4.1 and 4.3 and the b hemisphere probability correlations, λ^b, from table 4.2.*

$P_h <$	$\mathcal{P}^u$	$\mathcal{P}^d$	$\mathcal{P}^s$	$\mathcal{P}^c$	$\mathcal{P}^b$
0.0100	2.70 ± 0.38	3.43 ± 0.48	3.74 ± 0.52	17.07 ± 0.83	73.10 ± 1.47
0.0050	1.79 ± 0.30	2.31 ± 0.39	2.61 ± 0.44	14.36 ± 0.79	78.94 ± 1.28
0.0010	0.80 ± 0.29	1.07 ± 0.38	1.32 ± 0.47	8.81 ± 0.71	88.01 ± 1.25
0.0005	0.56 ± 0.21	0.75 ± 0.28	0.92 ± 0.35	6.93 ± 0.68	90.84 ± 1.03
0.0001	0.28 ± 0.14	0.33 ± 0.17	0.41 ± 0.21	3.77 ± 0.57	95.21 ± 0.75

Table 4.5: *The sample purities, $\mathcal{P}^f$, obtained using equation (4.10).*

value for each tag cut, shown in table 4.3. In this way the correlations between the measured $\Gamma^{b\bar{b}}/\Gamma^{had}$ and ε^b values are corrrectly taken into account. The u, d, s and c branching fractions are allowed to float within their Standard Model limits.

As mentioned above, the event selection used to obtain the results in table 4.5 is different from that used in the asymmetry analysis (see chapter 6). It is important to check that the sample purities obtained are independent of the event selection used. Table 4.6 below shows the true purity values obtained when the impact parameter tag is used on Monte Carlo data satisfying each of the event selections. It is clear that there

$P_h <$	$\mathcal{P}^u$	$\mathcal{P}^d$	$\mathcal{P}^s$	$\mathcal{P}^c$	$\mathcal{P}^b$
	$\Gamma^{b\bar{b}}$ *analysis event selection*				
0.0100	2.73 ± 0.03	3.49 ± 0.04	3.81 ± 0.04	17.71 ± 0.08	72.30 ± 0.16
0.0050	1.85 ± 0.03	2.39 ± 0.03	2.68 ± 0.03	15.03 ± 0.08	78.08 ± 0.18
0.0010	0.75 ± 0.02	1.02 ± 0.02	1.24 ± 0.03	9.36 ± 0.07	87.64 ± 0.22
0.0005	0.54 ± 0.02	0.74 ± 0.02	0.90 ± 0.02	7.42 ± 0.07	90.41 ± 0.24
0.0001	0.28 ± 0.02	0.35 ± 0.02	0.42 ± 0.02	4.15 ± 0.06	94.80 ± 0.28
	$A_{FB}^{b\bar{b}}$ *analysis event selection*				
0.0100	2.72 ± 0.03	3.48 ± 0.03	3.77 ± 0.03	16.88 ± 0.07	73.20 ± 0.15
0.0050	1.85 ± 0.03	2.38 ± 0.03	2.65 ± 0.03	14.28 ± 0.07	78.87 ± 0.17
0.0010	0.76 ± 0.02	1.02 ± 0.02	1.23 ± 0.03	8.89 ± 0.07	88.13 ± 0.21
0.0005	0.54 ± 0.02	0.74 ± 0.02	0.89 ± 0.02	7.07 ± 0.06	90.77 ± 0.23
0.0001	0.29 ± 0.02	0.36 ± 0.02	0.42 ± 0.02	3.97 ± 0.06	94.97 ± 0.27

Table 4.6: *The sample purities obtained using the impact parameter tag on Monte Carlo data samples satisfying the two different event selections.*

are small but significant discrepancies in the c and, more importantly, the b purities. This effect is taken into account as an extra systematic error.

4.3 Angular dependence of the event tagging efficiencies

In this section a study of the angular dependence of the impact parameter tag is described. Section 4.3.1 describes the modelling of the angular dependence of the quark tagging efficiencies and in section 4.3.2 the resulting fits are used to calculate the flavour dependent acceptance factors introduced in chapter 3.

4.3.1 Modelling the angular dependence

The maximum polar angle coverage of the inner and outer layers of VDET are 0.84 and 0.69 respectively. As the event axis approaches the edge of the VDET acceptance some charged tracks will pass outside its angular coverage, causing the efficiency of the impact parameter tag to decrease. This effect is shown in figure 4.7 for data and Monte Carlo. The agreement is reasonable over the whole angular range. Any difference in

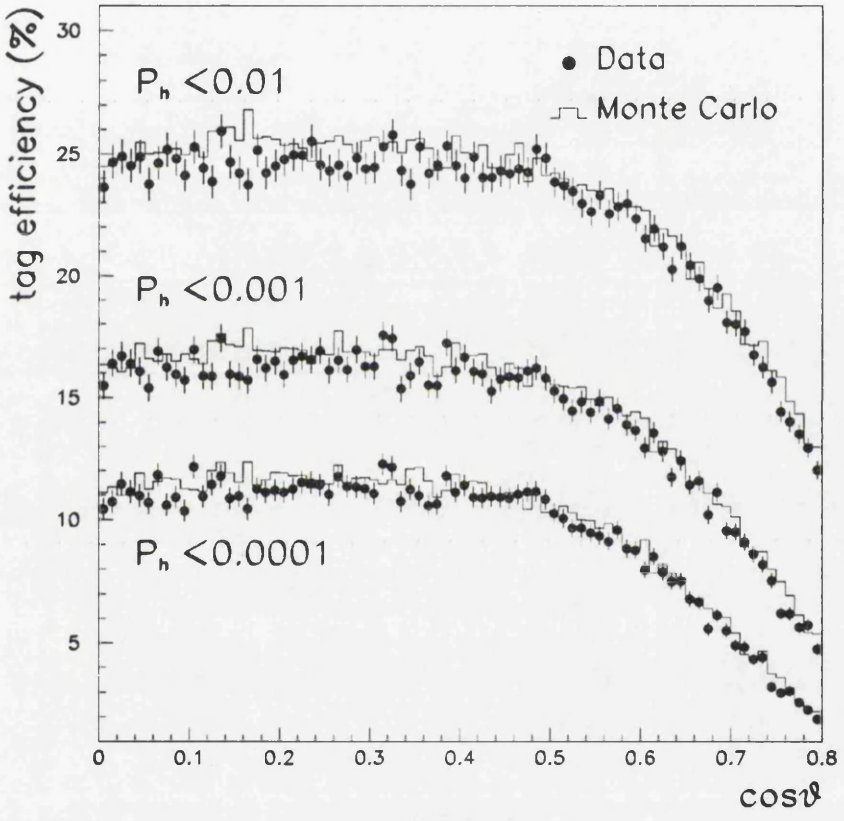

Figure 4.7: *Total event tagging efficiency, ε^{total}, in data and Monte Carlo where θ is the polar angle of the event axis. The approximate b purities corresponding to each of the cuts on P_h are, from top to bottom, 73, 88 and 95%.*

overall normalisation of data and Monte Carlo is not critical for reasons described in

section 4.3.2. What is important is that the Monte Carlo accurately models the loss of efficiency close to the edge of VDET.

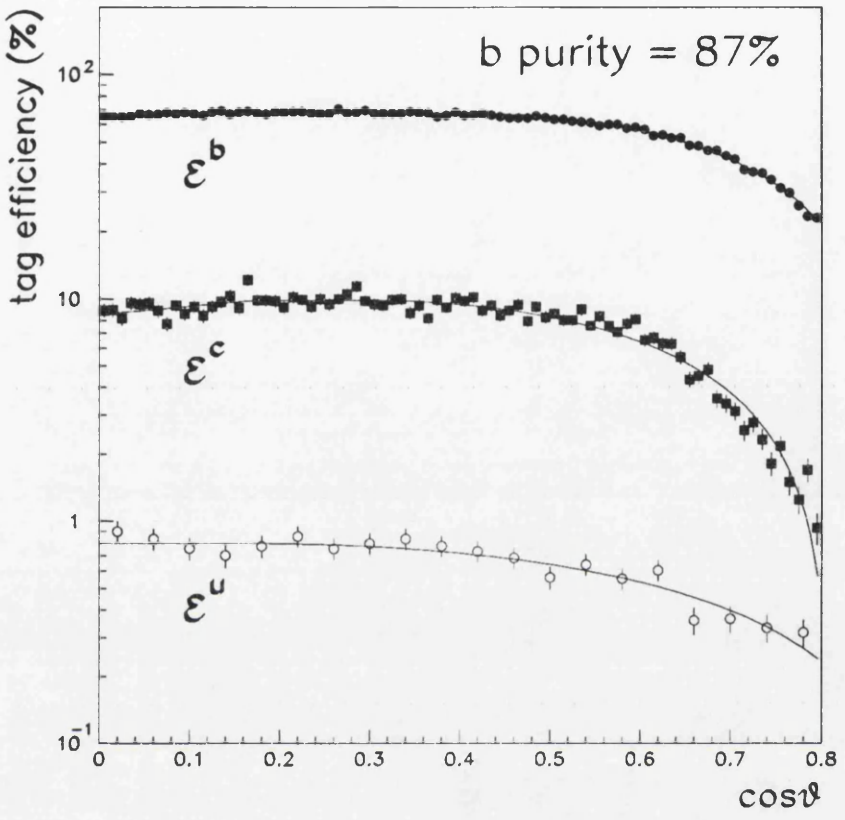

Figure 4.8: *Monte Carlo event tagging efficiencies, ε^f, as a function of the thrust axis polar angle for a tag cut of $P_h < 0.001$ which corresponds to a b purity of $\sim 87\%$.*

The angular dependence of the b, c and uds tagging efficiencies are different due to the different distribution of lifetime within their jets, as shown in figure 4.8 (note the log scale). The lifetime in u, d and s events is due in part to the finite resolution of the track impact parameter measurements as discussed in chapter 4, and is distributed evenly throughout their jets. As a result their tagging efficiencies demonstrate a gradual decrease starting close to the centre of the detector. In $c\bar{c}$ events, owing to the small c quark mass (compared to that of the b quark), the c hadron decay products are

located close to the event axis. This allows the $c\bar{c}$ event tagging efficiency to maintain a constant value out to $cos\theta = 0.5$ at which point it drops dramatically as each event loses the 2 or 3 charged tracks possessing lifetime. In contrast the decay products of b hadrons in $b\bar{b}$ events are more plentifull (~ 5) and are spread more evenly around their jet axes. Consequently, the $b\bar{b}$ event tagging efficiency shows a slower decrease at the edge of the VDET acceptance.

Each quark efficiency distribution is required for the asymmetry measurement and must be taken from Monte Carlo. However, with a b-purity of $\sim 90\%$ any systematic errors arising from uncertainties in these distributions are dominated by that of the b efficiency. Furthermore, the good agreement between data and Monte Carlo in figure 4.7 demonstrates the good Monte Carlo modelling of the angular dependence of the b-efficiency since these distributions are dominated by that of the b efficiency.

The separate b, c and uds Monte Carlo efficiency distributions are fitted with 3 parameter functions of the form

$$\varepsilon^f(cos\theta) = \begin{cases} \beta^f & \text{if } cos\theta < \alpha^f \\ \beta^f + \rho^f(cos\theta - \alpha^f)^2 & \text{if } cos\theta > \alpha^f \ . \end{cases}$$

β^f is the value of the tagging efficiency in the centre of the detector, α^f is the $cos\theta$ value at which the finite acceptance effects begin and ρ^f is the quadratic coefficient describing the fall in the efficiency at the edge of acceptance. The fits are superimposed in figure 4.8.

4.3.2 The flavour dependent acceptance factors

The above fits are used to calculate the flavour dependent acceptance constants, C^f, introduced in chapter 3 :

$$C^f A_{FB}^{f\bar{f}} = \frac{\int_{0.0}^{c} \frac{d\sigma^f}{d\Omega}\varepsilon^f(cos\theta)d(\cos\theta) - \int_{-c}^{0.0} \frac{d\sigma^f}{d\Omega}\varepsilon^f(\cos\theta)d(cos\theta)}{\int_{-c}^{c} \frac{d\sigma^f}{d\Omega}\varepsilon^f(\cos\theta)d(cos\theta)} \qquad (4.12)$$

where c is the maximum $cos\theta$ acceptance, chosen to be 0.8 corresponding to the approximate maximum acceptance of VDET. The C^f depend on the form of the differential cross section. For computational ease they are calculated using the Born level cross-section. No observable difference is seen if the fully corrected cross section is used instead. It is important to note that the overall normalisation of the efficiencies, ε^f, cancels in the ratio. Only their angular dependence is important for the evaluation of the C^f.

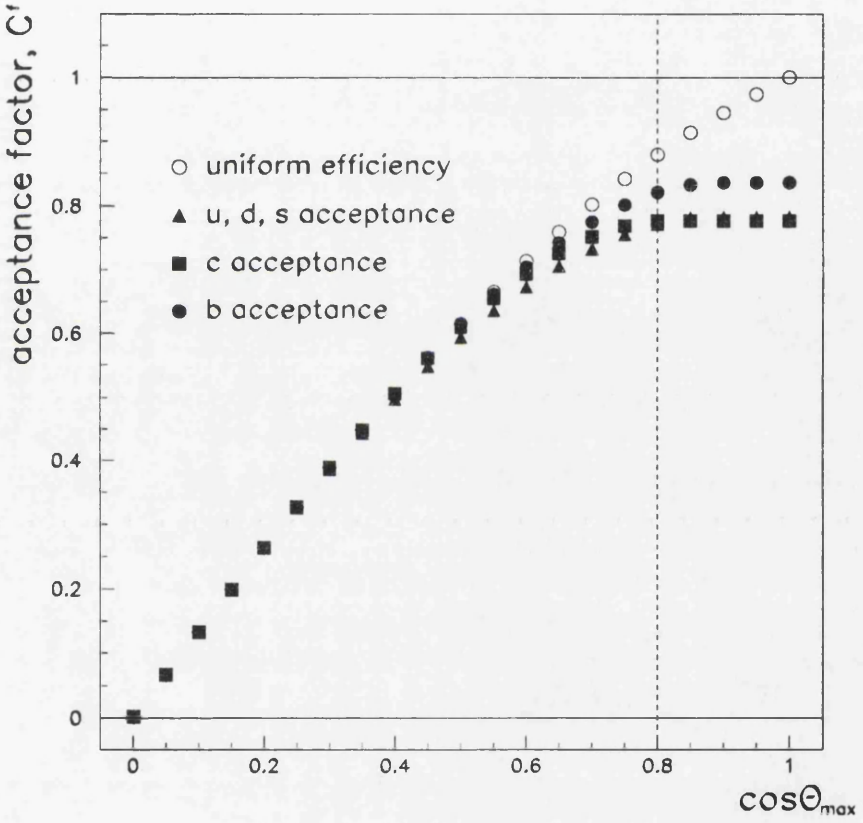

Figure 4.9: *The flavour dependent acceptance factors C^f evaluated using Monte Carlo events passing a tag cut of $P_h < 0.001$ which corresponds to a b purity of* 87%.

Figure 4.9 shows the dependence of the C^f on the maximum $cos\theta$ acceptance. The acceptance factors represent the fraction of the asymmetry 'seen' by the detector and

are equal to 1.0 if the corresponding efficiency, ε^f, is uniform over the whole angular range. C^{uds} and C^c do not increase beyond 0.8 because the efficiencies ε^{uds} and ε^c are effectively zero in this region. The small increase in C^b achieved by going beyond 0.8 in $cos\theta$ is outweighed by the lack of understanding of the performance of the lifetime-tag in that region.

$P_h <$	C^u $\pm stat \pm syst$	C^d $\pm stat \pm syst$	C^s $\pm stat \pm syst$	C^c $\pm stat \pm syst$	C^b $\pm stat \pm syst$
0.0100	0.815 $\pm 0.004 \pm 0.002$	0.818 $\pm 0.003 \pm 0.002$	0.813 $\pm 0.003 \pm 0.001$	0.811 $\pm 0.001 \pm 0.001$	0.848 $\pm 0.001 \pm 0.001$
0.0050	0.801 $\pm 0.005 \pm 0.003$	0.806 $\pm 0.004 \pm 0.003$	0.804 $\pm 0.005 \pm 0.003$	0.800 $\pm 0.002 \pm 0.002$	0.841 $\pm 0.001 \pm 0.002$
0.0010	0.790 $\pm 0.007 \pm 0.002$	0.774 $\pm 0.005 \pm 0.003$	0.772 $\pm 0.006 \pm 0.003$	0.777 $\pm 0.003 \pm 0.003$	0.822 $\pm 0.001 \pm 0.003$
0.0005	0.784 $\pm 0.015 \pm 0.011$	0.762 $\pm 0.008 \pm 0.004$	0.765 $\pm 0.008 \pm 0.005$	0.767 $\pm 0.003 \pm 0.003$	0.814 $\pm 0.001 \pm 0.003$
0.0001	0.766 $\pm 0.028 \pm 0.018$	0.730 $\pm 0.014 \pm 0.005$	0.760 $\pm 0.014 \pm 0.006$	0.743 $\pm 0.006 \pm 0.007$	0.796 $\pm 0.001 \pm 0.003$

Table 4.7: *The flavour dependent acceptance constants* C^f.

To calculate the Monte Carlo statistical error on each C^f the corresponding distribution containing the number of $f\bar{f}$ events tagged as a function of $cos\theta$ is regenerated with multinomial fluctuations in the number of entries in each bin. The corresponding efficiency distribution is fitted and C^f re-calculated. This procedure is repeated many times and the resulting spread in C^f values is taken as its statistical error. In this way the correlation between the parameters of the fit are correctly taken into account.

A systematic error is assigned to each C^f to account for any difference between

the data and Monte Carlo total tagging efficiency distributions (figure 4.7). Both distributions are regenerated as for the statistical error evaluation. They are then fitted and their ratio (data/MC) at the centre of each $cos\theta$ bin is applied as a correction to the original quark distribution, and C^f is re-calculated. This process is repeated many times and the resulting spread in C^f is added to any shift in its mean value from the Monte Carlo default value to form its systematic error. The acceptance factors and their statistical and systematic errors are shown in table 4.7.

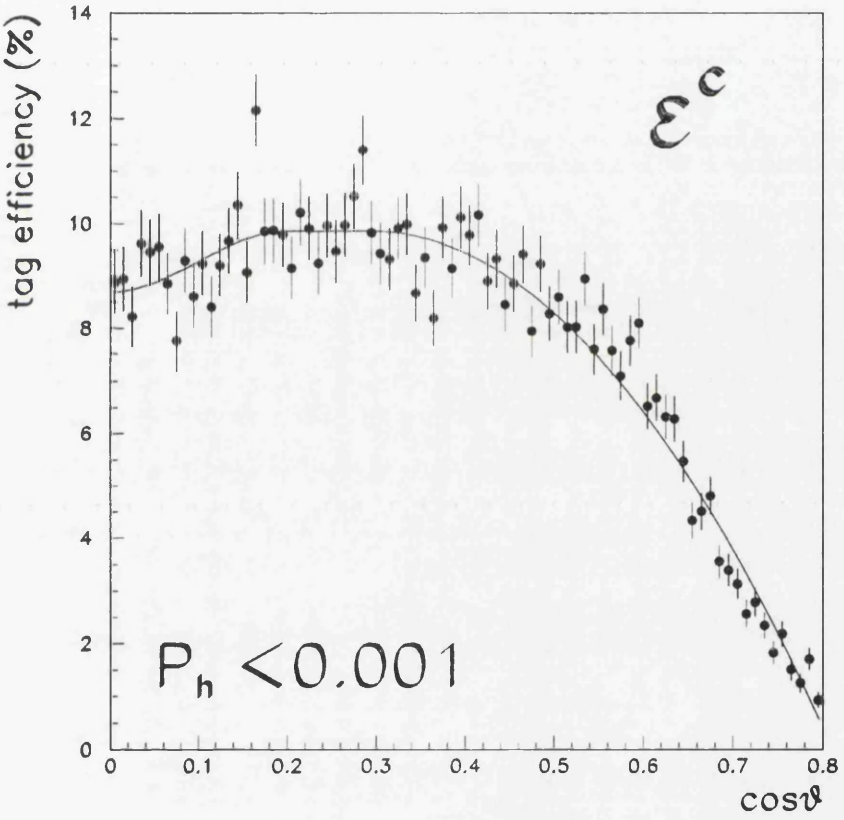

Figure 4.10: *The $c\bar{c}$ event tagging efficiency ε^c as a function of the $cos\theta$, with the central region ($cos\theta \sim 0$) modelled with a cubic dependence. The resulting decrease in the acceptance factor C^c compared to a flat $cos\theta$ dependence in the central region is less than* 0.1%.

Near the centre of VDET there is a ring, 50μm wide, for which there is no charged particle detection. The effect of this hole on the efficiencies is evident, if at all, only in the c efficiency, ε^c, as shown in figure 4.10 (linear scale). By modelling this region with a cubic $cos\theta$ dependence the acceptance factors were recalculated. The resulting decrease in C^c is less than 0.1%, so the effect can safely be ignored.

4.4 Summary

The impact parameter tag, used to select $b\bar{b}$ decays of the Z^0, has been described in detail. The event tagging efficiencies and purities have been measured and are presented in table 4.4. The angular dependence of the tag's performance was studied and the flavour dependent acceptance factors, defined in equation (4.12), were evaluated. These are shown in table 4.7. Both these quantities are required for the interpretation of the measured charge asymmetry, $\langle Q_{FB} \rangle$, in terms of the underlying $b\bar{b}$ forward-backward asymmetry, $\mathcal{A}_{FB}^{b\bar{b}}$, according to equation (3.7) of chapter 3.

Chapter 5

Quark charge separations

In this chapter the quark charge separations, δ^f, introduced in chapter 3, are evaluated. Section 5.1 describes the evaluation of the charge separations using Monte Carlo simulation and their systematic errors due to uncertainties in the fragmentation process are determined. In section 5.2 a measurement of the b charge separation is presented. The method used is insensitive to Monte Carlo simulation of b quark production and b hadron production and decay.

5.1 Monte Carlo quark charge separations

This section describes the evaluation of the charge separations using Monte Carlo simulation. Monte Carlo events are selected using the standard ALEPH hadronic event selection discussed in chapter 6 and are required to have their thrust axis within the VDET polar angle acceptance, $|cos\theta| < 0.8$. This selection has an efficiency of about 74%, leaving ~240,000 u and c events and ~310,000 d, s and b events.

For the hemisphere charge calculations charged tracks with momentum transverse to the incident beam direction less than 200 MeV/c are not used (see chapter 6).

5.1.1 κ dependence

Figure 5.1 shows the forward-backward hemisphere charge difference distribution in $u\bar{u}$ events for four different κ values (see equation 3.1). For small κ, approximately equal

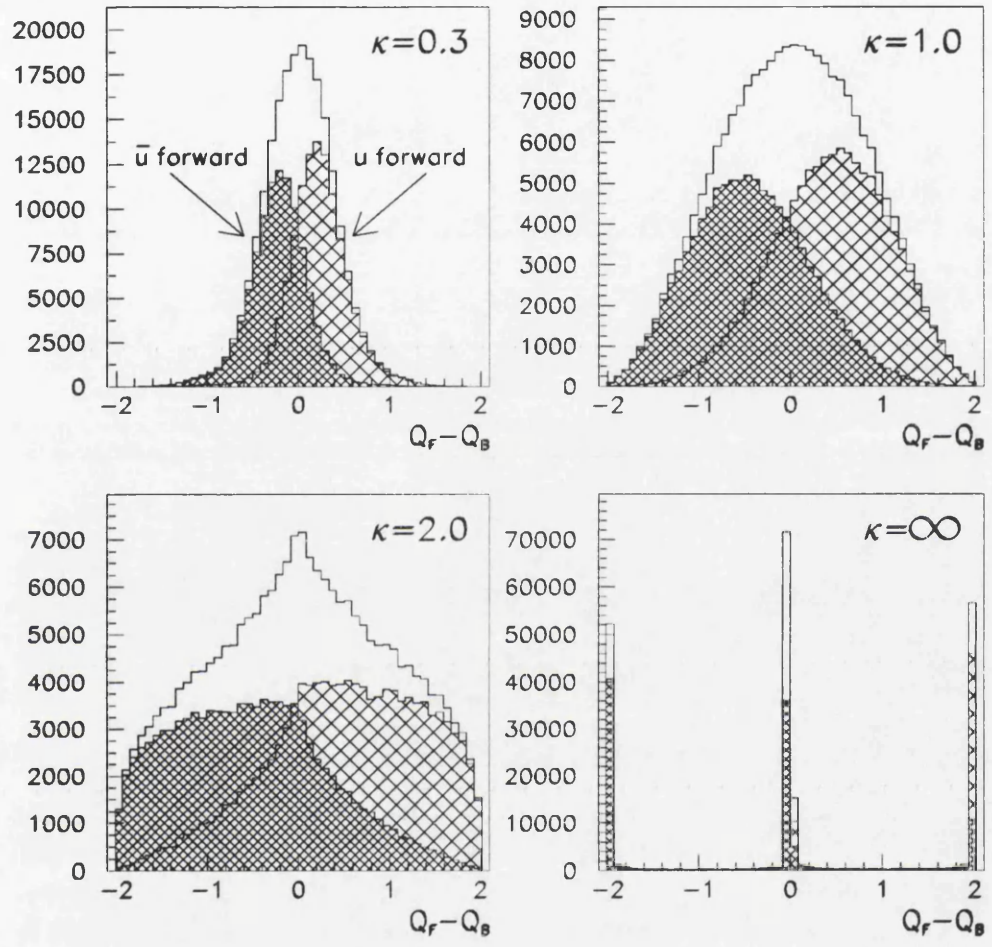

Figure 5.1: *The forward-backward hemisphere charge difference distribution in $u\bar{u}$ events for four different κ values.*

emphasis is placed on each track in the hemisphere charge calculation. As κ increases more emphasis is put on the leading tracks in the hemisphere, causing the mean charge separations to increase in magnitude, but their widths also increase. Figure 5.2 shows

the κ dependence of the charge separation significance, $\mathcal{S}^f$, defined as

$$\mathcal{S}^f = \frac{\delta^f}{\sigma(\delta^f)}\,, \tag{5.1}$$

where $\sigma(\delta^f)$ is the width of the charge separation distribution. It is clear that the most significant b charge separation, for instance, is obtained for $\kappa \sim 0.5$.

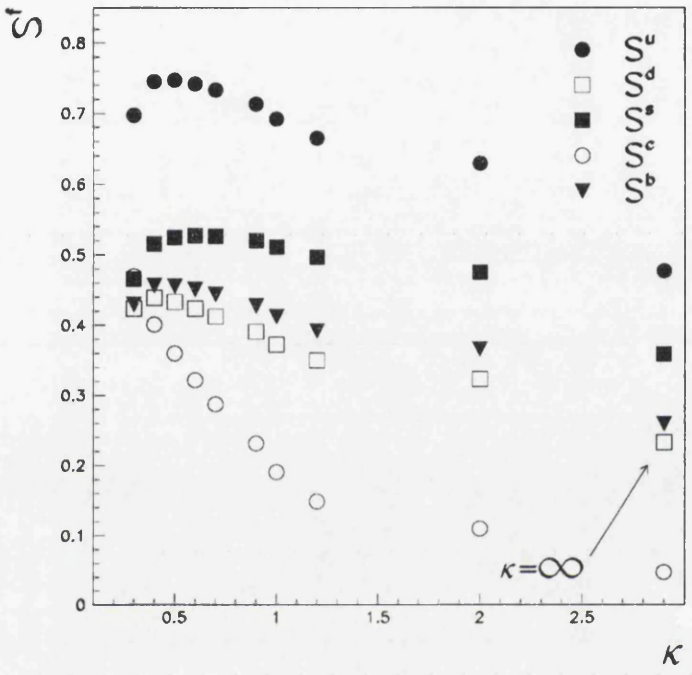

Figure 5.2: *The quark charge separation significance $\mathcal{S}^f$ as a function of κ.*

In figure 5.3 the κ dependence of all five quark charge separations are shown. As one might expect the charge $\frac{1}{3}$ quarks (d, s, b) have similar charge separations and are smaller than that of the u quark (charge $\frac{2}{3}$). However the c charge separation is much smaller than that of the u and decreases with increasing κ. This is because when a charged D^* meson, containing one of the original c quarks, decays to a D meson and a soft pion, the pion carries the c quark charge with it. As a result the c quark charge has little influence on the hemisphere charge, especially for large κ when only the highest momentum tracks contribute.

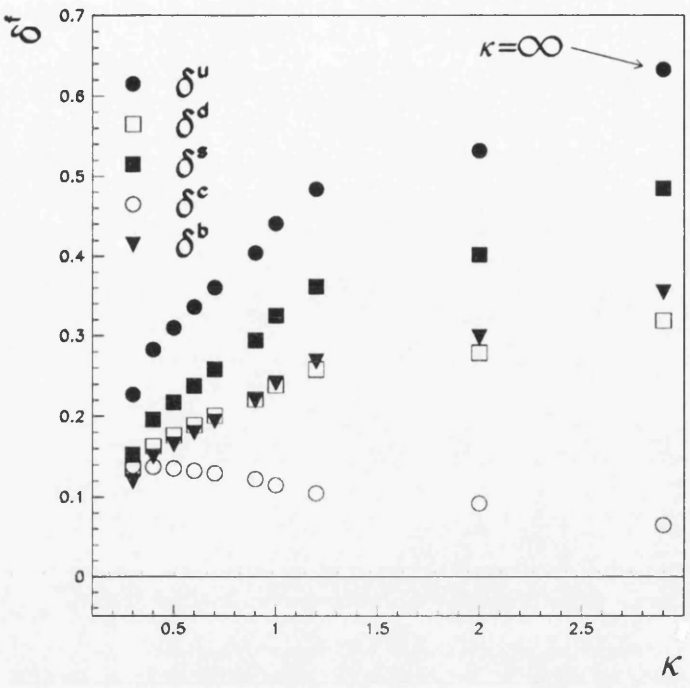

Figure 5.3: *The κ dependence of the quark charge separations. The d, s and b charge separations are in fact negative, but for easy comparison of their magnitudes the absolute values are shown.*

5.1.2 Impact parameter tag cut dependence

The impact parameter tag selects events with visible lifetime in the form of charged tracks with large impact parameters. The significance of the impact parameters are intrinsically dependent on momentum. Consequently, the tag introduces a bias in the charged multiplicity and mean momentum of tracks within hadronic events, preferring a large track multiplicity and a lower average momentum. This has the effect of decreasing the quark charge retention properties of event hemispheres and hence the quark charge separations. This effect is shown in figure 5.4 for the u, d, s and c charge separations. The effect is worse for the s and c separations since a large fraction of $s\bar{s}$ and $c\bar{c}$ events have visible lifetime and are therefore more likely to be affected by the bias introduced by the tag. Any visible lifetime within $u\bar{u}$ and $d\bar{d}$ events is spread

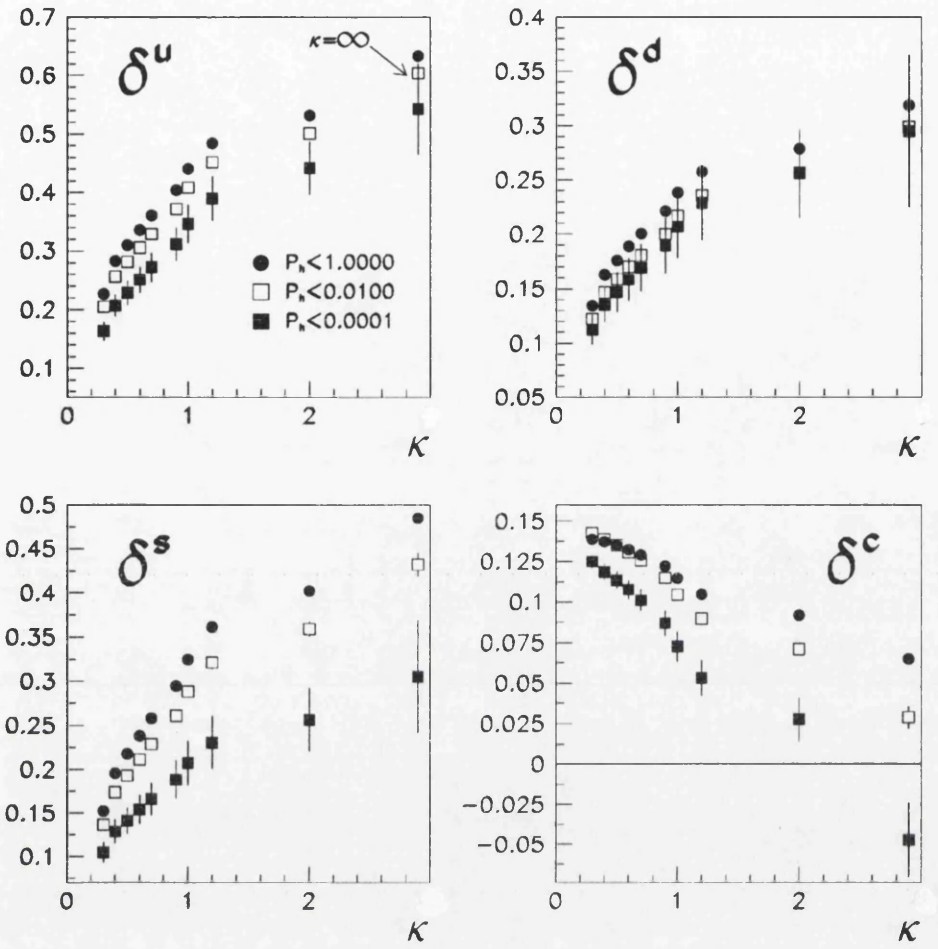

Figure 5.4: *The effect of the impact parameter tag on the quark charge separations.* $P_h < 1.0$ *is equivalent to NO tag.*

more evenly throughout the events since this lifetime is due largely to the finite impact parameter resolution

5.1.3 Fragmentation systematic errors

The charge separations depend on the fragmentation parameters used in the Monte Carlo simulation. By varying the relevant parameters in JETSET 7.3 within their experimental or theoretical limits systematic errors on the separations are determined.

The fragmentation parameters and their ranges are shown in table 5.1.

fragmentation Parameter	*Default value*	*lower limit*	*upper limit*
Λ_{QCD}	0.311	0.286	0.336
M_{min}	1.900	1.740	2.060
σ	0.347	0.336	0.358
ϵ_b	0.006	0.0043	0.0055
$V/(V+PS)_{u,d}$	0.500	0.300	0.750
$V/(V+PS)_s$	0.600	0.500	0.750
$V/(V+PS)_{c,b}$	0.750	0.434	0.630
$\frac{s}{u}$	0.300	0.270	0.330
χ_d	0.164	0.118	0.180
χ_s	0.250	0.250	0.499
Baryon Fraction	0.100	0.080	0.120
Popcorn Parameter	0.500	0.000	2.000

Table 5.1: *The fragmentation parameters and their current ranges.*

In practice the systematic errors on the charge separations are evaluated as in the following example for the u charge separation and the parameter Λ_{QCD}. Samples of $u\bar{u}$ events are generated with different values of Λ_{QCD}. For computational expediency the simulation of detector effects is not included. The u separations are then evaluated within each event sample. Figure 5.5 shows the percentage change in δ^u from its default value for each Λ_{QCD} value. The maximum possible gradient consistent with the five points is estimated and used to make a conservative estimate of the percentage change in δ^u due to the variation of Λ_{QCD}. The change is then scaled to the u separation evaluated including the simulation of detector effects.

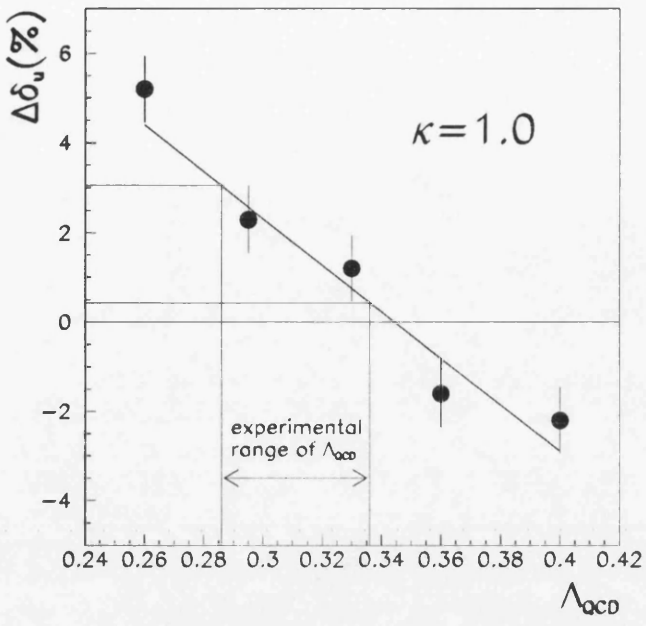

Figure 5.5: Λ_{QCD} *dependence of the* u *charge separation* δ^u *for* $\kappa = 1.0$.

The total theoretical systematic errors on the δ^f are obtained by adding in quadrature the errors from the variation of each of the fragmentation parameters and are shown in table 5.2 for u, d, s and c events passing a tag cut of $P_h < 0.001$. Also shown for comparison are the Monte Carlo statistical errors.

5.2 A measurement of the b charge separation using the impact parameter tag

The systematic error on the Monte Carlo predicted b charge separation δ^b due to uncertainties in b quark fragmentation and b hadron production and decay properties is $\sim 14\%$. For this reason and the fact that the asymmetry measurement is very sensitive to any uncertainty in δ^b, it is desirable that the b charge separation be measured in real data. This section describes a measurement of δ^b in the 1992 data sample using

	δ^f $\pm(stat) \pm (syst)$			
κ	u	d	s	c
0.3	0.1985	0.1064	0.1236	0.1376
	$\pm$ 0.0079 $\pm$ 0.0141	$\pm$ 0.0066 $\pm$ 0.0152	$\pm$ 0.0063 $\pm$ 0.0116	$\pm$ 0.0021 $\pm$ 0.0178
0.4	0.2215	0.1158	0.1399	0.1345
	$\pm$ 0.0087 $\pm$ 0.0157	$\pm$ 0.0071 $\pm$ 0.0166	$\pm$ 0.0067 $\pm$ 0.0131	$\pm$ 0.0023 $\pm$ 0.0175
0.5	0.2448	0.1254	0.1566	0.1303
	$\pm$ 0.0096 $\pm$ 0.0173	$\pm$ 0.0078 $\pm$ 0.0179	$\pm$ 0.0074 $\pm$ 0.0147	$\pm$ 0.0025 $\pm$ 0.0169
0.7	0.2901	0.1445	0.1897	0.1193
	$\pm$ 0.0118 $\pm$ 0.0205	$\pm$ 0.0095 $\pm$ 0.0207	$\pm$ 0.0091 $\pm$ 0.0178	$\pm$ 0.0031 $\pm$ 0.0155
0.9	0.3313	0.1621	0.2199	0.1065
	$\pm$ 0.0142 $\pm$ 0.0235	$\pm$ 0.0115 $\pm$ 0.0232	$\pm$ 0.0109 $\pm$ 0.0206	$\pm$ 0.0037 $\pm$ 0.0138
1.0	0.3499	0.1700	0.2335	0.0999
	$\pm$ 0.0153 $\pm$ 0.0248	$\pm$ 0.0125 $\pm$ 0.0243	$\pm$ 0.0118 $\pm$ 0.0219	$\pm$ 0.0041 $\pm$ 0.0130
1.2	0.3827	0.1841	0.2572	0.0872
	$\pm$ 0.0174 $\pm$ 0.0271	$\pm$ 0.0144 $\pm$ 0.0263	$\pm$ 0.0135 $\pm$ 0.0241	$\pm$ 0.0047 $\pm$ 0.0113
1.5	0.4215	0.2009	0.2850	0.0704
	$\pm$ 0.0202 $\pm$ 0.0299	$\pm$ 0.0169 $\pm$ 0.0287	$\pm$ 0.0157 $\pm$ 0.0267	$\pm$ 0.0056 $\pm$ 0.0091
2.0	0.4645	0.2205	0.3149	0.0498
	$\pm$ 0.0237 $\pm$ 0.0329	$\pm$ 0.0202 $\pm$ 0.0315	$\pm$ 0.0186 $\pm$ 0.0295	$\pm$ 0.0067 $\pm$ 0.0065
∞	0.5565	0.2636	0.3793	0.0041
	$\pm$ 0.0383 $\pm$ 0.0394	$\pm$ 0.0344 $\pm$ 0.0377	$\pm$ 0.0314 $\pm$ 0.0355	$\pm$ 0.0116 $\pm$ 0.0005

Table 5.2: *The u, d, s and c charge separations and their statistical and systematic errors in events passing a tag cut of $P_h < 0.001$.*

the impact parameter tag [28] [29]. In the following subsection a brief outline of the method is given, section 5.2.2 presents the experimental results and in section 5.2.3 the b charge separation is determined.

5.2.1 Principle of the measurement

For each hadronic event the forward-backward hemisphere charge difference Q_{FB} and charge sum Q are given by

$$Q_{FB} = Q_F - Q_B \,,$$

$$Q = Q_F + Q_B \,, \tag{5.2}$$

$$\tag{5.3}$$

where the forward and backward hemisphere charges are calculated as in chapter 3.1. Schematic Q_{FB} and Q distributions are shown in figure 5.6 for $b\bar{b}$ events. It is possible to evaluate the b charge separation, δ^b, by exploiting the difference between the widths σ_{FB} and σ_Q of the Q_{FB} and Q distributions respectively.

The quantity $\bar{\delta}$ defined as

$$\bar{\delta}^2 = \sigma_{FB}^2 - \sigma_Q^2 \tag{5.4}$$

is measured in data samples of varying b purity. By fitting the purity dependence of $\bar{\delta}$ and extrapolating to 100% b purity $\bar{\delta}^b$ is obtained :

$$(\bar{\delta}^b)^2 = (\sigma_{FB}^{b\bar{b}})^2 - (\sigma_Q^{b\bar{b}})^2 \tag{5.5}$$

which can be expressed in terms of δ^b as follows

$$(\bar{\delta}^b)^2 = (\delta^b)^2 + \langle Q_{FB}^{b\bar{b}} \rangle^2 + 4\,(\langle Q_F Q_B \rangle - \langle Q_F \rangle \langle Q_B \rangle) \,. \tag{5.6}$$

The derivation of this relation is given in [28]. The term $4\,(\langle Q_F Q_B \rangle - \langle Q_F \rangle \langle Q_B \rangle)$ is the correlation between the forward and backward hemisphere charges and is evaluated

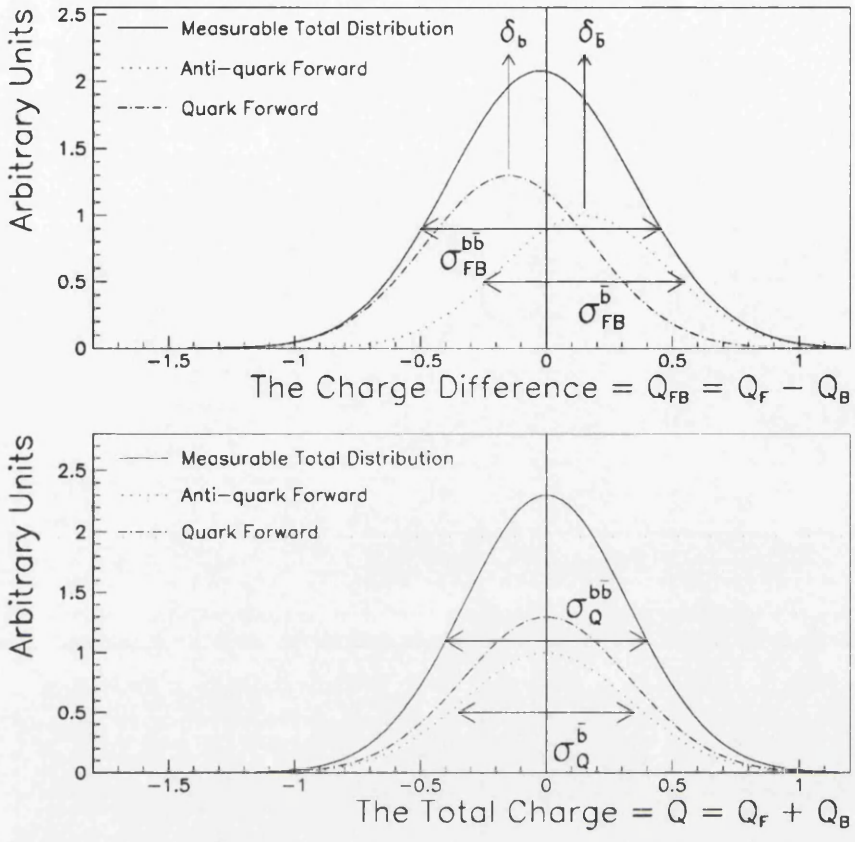

Figure 5.6: *Schematic Q_{FB} and Q distributions in $b\bar{b}$ events.*

using Monte Carlo simulation. $\langle Q^{b\bar{b}}_{FB} \rangle$ is the forward-backward charge asymmetry in $b\bar{b}$ events and is estimated using the charge asymmetry measured in data with a b purity of $\sim 95\%$. $(\langle Q_F Q_B \rangle - \langle Q_F \rangle \langle Q_B \rangle)$ and $\langle Q^{b\bar{b}}_{FB} \rangle$ are small and enter equation 5.6 only as corrections. (For zero asymmetry and no hemisphere charge correlations $\bar{\delta}^b = \delta^b$.)

5.2.2 Experimental results

Events are selected using the standard ALEPH hadronic event selection described in chapter 6 and the thrust axis is required to lie within the VDET approximate polar angle acceptance, $|cos\theta| < 0.8$. The raw $\bar{\delta}$ values are evaluated using equation 5.4 and are shown in figure 5.7 for a range of κ values. Before these values can be used in an

extrapolation to 100% b purity they have to be corrected for any bias introduced by the impact parameter tag.

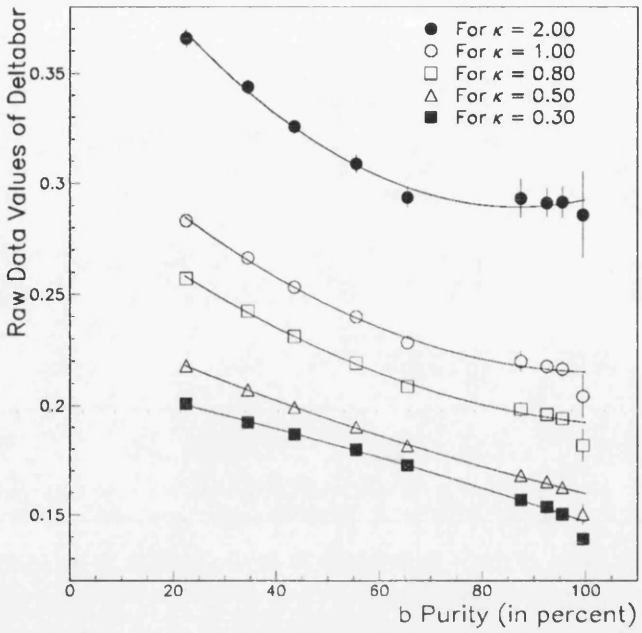

Figure 5.7: *The variation of the raw $\bar{\delta}$ values in data as a function the b purity of the event subsample.*

The tag algorithm selects events with visible lifetime in the form of charged tracks with large impact parameters. The significance of the impact parameters depends on the track momentum. Consequently the tag introduces a bias in the number of charged tracks and in their momentum. This in turn introduces a bias in the mean hemisphere charges and their widths. Given that the effects are small, and well modelled by the Monte Carlo, the lifetime dependence of the simulated $\bar{\delta}^f$s are used to correct the raw $\bar{\delta}$ data values. The corrections are calculated using

$$\begin{aligned} Correction &= \bar{\delta}^{MC}_{tagged} - \bar{\delta}^{MC}_{untagged}, \\ &= \sqrt{\sum_{f=u,d...}^{b} \mathcal{P}^f (\bar{\delta}^f)^2_{tagged}} - \sqrt{\sum_{f=u,d...}^{b} \mathcal{P}^f (\bar{\delta}^f)^2_{untagged}}, \end{aligned} \tag{5.7}$$

where $\mathcal{P}^f$ are the quark purities. These corrections are assigned systematic errors to account for an observed difference between the ratio of tagged and untagged hemisphere charge widths in data and Monte Carlo. When added to the Monte Carlo statistical error on the corrections this represents an additional 20% uncertainty. The corrected $\bar{\delta}$ values are shown in figure 5.8.

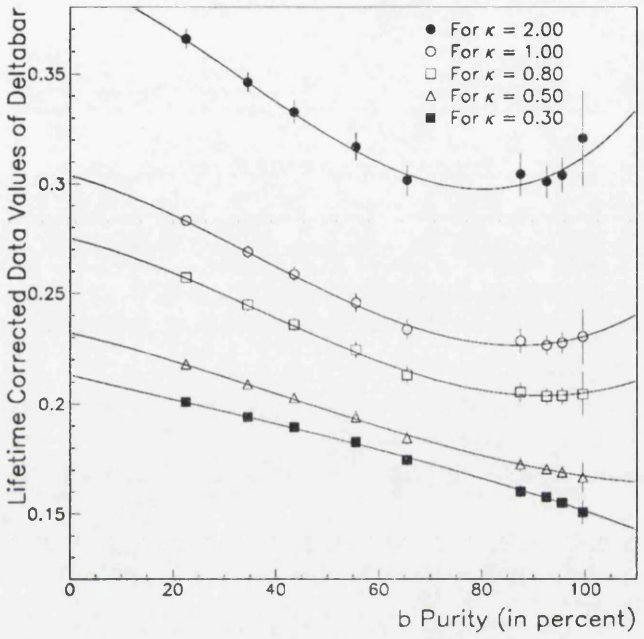

Figure 5.8: *The variation of the lifetime-corrected $\bar{\delta}$ values in data as a function the b purity.*

The trends displayed in figure 5.8 can be explained by writing $\bar{\delta}$ as

$$\bar{\delta} = \sqrt{\sum_{f=u,d...}^{b} P^f \, (\bar{\delta}^f)^2} \tag{5.8}$$

Before applying the impact parameter tag the quark purities are all $\sim 20\%$ and $\bar{\delta}$ is dominated by $\bar{\delta^u}$, it being the largest. When the b purity rises to $\sim 80\%$ the light quark purities drop effectively to zero and the only background is from $c\bar{c}$ events. For small κ values $|\bar{\delta^c}| > |\bar{\delta^b}|$ so as the b purity increases further, $\bar{\delta}$ continues to decrease toward

$\bar{\delta}^b$. However, for large κ, $|\bar{\delta}^c| < |\bar{\delta}^b|$ causing $\bar{\delta}$ to reach a minimum and then increase with b purity as the c contamination diminishes.

κ	$\bar{\delta}^b$	$\langle Q_{FB}^{b\bar{b}} \rangle$	$4\,(\langle Q_F Q_B \rangle - \langle Q_F \rangle \langle Q_B \rangle)$
0.3	0.1513 ± 0.0028	0.0093 ± 0.0011	0.0108 ± 0.0003
0.4	0.1577 ± 0.0030	0.0106 ± 0.0013	0.0092 ± 0.0004
0.5	0.1627 ± 0.0034	0.0119 ± 0.0014	0.0082 ± 0.0004
0.6	0.1791 ± 0.0038	0.0131 ± 0.0016	0.0076 ± 0.0006
0.8	0.2050 ± 0.0047	0.0152 ± 0.0020	0.0076 ± 0.0009
0.9	0.2178 ± 0.0051	0.0161 ± 0.0021	0.0079 ± 0.0010
1.0	0.2307 ± 0.0056	0.0170 ± 0.0023	0.0084 ± 0.0012
1.5	0.2813 ± 0.0076	0.0200 ± 0.0032	0.0112 ± 0.0023
2.0	0.3127 ± 0.0093	0.0216 ± 0.0038	0.0136 ± 0.0032
∞	0.3378 ± 0.0222	0.0220 ± 0.0065	0.0176 ± 0.0099

Table 5.3: *The corrected $\bar{\delta}^b$ values obtained by extrapolating the fits of figure 5.8, the $\langle Q_{FB} \rangle$ values measured in a 95% b purity data sample and the hemisphere charge correlations evaluated using Monte Carlo simulation.*

The corrected $\bar{\delta}$ distributions are fitted with cubic polynomials reflecting the three regimes in its dependence on the b purity. The fits are superimposed in figure 5.8 and are used to extrapolate to 100% b purity. The resulting $\bar{\delta}^b$ values are shown in column 1 of table 5.3.

The unbiased $b\bar{b}$ forward-backward charge asymmetry $\langle Q_{FB}^{b\bar{b}} \rangle$ values are estimated using the charge asymmetries measured in a data sample with a b purity of $\sim 95\%$ and are shown in column 2 of table 5.3. The errors shown are the statistical errors only ;

the systematic errors are negligible. Also shown are the hemisphere charge correlations evaluated using Monte Carlo simulation and their Monte Carlo statistical errors.

5.2.3 Determination of the b charge separation

Equation 5.6 is used to determine δ^b from the corrected $\bar{\delta}^b$ values given in table 5.3.

Model parameter	*Parameter range*		Δ *Correlation and error*	
Λ_{QCD}	0.296	0.346	0.0001	0.0002
M_{min}	1.530	1.770	0.0004	0.0001
σ	0.342	0.352	0.0001	0.0001
ϵ_b	0.002	0.007	0.0001	0.0003
$V/(V+PS)_{u,d}$	0.520	0.580	0.0001	0.0001
$V/(V+PS)_{s}$	0.570	0.630	0.0001	0.0001
$V/(V+PS)_{c,b}$	0.510	0.690	0.0002	0.0002
$\frac{s}{u}$	0.291	0.311	0.0001	0.0001
χ_d	0.118	0.180	0.0004	0.0006
χ_s	0.250	0.499	0.0000	0.0010
Baryon Fraction	0.099	0.110	0.0003	0.0002
Popcorn Parameter	0.350	0.550	0.0000	0.0001

Table 5.4: *The effect of varying different fragmentation model parameters on the correlation corrections for $\kappa = 0.5$.*

Systematic errors on the hemisphere charge correlations due to uncertainties in b fragmentation and b hadron production and decay, are evaluated by varying those parameters within JETSET 7.3 relevant to the b system within their experimental or theoretical limits [29]. These errors are summarised in table 5.4 for the case $\kappa = 0.5$. A

κ	$\delta^b \pm (stat) \pm (syst)$
0.3	$0.1100 \pm 0.0026 \pm 0.0040$
0.4	$0.1252 \pm 0.0027 \pm 0.0041$
0.5	$0.1400 \pm 0.0029 \pm 0.0039$
0.6	$0.1688 \pm 0.0036 \pm 0.0048$
0.8	$0.1952 \pm 0.0045 \pm 0.0063$
0.9	$0.2068 \pm 0.0049 \pm 0.0067$
1.0	$0.2272 \pm 0.0058 \pm 0.0075$
1.5	$0.2515 \pm 0.0077 \pm 0.0082$
2.0	$0.2777 \pm 0.0088 \pm 0.0154$
∞	$0.2848 \pm 0.0239 \pm 0.0229$

Table 5.5: *Final δ^b values and their statistical and systematic errors.*

summary of the final δ^b values and their statistical and total systematic errors is given in table 5.5. These δ^b values are used in the asymmetry analysis.

The self-consistency of the method was tested on Monte Carlo simulated data by comparing the extracted δ^b with their true values. The results are shown in table 5.6. The systematic errors on the extracted δ_b values include only those effects not derived from the same Monte Carlo sample. From the values shown it is clear that the method is self-consistent.

5.3 Summary

A detailed description of the evaluation of the quark charge separations, δ^f, defined in chapter 3, has been presented. The u, d, s and c charge separations were estimated using Monte Carlo simulated data and are shown in table 5.2 for events passing a tag cut of $P_h < 0.001$. A method for measuring the b charge separation using the lifetime

κ	Monte Carlo measured δ^b	Monte Carlo true δ^b
0.3	0.1215 ± 0.0038	0.1210 ± 0.0006
0.4	0.1364 ± 0.0038	0.1357 ± 0.0006
0.5	0.1513 ± 0.0040	0.1505 ± 0.0007
0.6	0.1813 ± 0.0046	0.1793 ± 0.0008
0.8	0.2087 ± 0.0054	0.2057 ± 0.0010
0.9	0.2207 ± 0.0058	0.2177 ± 0.0011
1.0	0.2430 ± 0.0065	0.2393 ± 0.0013
1.5	0.2694 ± 0.0074	0.2651 ± 0.0015
2.0	0.1983 ± 0.0085	0.2942 ± 0.0018
∞	0.3554 ± 0.0156	0.3483 ± 0.0031

Table 5.6: *The δ^b values obtained using the method described in section 5.2.1 on Monte Carlo data, and those extracted directly from the Monte Carlo. The agreement between the two sets of values proves the self consistency of the method*

tag was described and the results obtained are presented in table 5.5. The quark charge separations are one of the key elements required for the electroweak interpretation of the measured charge asymmetry, $\langle Q_{FB} \rangle$.

Chapter 6

A measurement of the forward-backward charge asymmetry

A measurement of the charge asymetry in a $Z^0 \rightarrow b\bar{b}$ event sample is used to extract the underlying forward-backward asymmetry $\mathcal{A}_{FB}^{b\bar{b}}$. The momentum weighted charge method, introduced in chapter 3, is used in other ALEPH analyses [18] [19]. In particular, it was first used to measure the charge asymmetry in an inclusive sample of hadronic events where the fractions of u and d type quarks present are given simply by their corresponding Z^0 branching fractions. As a result, the measured charge asymmetry has approximately equal contributions from u and d type quarks which have opposite signed charge asymmetries and so lead to some degree of cancellation, which decreases the sensitivity of the measurement to the underlying quark asymmetries. The analysis is also inherently dependent on Monte Carlo simulation of the quark fragmentation process.

By measuring the charge asymmetry in a sample enhanced in one quark flavour the cancellation is reduced and the measurement's sensitivity to the underlying asymmetry

increases. In this analysis track impact parameters are used to obtain a high purity $b\bar{b}$ event sample. Consequently, the measured charge asymmetry is sensitive to the $b\bar{b}$ asymmetry $\mathcal{A}_{FB}^{b\bar{b}}$, but not to the lighter quark asymmetries. Furthermore, as described in chapter 5, it is possible to measure the mean hemisphere charge of the b quark in data. This is one of the key elements in the interpretation of the measured charge asymmetry and effectively removes any dependence on Monte Carlo simulation of quark fragmentation.

Section 6.1 discusses in detail the event and track selections. Section 6.2 presents the measured $\langle Q_{FB} \rangle$ values and finally in section 6.3 the experimental systematic errors on $\langle Q_{FB} \rangle$ are determined.

6.1 Event Selection

Events are selected according to the standard ALEPH hadronic event selection. This selection, based on charged tracks, requires at least five charged tracks in the TPC. The sum of the energies of the tracks (assuming the pion mass) is required to be larger than 10% of the centre of mass energy. The tracks must have a polar angle greater than 18.2° ($|cos\theta| < 0.95$), which ensures that at least 6 TPC pad rows are traversed, and must have at least four reconstructed coordinates. The distance of closest approach of the tracks to the ALEPH origin must be less than 10 cm along the beam direction and 2 cm transverse to it.

This selection has an efficiency of $\sim 99\%$ and introduces no significant flavour bias. The background from τ events and two photon interactions is ~ 0.62 and $\sim 0.3\%$ respectively [30]. The latter have negligible lifetime and are effectively removed after applying typical impact parameter tag cuts. The τ has a significant lifetime but its decay products have small impact parameters owing to the small τ mass. Consequently, τ events too form a negligible background ($\sim 0.05\%$) once typical tag cuts are applied.

In addition to the hadronic event selection, the event thrust axes, reconstructed using all charged and neutral objects[1], must lie within the approximate polar angle acceptance of the VDET $|cos\theta| < 0.8$. These cuts give an overall acceptance of 75.2% leaving 504,911 hadronic events from an initial sample of 671,362 events.

The surviving events are then passed through the impact parameter tag which has its own event selection. Table 6.1 shows the effect of each stage of the event selection, and the nominal b purities corresponding to each tag cut.

Selection	*Number of events*	
Hadronic event selection	671362	
$\|cos\theta\| < 0.8$	504911	
$P_h < 0.01$	112811	$\mathcal{P}^b = 73\%$
$P_h < 0.005$	96806	$\mathcal{P}^b = 79\%$
$P_h < 0.001$	70259	$\mathcal{P}^b = 88\%$
$P_h < 0.0005$	61882	$\mathcal{P}^b = 91\%$
$P_h < 0.0001$	45992	$\mathcal{P}^b = 95\%$

Table 6.1: *The data sample sizes for each cut on the impact parameter tag. The nominal b purities corresponding to each tag cut are also shown.*

6.2 The measured forward-backward charge asymmetry

The forward-backward hemisphere charge asymmetry $\langle Q_{FB} \rangle$ is measured in the event samples shown in table 6.1. In the hemisphere charge calculations those tracks with momentum transverse to the beam direction less than 200 MeV/c are not used. This removes tracking ambiguities introduced by the spiralling of such tracks in the TPC.

[1] The reconstruction of the four-momenta of all the charged and neutral particles is described in [21]

Before evaluating the hemisphere charges each charged track is corrected for an observed momentum imbalance as described later in section 6.3.1.

	$\langle Q_{FB} \rangle \pm (stat)$				
κ	$P_h < 0.0100$	$P_h < 0.0050$	$P_h < 0.0010$	$P_h < 0.0005$	$P_h < 0.0001$
0.3	-0.0061 ± .0008	-0.0073 ± .0009	-0.0088 ± .0010	-0.0089 ± .0011	-0.0098 ± .0012
0.4	-0.0070 ± .0009	-0.0082 ± .0010	-0.0100 ± .0011	-0.0101 ± .0012	-0.0111 ± .0013
0.5	-0.0079 ± .0010	-0.0092 ± .0011	-0.0112 ± .0012	-0.0112 ± .0013	-0.0124 ± .0015
0.7	-0.0096 ± .0012	-0.0111 ± .0013	-0.0135 ± .0015	-0.0133 ± .0016	-0.0147 ± .0018
0.9	-0.0112 ± .0015	-0.0128 ± .0016	-0.0154 ± .0018	-0.0151 ± .0019	-0.0167 ± .0022
1.0	-0.0119 ± .0016	-0.0135 ± .0017	-0.0163 ± .0020	-0.0159 ± .0021	-0.0176 ± .0024
1.2	-0.0131 ± .0018	-0.0149 ± .0019	-0.0179 ± .0022	-0.0173 ± .0024	-0.0190 ± .0027
1.5	-0.0147 ± .0021	-0.0166 ± .0023	-0.0198 ± .0026	-0.0188 ± .0028	-0.0207 ± .0032
2.0	-0.0164 ± .0025	-0.0185 ± .0027	-0.0218 ± .0031	-0.0204 ± .0033	-0.0223 ± .0038
∞	-0.0159 ± .0042	-0.0196 ± .0045	-0.0233 ± .0053	-0.0208 ± .0056	-0.0233 ± .0065

Table 6.2: *The measured $\langle Q_{FB} \rangle$ values for the full range of κ and P_h cut values.*

The measured $\langle Q_{FB} \rangle$ values and their statistical errors are shown in table 6.2. Figures 6.1.a and b. demonstrate the dependence of $\langle Q_{FB} \rangle$ and its statistical significance, $\langle Q_{FB} \rangle / \sigma_{FB}$, on the tag cut, P_h, for $\kappa = 0.5$. A maximum statistical significance of 9.25 is obtained for a tag cut of $P_h < 0.001$, corresponding to a b purity of $\sim 88\%$. As the background diminishes, $\langle Q_{FB} \rangle$ approaches its asymptotic value $\langle Q_{FB}^{b\bar{b}} \rangle$ but its statistical error increases due to the decreasing statistics. For a cut of $P_h < 0.001$ a compromise is reached between the increasing b purity and the decreasing sample size. Figures 6.1.c. and d. show the κ dependence using the above tag cut. The optimal κ of 0.5 corresponds to that which gave the most significant b charge separation, δ^b, as shown in figure 5.2 of chapter 5.

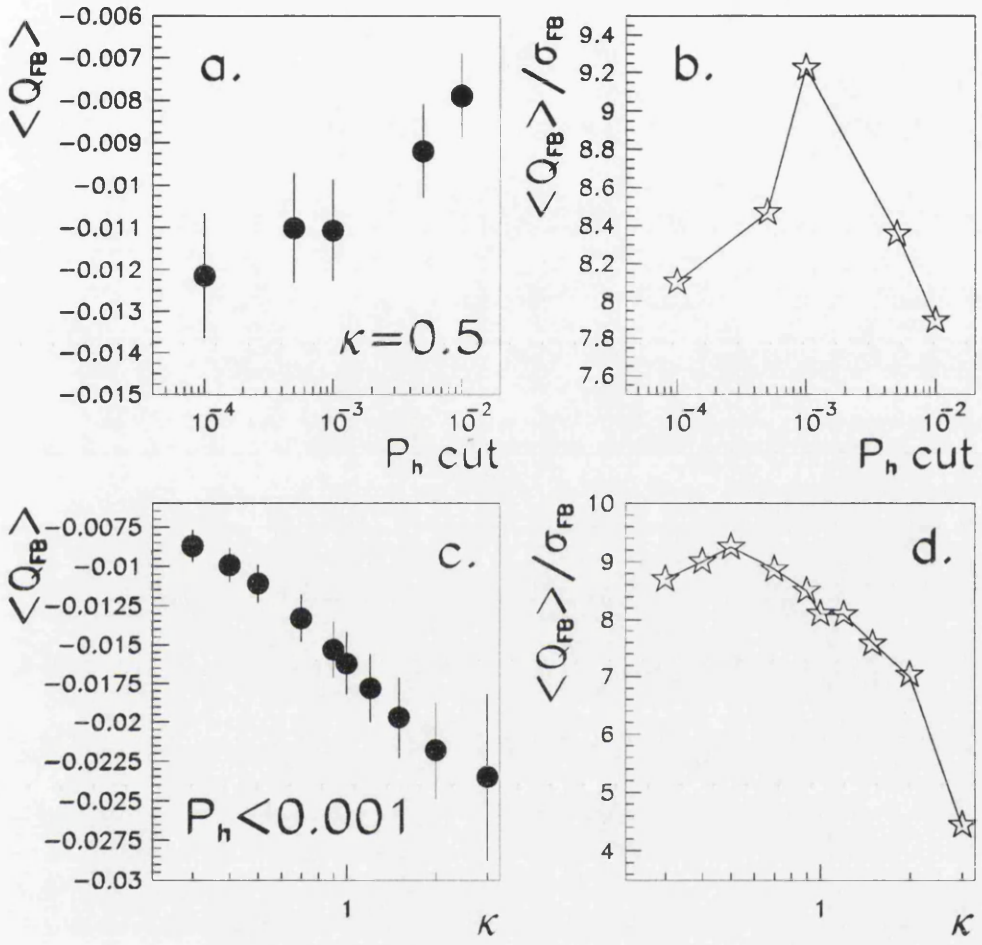

Figure 6.1: *Figures (a) and (b) show* $\langle Q_{FB} \rangle$ *and its statistical significance* $\langle Q_{FB} \rangle / \sigma_{FB}$ *as a function of the tag cut* P_h. *Figures (c) and (d) show the corresponding distributions as a function a* κ. *The optimal* P_h *cut and* κ *values are 0.001 and 0.5 respectively.*

κ	$\langle Q \rangle \pm (stat)$				
	$P_h < 0.0100$	$P_h < 0.0050$	$P_h < 0.0010$	$P_h < 0.0005$	$P_h < 0.0001$
0.3	0.0065 ± .0007	0.0061 ± .0007	0.0051 ± .0008	0.0046 ± .0009	0.0043 ± .0010
0.4	0.0063 ± .0008	0.0059 ± .0008	0.0049 ± .0009	0.0043 ± .0010	0.0040 ± .0011
0.5	0.0062 ± .0009	0.0056 ± .0009	0.0046 ± .0011	0.0040 ± .0011	0.0037 ± .0013
0.7	0.0058 ± .0011	0.0052 ± .0012	0.0041 ± .0013	0.0034 ± .0014	0.0029 ± .0016
0.9	0.0055 ± .0013	0.0048 ± .0014	0.0036 ± .0016	0.0028 ± .0017	0.0022 ± .0020
1.0	0.0054 ± .0014	0.0046 ± .0015	0.0033 ± .0018	0.0025 ± .0019	0.0018 ± .0022
1.2	0.0051 ± .0017	0.0042 ± .0018	0.0028 ± .0021	0.0019 ± .0022	0.0010 ± .0025
1.5	0.0046 ± .0020	0.0035 ± .0021	0.0010 ± .0024	0.0010 ± .0026	-0.0001 ± .0030
2.0	0.0038 ± .0024	0.0026 ± .0025	0.0009 ± .0029	-0.0004 ± .0031	-0.0017 ± .0036
∞	0.0012 ± .0041	-0.0001 ± .0044	-0.0024 ± .0052	-0.0040 ± .0055	-0.0054 ± .0064

Table 6.3: *The measured $\langle Q \rangle$ values for the full range of κ and P_h cut values.*

The $\langle Q \rangle$ ($= \langle Q_F + Q_B \rangle$) values and their statistical errors are shown in table 6.3. The $\langle Q \rangle$ values are incompatible with zero for low κ due to the interaction of soft particles in the detector material between the Z^0 decay point and the inner wall of the TPC, which is charge asymmetric due to charge dependent nuclear cross-sections. Both particle absorption and creation are forward-backward symmetric and so to first order affect $\langle Q_F \rangle$ and $\langle Q_B \rangle$ equally and therefore have no influence on $\langle Q_{FB} \rangle$, but result in $\langle Q \rangle$ being non-zero.

6.3 Experimental systematic errors

The experimental systematic errors on $\langle Q_{FB} \rangle$ are of two types. The most important effects are those that are both forward-backward and charge asymmetric since they can generate a false electroweak asymmetry. Other effects that are either forward-

backward or charge asymmetric result in a dilution of $\langle Q_{FB} \rangle$ and produce an uncertainty proportional to the asymmetry. The evaluation of the systematic errors is explained in detail in [31] and is briefly described below[2].

6.3.1 Forward-backward momentum imbalance

Non-uniformity in the ALEPH magnetic field could produce a significant charge asymmetry. Di-muon events in which the acollinearity of the muons is less than 0.3° are used to correct for any momentum imbalance. The average momentum of the muons in each of twelve $cos\theta$ bins is forced to match that expected for both signs. The correction is applied to the track sagitta and has a precision of $\sim 40\mu$m corresponding to a maximum momentum change of 1%. The systematic errors on each measured $\langle Q_{FB} \rangle$ value is taken as the larger of, half the shift in $\langle Q_{FB} \rangle$ with and without the track sagitta correction or the error on the correction, and are shown in the first row of table 6.4 for a range of κ.

Systematic	$\Delta(\langle Q_{FB} \rangle) \times 10^4$					
error source	$\kappa = 0.3$	$\kappa = 0.5$	$\kappa = 1.0$	$\kappa = 1.5$	$\kappa = 2.0$	$\kappa = \infty$
Momentum imbalance	0.1	0.3	0.6	0.9	1.0	1.4
Material asymmetry	0.8	0.6	0.3	0.1	0.1	0.0
Track losses	1.6	1.7	2.0	2.4	2.6	4.1
Unphysical tracks	0.1	0.2	0.2	0.3	0.4	0.5
Total systematic error	1.8	1.8	2.1	2.6	2.8	4.3

Table 6.4: $\langle Q_{FB} \rangle$ *experimental systematic errors.*

[2] The experimental systematic errors on $\langle Q_{FB} \rangle$ were evaluated for the hadronic charge asymmetry analysis [18] but can used as *conservative* estimates of those errors appropriate to this analysis

6.3.2 Material asymmetry

As mentioned above, the interaction of charged particles in the material between the primary vertex and the inner wall of the TPC is charge asymmetric. On its own, this effect changes the measured charge asymmetry, but if the effect is correctly modelled within the quark charge separations it cannot generate a false electroweak asymmetry. However, if combined with a possible asymmetry in the amount of detector material in the forward and backward hemispheres, it can generate a false electroweak asymmetry. The material asymmetry is measured by comparing the photon conversion rates in the forward and backward hemispheres as a function of $cos\theta$ and is found to be $A_{mat} = +1.8 \pm 1.6\%$. The systematic error on $\langle Q_{FB} \rangle$ can then be estimated using the product $A_{mat} \cdot \langle Q \rangle$, where $\langle Q \rangle$ is the mean total event charge measured in data. The resulting errors are shown in table 6.4.

6.3.3 Track losses

The stability of $\langle Q_{FB} \rangle$ with respect to each of the arbitrarily chosen track cuts is examined by measuring $\langle Q_{FB} \rangle$ using those tracks that pass all selection criteria but are near the cut for one of the criteria. Four track cuts are varied as explained in the following list (the standard cuts are listed first) :

- $|D_0| \leq 2.0\text{cm}$; $|D_0| \leq 1.6\text{cm}$,
- $|Z_0| \leq 10.0\text{cm}$; $|Z_0| \leq 8.0\text{cm}$,
- $N_{TPC\ hits} < 4$; $N_{TPC\ hits} < 5$,
- $cos\theta \leq 0.95$; $cos\theta \leq 0.94$.

D_0 (Z_0) is the distance of closest approach of a charged track to the ALEPH origin along (transverse to) the beam direction, $N_{TPC\ hits}$ is the number of reconstructed coordinates in the TPC and $cos\theta$ is the cosine of the polar angle of the track. The total systematic error due to track losses is obtained by adding in quadrature each of the variations, and are shown in table 6.4.

6.3.4 Charged tracks with unphysically high momentum

Approximately 0.3% of hadronic events contain at least 1 unphysically high momentum ($p > 50\text{GeV}/c$) charge track, as a result of reconstruction ambiguities such as overlapping tracks. These tracks are produced with equal rates in the forward and backward hemispheres and for positive and negative tracks and therefore should not influence the charge asymmetry measurement. But they can introduce an uncertainty in the interpretation of $\langle Q_{FB} \rangle$ if the effects are not accurately reproduced in the Monte Carlo simulation of the background charge separations. The b charge separation is evaluated in data and so includes these effects correctly.

$\langle Q_{FB} \rangle$ is evaluated with and without those events containing unphysically high momentum tracks and its systematic error is taken as the product $\mathcal{P}^{udsc} \cdot \Delta(\langle Q_{FB} \rangle)$, where P^{udsc} is the measured background fraction and $\Delta(\langle Q_{FB} \rangle)$ is the change in $\langle Q_{FB} \rangle$ when those events with high momentum tracks are removed. These errors are shown in table 6.4.

6.4 Summary

The forward-backward hemisphere charge asymmetry, $\langle Q_{FB} \rangle$, has been measured in hadronic data samples of varying b purity and with different values for the momentum weighting parameter, κ. The results are presented in table 6.2. The evaluation of the experimental systematic errors on $\langle Q_{FB} \rangle$ has been described. The errors obtained are

shown in table 6.4 for a range of κ values. In chapter 7 the $\langle Q_{FB} \rangle$ values are used, in conjuction with the quark purities and acceptance factors presented in chapter 4 and the quark charge separations presented in chapter 5, to determine a value for the underlying $b\bar{b}$ forward-backward asymmetry $\mathcal{A}_{FB}^{b\bar{b}}$.

Chapter 7

Electroweak interpretation of the charge asymmetry

This chapter concerns itself with the electroweak interpretation of the measured forward-backward hemisphere charge asymmetry, $\langle Q_{FB} \rangle$, presented in chapter 6. In section 7.1 an outline of the calculation of the quark asymmetries and Z^0 branching fractions in the framework of the Standard Model is given and the effective weak mixing angle, $sin^2\theta_W^{eff}$, is defined. Section 7.2 describes a correction applied to $\mathcal{A}_{FB}^{b\bar{b}}$ to account for QCD effects. Section 7.3 summarises the procedure used to fit the data and extract the underlying $b\bar{b}$ asymmetry and weak mixing angle and in section 7.4 the systematic errors on both quantities are determined.

7.1 A Standard Model analysis of the data

The Minimal Standard Model of Glashow, Weinberg and Salam is used to analyse the measured forward-backward charge asymmetry $\langle Q_{FB} \rangle$. To this end, the ZFITTER package [32] is used. ZFITTER is a program based on a semi-analytical approach to

fermion pair production in e^+e^- annihilation:

$$e^+e^- \rightarrow f\bar{f}(n\gamma) \tag{7.1}$$

and is optimised for energies near the Z^0 pole. The program directly calculates predictions for cross-sections and forward-backward asymmetries. The calculational scheme involves the convolution of effective Born cross-sections which describe the underlying hard scattering process with QED radiator functions which depend on the treatment of initial and final state radiation.

The quark asymmetries and branching fractions are predicted by the minimal Standard Model once α, G_μ, M_Z, M_H and the fermion masses, m_f, are all known. The Thompson limit QED coupling constant, α, the Fermi coupling constant, G_μ, and M_Z have been determined experimentally to a high precision, compared to the other parameters, and can be considered as fundamental parameters of the Standard Model. Neither the precise values of the light quark masses nor their physical meaning are unambiguously known, but they enter the radiative corrections only through the vector boson self-energies where their contribution can be replaced by the experimentally known cross-sections for $e^+e^- \rightarrow hadrons$. A similar ambiguity exists for the b quark mass, m_b. In this analysis m_b is fixed at 4.5 GeV/c^2. This increases $\mathcal{A}_{FB}^{b\bar{b}}$ by approximately 0.5% compared to the $m_b = 0$ approximation. This is an order of magnitude smaller than the precision presently available, so the uncertainty on m_b can safely be ignored. This leaves m_t and M_H as the only unknown parameters upon which the quark asymmetries depend.

The light quark cross-sections depend on m_t purely via corrections to the Z^0 propagator (figure 7.1.a). However for b quarks, owing to the large mass splitting between b and t quarks, there are two vertex diagrams for $Z^0 \rightarrow b\bar{b}$ (figure 7.1.b) which contribute additional m_t dependent corrections to $\mathcal{A}_{FB}^{b\bar{b}}$ and $\Gamma^{b\bar{b}}$ which are absent for light quarks. The effect of the vertex corrections is evident in the top mass dependence

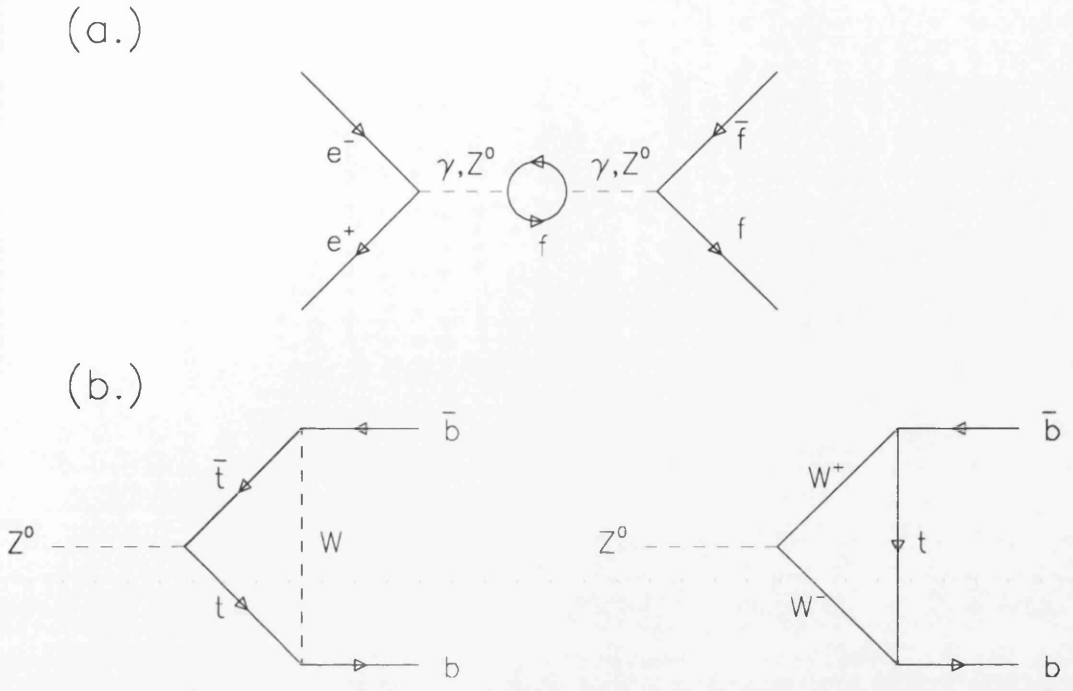

Figure 7.1: *(a.) Corrections to the Z^0 propagator, including self-energy insertions, γ exchange and $\gamma - Z^0$ interference. (b.) The vertex diagrams for $Z^0 \rightarrow b\bar{b}$ which contribute additional m_t dependent corrections to $\mathcal{A}_{FB}^{b\bar{b}}$ and $\Gamma^{b\bar{b}}$.*

of the b and d branching fractions, as shown in figure 7.2, but effectively cancels in the asymmetry, producing only a shift in its normalisation.

In the on-shell renormalisation scheme used in ZFITTER, the weak mixing angle is defined uniquely through the gauge-boson masses :

$$sin^2\theta_W = 1 - \frac{M_W^2}{M_Z^2} \, . \tag{7.2}$$

Electroweak radiative corrections to the bare cross-sections can be parameterised in such a way that they are absorbed into a redefinition of $sin^2\theta_W$. The resulting 'effective' weak mixing angle $sin^2\theta_W^{eff}$ is often defined as

$$sin^2\theta_W^{eff} = \kappa_e^Z sin^2\theta_W \, , \tag{7.3}$$

where κ_e^Z is the electron weak form factor which contains the corrections to the bare

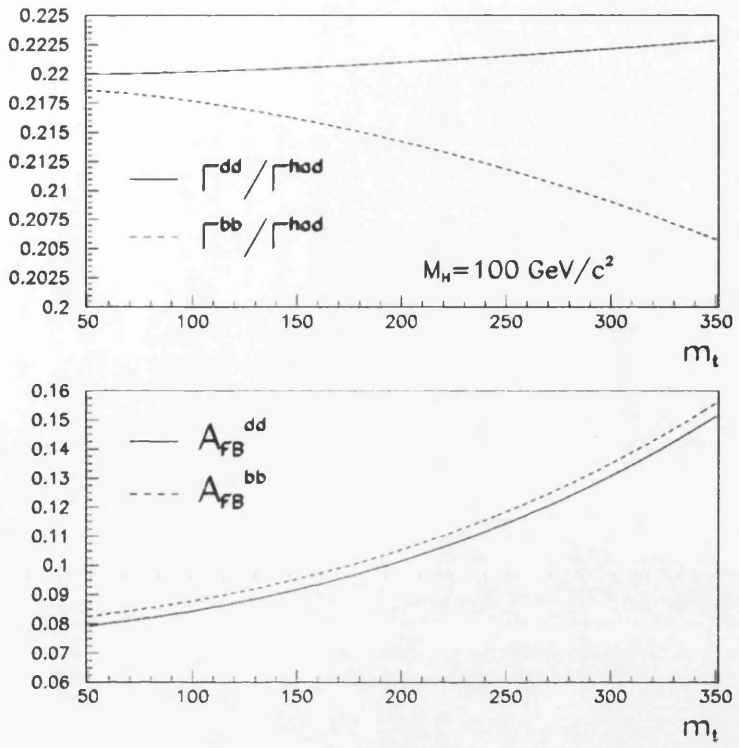

Figure 7.2: *The top mass dependence of the b and d branching fractions and asymmetries.*

cross-sections including the dependence on m_t and M_H.

Figure 7.3 shows the m_t dependence of $sin^2\theta_W^{eff}$ for three different Higgs masses as calculated using ZFITTER. Varying the top mass from 200 GeV/c^2 to 250 GeV/c^2 changes $sin^2\theta_W^{eff}$ by only 1%, so a precision measurement is required to be sensitive to the top mass dependent radiative corrections. The sensitivity to M_H is much weaker ; the ambiguity in $sin^2\theta_W^{eff}$ due to varying M_H in the range 60 GeV $< M_H <$ 1 TeV is below the present experimental error, so that for practical purposes, at the present stage of accuracy, the predictions can be plotted as functions of m_t.

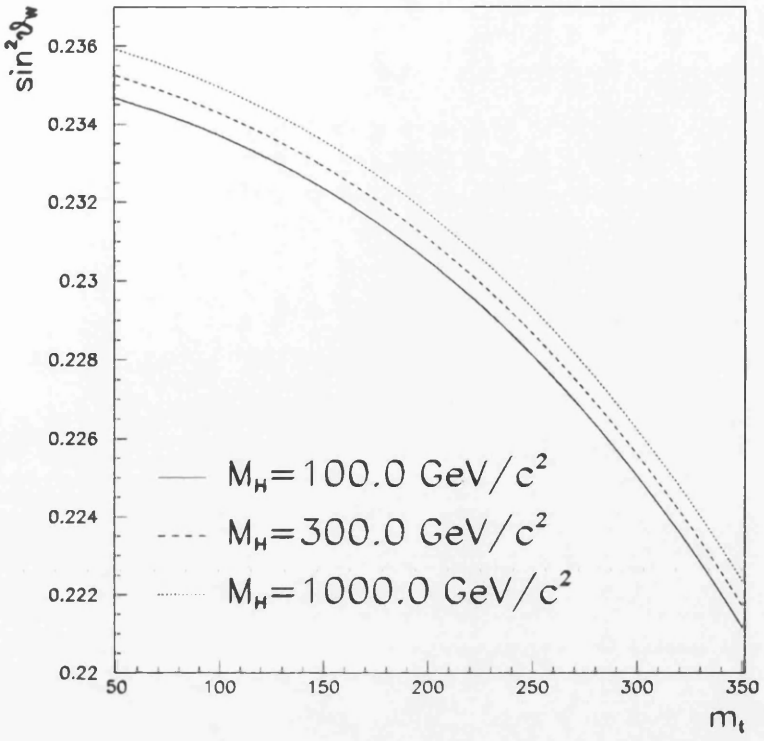

Figure 7.3: *The m_t and M_H dependence of the weak mixing angle $sin^2\theta_W^{eff}$ as calculated using ZFITTER.*

7.2 QCD corrections to $\mathcal{A}_{FB}^{b\bar{b}}$

A precision measurement of $\mathcal{A}_{FB}^{b\bar{b}}$ requires a good understanding of higher order corrections to the Born level cross-sections. As described in the preceding section, ZFITTER incorporates initial and final state photon radiation and weak loop and vertex corrections to a sufficiently high precision. QCD effects including gluon radiation from the final state b and $\bar{b}$ quarks must also be corrected for. Figure 7.4 shows those diagrams which contribute to $\sigma(e^+e^- \rightarrow q\bar{q})$ to first order in α_s. The correction to $\mathcal{A}_{FB}^{b\bar{b}}$ takes the form [33] [34]

$$\mathcal{R}_{QCD} = 1 + c_1(m_b)\frac{\alpha_s}{\pi} + c_2(m_b, m_t)(\frac{\alpha_s}{\pi})^2 + ... \tag{7.4}$$

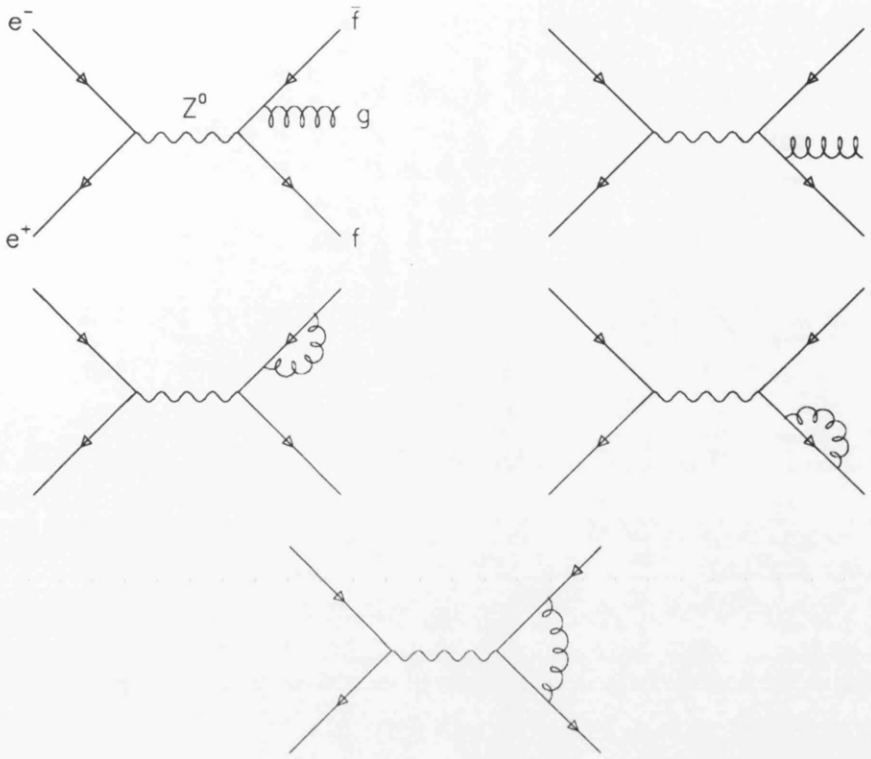

Figure 7.4: *Diagrams contributing to* $\sigma(e^+e^- \to q\bar{q})$ *to first order in* α_s.

At parton level, using a b quark mass of 4.5 GeV/c^2, c_1 is found to be approximately 0.8. The corresponding change in $\mathcal{A}_{FB}^{b\bar{b}}$ is a reduction of 3% relative to its Born level value.

In this analysis, however, the b quark direction is estimated using that of the thrust vector, $\vec{t}$, reconstructed using all charged and neutral final state particles. The hadronisation and decay processes dilute the ambiguity in the b quark direction introduced by the radiation of a hard gluon. Consequently the angular resolution between the thrust vector and the initial b quark direction is better than that between the b quark direction before radiating a gluon and its direction after radiating a gluon. The Monte Carlo program JETSET 7.3 simulates gluon radiation correctly to first order [35] and so can be used to estimate its effect on $\mathcal{A}_{FB}^{b\bar{b}}$.

Figure 7.5 shows the angular resolution between the thrust vector and the b quark

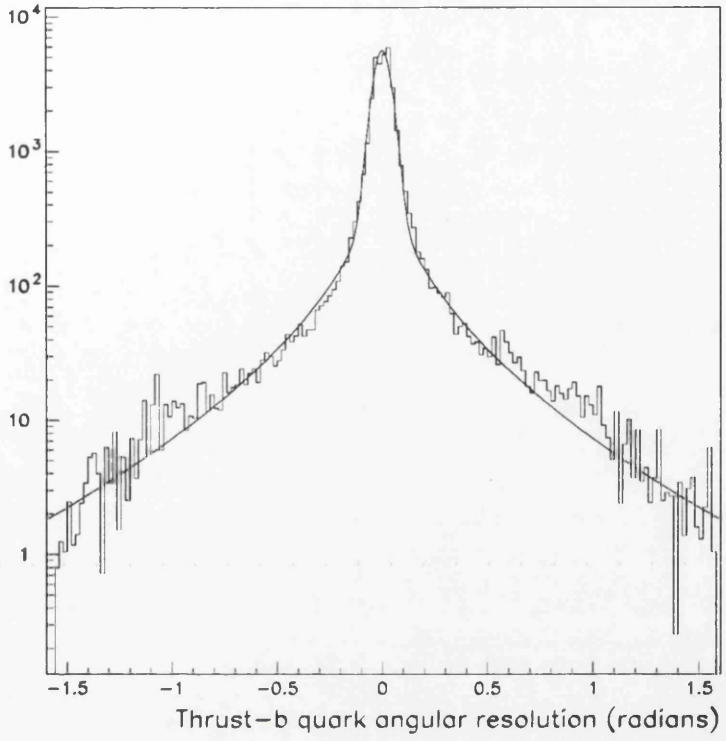

Figure 7.5: *The angular resolution between the thrust vector and the b quark direction before any gluon radiation obtained using Monte Carlo simulated data.*

direction before gluon radiation obtained using Monte Carlo simulated data (note the log scale). Using a fit to this distribution (superimposed) the b quark direction is smeared and the forward-backward asymmetry is re-evaluated. The asymmetry decreases by 0.6% (with a Monte Carlo statistical error of 0.1%), so rather than apply a correction, a conservative systematic error of 1% is included.

7.3 The fitting procedure

The measured charge asymmetry $\langle Q_{FB} \rangle$ can be expressed in terms of the underlying quark asymmetries $\mathcal{A}_{FB}^{f\bar{f}}$ and Z^0 branching fractions $\Gamma^{f\bar{f}}/\Gamma^{had}$ as follows :

$$\langle Q_{FB} \rangle = \frac{\sum_f \delta^f \, C^f \, \mathcal{A}_{FB}^{f\bar{f}} \, \varepsilon^f \, (\Gamma^{f\bar{f}}/\Gamma^{had})}{\sum_f \varepsilon^f \, (\Gamma^{f\bar{f}}/\Gamma^{had})} \quad , \tag{7.5}$$

where δ^f are the quark charge separations (chapter 5), ε^f are the event tagging efficiencies (chapter 4) and C^f are the flavour dependent acceptance factors (chapter 4).

	$sin^2\theta_W^{eff} \pm (stat)$				
κ	$P_h < 0.01$	$P_h < 0.005$	$P_h < 0.001$	$P_h < 0.0005$	$P_h < 0.0001$
0.3	0.2311 ± 0.0027	0.2294 ± 0.0026	0.2278 ± 0.0026	0.2282 ± 0.0026	0.2269 ± 0.0029
0.4	0.2314 ± 0.0025	0.2298 ± 0.0025	0.2280 ± 0.0025	0.2285 ± 0.0025	0.2269 ± 0.0028
0.5	0.2317 ± 0.0024	0.2302 ± 0.0024	0.2281 ± 0.0024	0.2287 ± 0.0025	0.2269 ± 0.0028
0.7	0.2321 ± 0.0023	0.2307 ± 0.0023	0.2285 ± 0.0024	0.2291 ± 0.0025	0.2272 ± 0.0028
0.9	0.2324 ± 0.0024	0.2310 ± 0.0024	0.2288 ± 0.0025	0.2296 ± 0.0026	0.2276 ± 0.0029
1.0	0.2325 ± 0.0024	0.2311 ± 0.0024	0.2289 ± 0.0025	0.2298 ± 0.0026	0.2278 ± 0.0030
1.2	0.2326 ± 0.0024	0.2312 ± 0.0025	0.2290 ± 0.0026	0.2301 ± 0.0027	0.2281 ± 0.0031
1.5	0.2326 ± 0.0025	0.2313 ± 0.0025	0.2292 ± 0.0028	0.2304 ± 0.0029	0.2285 ± 0.0033
2.0	0.2327 ± 0.0027	0.2314 ± 0.0027	0.2293 ± 0.0030	0.2308 ± 0.0031	0.2290 ± 0.0036
∞	0.2341 ± 0.0041	0.2311 ± 0.0043	0.2286 ± 0.0049	0.2311 ± 0.0051	0.2285 ± 0.0060

Table 7.1: *The fitted $sin^2\theta_W^{eff}$ values. The errors are due to the statistical error on the measured $\langle Q_{FB} \rangle$.*

The measured charge asymmetry $\langle Q_{FB} \rangle$ and its relation to the quark asymmetries expressed through equation 7.5 are used to determine the effective weak mixing angle $sin^2\theta_W^{eff}$. $\langle Q_{FB} \rangle$ is reconstructed using the measured δ^f, C^f, ε^f and $\Gamma^{b\bar{b}}/\Gamma^{had}$, and $\mathcal{A}_{FB}^{f\bar{f}}$ and $\Gamma^{f\bar{f}}/\Gamma^{had}$ ($f \neq b$) calculated using ZFITTER. M_H is set at 300 GeV/C^2 and m_t is varied between 50 and 350 GeV/c^2. The 'best' m_t is chosen as that which minimises the difference between the reconstructed $\langle Q_{FB} \rangle$ and its measured value. Corresponding to this top mass, the effective weak mixing angle and $b\bar{b}$ asymmetry are determined. The resulting values are shown in tables 7.1 and 7.2 respectively. The errors are statistical only, corresponding to the 1 sigma statistical error on $\langle Q_{FB} \rangle$.

	$A_{FB}^{b\bar{b}} \pm (stat)$				
κ	$P_h < 0.01$	$P_h < 0.005$	$P_h < 0.001$	$P_h < 0.0005$	$P_h < 0.0001$
0.3	0.1022 ± 0.0149	0.1115 ± 0.0143	0.1200 ± 0.0140	0.1176 ± 0.0143	0.1251 ± 0.0156
0.4	0.1002 ± 0.0137	0.1090 ± 0.0133	0.1190 ± 0.0133	0.1164 ± 0.0136	0.1250 ± 0.0150
0.5	0.0988 ± 0.0132	0.1072 ± 0.0129	0.1183 ± 0.0131	0.1153 ± 0.0134	0.1248 ± 0.0149
0.7	0.0965 ± 0.0128	0.1044 ± 0.0127	0.1164 ± 0.0131	0.1127 ± 0.0136	0.1232 ± 0.0152
0.9	0.0949 ± 0.0129	0.1025 ± 0.0128	0.1147 ± 0.0135	0.1102 ± 0.0140	0.1210 ± 0.0159
1.0	0.0946 ± 0.0130	0.1020 ± 0.0130	0.1142 ± 0.0137	0.1093 ± 0.0143	0.1201 ± 0.0162
1.2	0.0941 ± 0.0133	0.1014 ± 0.0134	0.1134 ± 0.0142	0.1077 ± 0.0149	0.1184 ± 0.0169
1.5	0.0937 ± 0.0137	0.1009 ± 0.0139	0.1126 ± 0.0150	0.1057 ± 0.0157	0.1161 ± 0.0179
2.0	0.0935 ± 0.0145	0.1007 ± 0.0148	0.1120 ± 0.0161	0.1035 ± 0.0169	0.1135 ± 0.0194
∞	0.0856 ± 0.0227	0.1019 ± 0.0235	0.1160 ± 0.0262	0.1021 ± 0.0275	0.1162 ± 0.0323

Table 7.2: *The fitted $A_{FB}^{b\bar{b}}$ values. The errors are due to the statistical error on the measured $\langle Q_{FB} \rangle$.*

As expected the statistical error on $sin^2\theta_W^{eff}$ reaches a minimum for $\kappa = 0.5$ and $P_h < 0.001$, since it is for this combination that the measured $\langle Q_{FB} \rangle$ is most significant :[1]

$$sin^2\theta_W^{eff} = 0.2281 \pm 0.0024(stat)\,,$$
$$A_{FB}^{b\bar{b}} = 0.1183 \pm 0.0131(stat)\,.$$

The corresponding Standard Model top mass limits are

$$m_t = 260^{+39}_{-47}\,. \tag{7.6}$$

[1] The statistical error is smaller for a κ of 0.7 and a looser tag cut of $P_h < 0.005$, but the b charge separation for this κ is estimated using Monte Carlo simulation. Consequently the systematic error due to fragmentation uncertatinies makes the total error larger.

The κ and P_h cut dependence of $sin^2\theta_W^{eff}$ and $\mathcal{A}_{FB}^{b\bar{b}}$ are shown in figures 7.6 and 7.7.

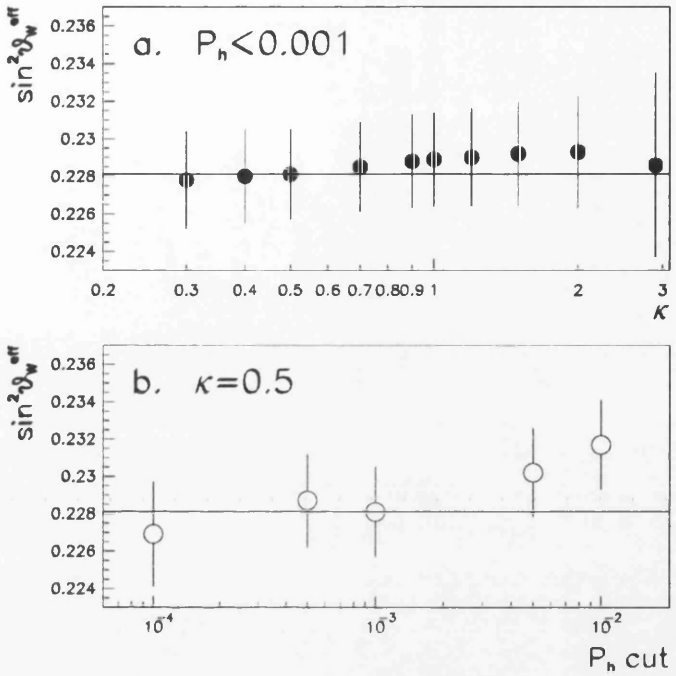

Figure 7.6: *The dependence of $sin^2\theta_W^{eff}$ on (a). κ and (b). the cut on the lifetime tag P_h. The errors shown are statistical only and are highly correlated as a function of both κ and tag cut. However, it is clear that each $sin^2\theta_W^{eff}$ value is consistent with the optimal value of 0.2281 at $\kappa = 0.5$ and $P_h < 0.001$.*

7.4 Systematic errors

In this section the systematic errors on $sin^2\theta_W^{eff}$ and $\mathcal{A}_{FB}^{b\bar{b}}$ are determined. The systematic errors enter via the now familiar relation

$$\langle Q_{FB} \rangle = \frac{\sum_f \delta^f \, C^f \, \mathcal{A}_{FB}^{f\bar{f}} \, \varepsilon^f \, (\Gamma^{f\bar{f}}/\Gamma^{had})}{\sum_f \varepsilon^f \, (\Gamma^{f\bar{f}}/\Gamma^{had})} \quad .$$

There are four main sources of systematic uncertainty :

- $\langle Q_{FB} \rangle$ experimental systematics (chapter 6),

error source	$sin^2\theta_W^{eff}$	$\mathcal{A}_{FB}^{b\bar{b}}$
$\langle Q_{FB} \rangle$ *syst*	0.00035	0.00192
δ^b *stat*	0.00050	0.00271
δ^b *syst*	0.00071	0.00383
$\delta^f (f \neq b)$ *stat*	0.00005	0.00024
$\delta^f (f \neq b)$ *syst*	0.00020	0.00107
ε_h^{uds}	0.00019	0.00106
ε_h^c	0.00031	0.00171
F_h, F_d	0.00002	0.00011
$\mathcal{P}^f$ *syst*	0.00028	0.00156
C^b *stat*	0.00002	0.00022
C^b *syst*	0.00009	0.00037
$C^f (f \neq b)$ *stat*	0.00001	0.00001
QCD correction	0.00022	0.00118
$\langle Q_{FB} \rangle$ *stat*	0.00240	0.01310
Total	0.00260	0.01420

Table 7.3: *The statistical and dominant systematic errors on* $sin^2\theta_W^{eff}$ *and* $\mathcal{A}_{FB}^{b\bar{b}}$ *at the nominal tag cut and* κ.

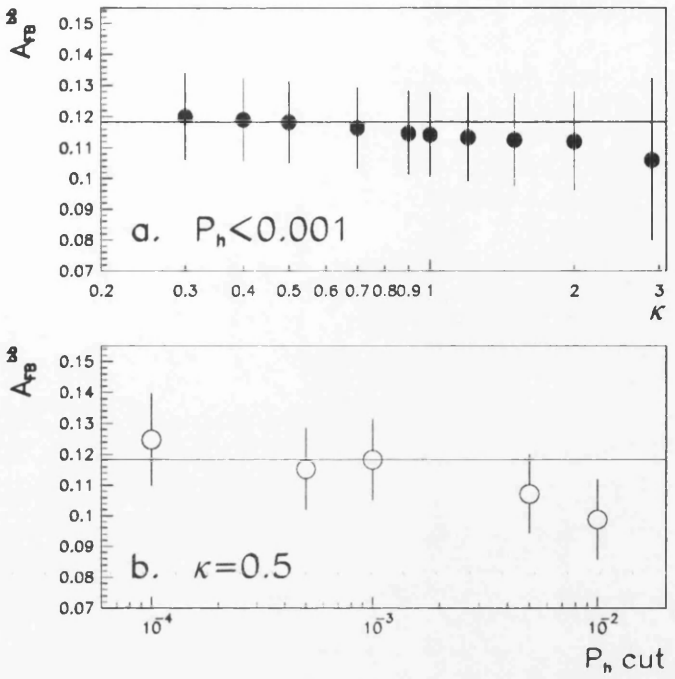

Figure 7.7: *The dependence of $\mathcal{A}_{FB}^{b\bar{b}}$ on (a). κ and (b). the cut on the lifetime tag P_h.*

- statistical and systematic errors on the quark charge separations δ^f (chapter 5)
- total errors on the quark tagging efficiencies ε^f and the $b\bar{b}$ branching fraction $\Gamma^{b\bar{b}}/\Gamma^{had}$ (chapter 4)
- statistical and sytematic errors on the flavour dependent acceptance factors C^f (chapter 4)

The systematic errors on $sin^2\theta_W^{eff}$ and $\mathcal{A}_{FB}^{b\bar{b}}$ correspond to the one sigma variation in each of the above quantities. For example to evaluate the error on $sin^2\theta_W^{eff}$ due to the statistical error on the b charge separation δ^b, δ^b is varied by $\pm$ its statistical error and the fit, described in the previous section, is repeated. The maximum resulting shift in $sin^2\theta_W^{eff}$ is taken as its systematic error.

The propagation of the errors on ε^b and $\Gamma^{b\bar{b}}/\Gamma^{had}$ requires more care. The measured values of ε^b and $\Gamma^{b\bar{b}}/\Gamma^{had}$, presented in section 4.2.2, depend entirely on the four

independent variables ε_h^{uds}, ε_h^c, F_h and F_d according to equations 4.9 and 4.10 (λ^b has a negligible effect on the $sin^2\theta_W^{eff}$ measurement) and so only the uncertainty on these quantities need be propagated to errors on $sin^2\theta_W^{eff}$ and $\mathcal{A}_{FB}^{b\bar{b}}$. In propagating the uncertainty on ε^{uds}, for example, to a systematic error on $sin^2\theta_W^{eff}$, ε^{uds} is changed by $\pm$ its total error and the corresponding ε^b and $\Gamma^{b\bar{b}}/\Gamma^{had}$ are re-evaluated before refitting. In this way the correlations betwen the measured ε^b and $\Gamma^{b\bar{b}}/\Gamma^{had}$ are correctly taken into account.

Due to the dominance of the statistical error the optimal κ and tag cut are just those of the previous section. Table 7.3 shows the breakdown of the total errors on $sin^2\theta_W^{eff}$ and $\mathcal{A}_{FB}^{b\bar{b}}$.

Chapter 8

Summary and conclusions

The forward-backward hemisphere charge asymmetry has been measured in a sample of 70,259 hadronic heavy flavour decays of the Z^0 boson collected with the ALEPH detector at LEP. The charge asymmetry, expressed as the difference in the momentum weighted charges of the forward and backward hemispheres, is measured to be :

$$\langle Q_{FB} \rangle \; = \; -0.0112 \pm 0.0012(stat.) \pm 0.00018(syst.) \; .$$

Heavy flavour Z^0 decays are tagged by identifying the decay products of beauty and charmed hadrons via their large track impact parameters. The *uds* and *c* event tagging efficiencies are estimated using Monte Carlo simulation. The *b* efficiency is measured by counting the relative number of single and double-tag events. This method is insensitive to Monte Carlo modelling of *b* quark production and hadronisation and of *b* hadron decay. The *b* purity of the data sample is measured to be $88.01 \pm 1.25\%$. The angular dependence of the event tagging efficiencies were modelled using Monte Carlo simulated data.

The extent to which *uds* and *c* event hemispheres retain the charge of their parent quarks was estimated using Monte Carlo simulation. For the *b*-quark this was determined by comparing the widths of the forward-backward hemisphere charge *difference* and *sum* distributions in data samples of increasing *b* purity. The method is

insensitive to the simulation of b-quark hadronisation and decay properties.

The measured charge asymmetry is used in conjunction with the measured event tagging efficiencies and quark charge separations to determine a value for the $b\bar{b}$ forward-backward asymmetry, $\mathcal{A}_{FB}^{b\bar{b}}$:

$$\mathcal{A}_{FB}^{b\bar{b}} = 0.1183 \pm 0.0131(stat) \pm 0.0057(syst) .$$

Interpreting $\mathcal{A}_{FB}^{b\bar{b}}$ in the framework of the minimal Standard Model of electroweak interactions the effective weak mixing angle, $sin^2\theta_W^{eff}$, is found to be :

$$sin^2\theta_W^{eff} = 0.2281 \pm 0.0024(stat) \pm 0.0011(syst) ,$$

and the corresponding top quark mass limits are

$$m_t = 260 \, ^{+43}_{-50} \, \mathrm{GeV}/c^2 .$$

or

$$m_t < 338 \, \mathrm{GeV}/c^2 \qquad (95\% \text{ confidence level}) .$$

References

[1] V.Barger and R. Phillips, *Collider Physics*, Frontiers in Physics Series, Addison-Wesley Publishing, ISBN 0-201-05876-6 (1987).

[2] S. L. Glashow, em Partial Symmetries of Weak Interactions, Nucl. Phys. 22 (1961) 579.

[3] S. Weinberg, *Elementary Particle Theory*, Proc. 8'th Nobel Symposium, ed. N. Svartholm, Almquist and Wiksell, Stockholm, (1968).

[4] A. Salam, *A Model of Leptons*, Phys. Rev. Lett. 19 (1967) 1264.

[5] F. Halzen and A. D. Martin, *Quarks and Leptons*, Wiley, ISBN 0-471-81187-4 (1984).

[6] J. D. Bjorken and S. D. Drell, *Relativistic Quantum Field Theory*, McGraw-Hill.

[7] J. D. Bjorken and S. D. Drell, *Relativistic Quantum Mechanics*, McGraw-Hill.

[8] T. Sjostrand, CERN-TH.6488/92.

[9] G. Marchesini *et al.*, Comp. Phys. Commun., 67 (1991) 465.

[10] The LEP collaborations, CERN-PPE/93-157.

[11] G. Altarelli *et al.*, CERN 89-08.

[12] D. Decamp *et al.*, ALEPH Collab., Nuclear Insruments and methods A294 (1990) 121.

[13] A. S. Schwarz., *Silicon Strip Vertex Detectors at Z^0 factories*, MPI-PhE/92-05 (1992).

[14] W. Atwood *et al.*, CERN-PPE/91-24 (1991).

[15] A. Falvard *et al.*, ALEPH 93-30, PHYSIC 93-21.

[16] J. E. Campagne and R. Zitoun, Z. Phys. C, 43 (1989) 469-475.

[17] R. Brun *et al*, CERN-DD/EE/84-1 (1987).

[18] D. Decamp *et al.*, ALEPH Collab., Phys. Lett. B259 (1991) 377.

[19] D. Decamp *et al.*, ALEPH Collab., Phys. Lett. B284 (1992) 177.

[20] R. Field and R. Feynman, Nucl. Phys. B136 (1978) 1.

[21] D. Decamp *et al.*, ALEPH Collab., Phys. Rep. V 216 (1992) 253.

[22] D. Brown, M. Frank, ALEPH 92-135, PHYSIC 92-124.

[23] D. Brown *et al.*, ALEPH Collab., Phys. Lett. B313 (1993) 535.

[24] W. Bartel *et al.*, JADE Collab., Z. Phys. C, 33 (1986) 23.

[25] S. Bethke *et al.*, JADE Collab., Phys Lett, B213 (1988) 235.

[26] D. Decamp *et al.*, ALEPH Collab., Phys. Lett. B 257 (1991) 492.

[27] D. Brown, ALEPH 92-47, PHYSIC 92-42.

[28] P. Colrain and A. Halley, ALEPH 93-161, PHYSIC 93-138.

[29] A. Halley, ALEPH 93-172, PHYSIC 93-147.

[30] D. Decamp *et al.*, ALEPH Collab., Z. Phys. C, 48 (1992) 365-392.

[31] A. Blondel *et al.*, ALEPH 93-42, PHYSIC 93-33.

[32] D. Bardin *et al.*, CERN-TH.6443/92.

[33] A. Djouadi *et al.*, Z. Phys. C, 46 (1990) 411-417.

[34] B. Lampe, MPI-Ph/93-74 (1993).

[35] D. Buskulic *et al.*, ALEPH Collab., Zeit. Phys. C55 (1992) 209.